UNIVERSITY OF CALIFORNIA, SAN DIEGO

Imaging Excitable Cell Activity in *C. elegans*

A dissertation submitted in partial satisfaction of the

requirements for the degree Doctor of Philosophy

in

Biology

by

Rex Alexander Kerr

Committee in charge:

William R. Schafer, Chair
Marla B. Feller
Lawrence S.B. Goldstein
William B. Kristan
Roger Y. Tsien

2002

The dissertation of Rex Kerr is approved, and it is acceptable in quality and form for publication on microfilm:

_____

_____

_____

_____

_____

Chair

University of California, San Diego

2002

Table of Contents

List of Figures

List of Tables

ACKNOWLEDGEMENTS

The text of Chapter 2, in part, is a reprint of the material as it appears in Neuron in the article " Optical imaging of calcium transients in neurons and pharyngeal muscle of C. elegans." Neuron *26*, 583-594 by Kerr, R., Lev-Ram, V., Baird, G., Vincent, P., Tsien, R.Y., Schafer, W.R. (2000). The material contains three minor alterations from the published form. First, the work has been reformatted to fix references and to fit the format of this dissertation. Second, the original Figure 3 and the text describing electrical stimulation of neurons in [Kerr et al. 2000] has been moved to Chapter 3 where it fits more naturally with subsequent work. Finally, some results of work on vulval muscles started after the publication of the original paper are described in section 2.7. The dissertation author was the primary researcher and author and the co-authors listed above contributed advice and technical expertise and in part directed and supervised the research which forms the basis for Chapter 2.

VITA

1996 B.Sc. in Mathematics (with highest honors), Physics (with highest honors), and Molecular and Cell Biology (emphasis genetics), University of California, Berkeley

2002 Ph.D. in Biology, University of California, San Diego

PUBLICATIONS

Kerr, R., Lev-Ram, V., Baird, G., Vincent, P., Tsien, R.Y., Schafer, W.R. (2000). " Optical imaging of calcium transients in neurons and pharyngeal muscle of C. elegans." Neuron *26*, 583-594

Sagi, B., Nemat-Nasser, S., Kerr, R., Hayek, R., Downing, C., Hecht-Nielsen, R. (2001). "A biologically motivated solution to the cocktail party problem.". Neural Computation, *13*, 1575-1602.

Hardaker, L.A., Singer, E., Kerr, R., Zhou, G., Schafer, W.R. (2001). "Serotonin modulates locomotory behavior and coordinates egg-laying and movement in Caenorhabditis elegans." J. Neurosci. *49*, 303-313.

Mitchell, J.C., Kerr, R., Ten Eyck, L.F. (2001). "Rapid atomic density methods for molecular shape characterization." J. Molecular Graphics and Modelling *19*, 325-330.

ABSTRACT OF THE DISSERTATION

Imaging Excitable Cell Activity in *C. elegans*

by

Rex Alexander Kerr

Doctor of Philosophy in Biology

University of Californa, San Diego, 2002

Professor William R. Schafer, Chair

The nematode worm *Caenorhabditis elegans* has a relatively simple nervous system consisting of 302 neurons of known lineage and connectivity. Despite this simplicity, the worm exhibits relatively complex behaviors such as chemotaxis, avoidance of noxious stimuli, and associative and non-associative forms of learning. In addition, the well-developed techniques for genetic analysis of the worm facilitate the discovery and characterization of the molecules responsible for this behavior. However, electrophysiology is particularly problematic due to the worm's size and morphology. Techniques that enable the detection of neuronal activity are therefore of considerable interest. This manuscript presents the development of such a technique. We use the fluorescent calcium indicator protein cameleon to optically monitor the activity of excitable cells. Initially, we show that cameleon can be used to detect the activity of the pharyngeal muscle in *C. elegans*. These calcium transients are quantitatively compared between wild-type worms and those with mutations in calcium channel subunits. Mutations in the *egl-19* voltage-gated calcium channel, previously shown via electrical recording to

increase or decrease the duration of calcium transients, gave similar results with calcium imaging. We also show that mutations in the *unc-36* accessory subunit increase the rate of calcium entry without affecting transient duration. We then investigate the activity of the mechanosensory neurons of the worm, demonstrating that they function as motion sensors rather than pressure or displacement sensors, and that the response is not graded in intensity. The effect of disruption of the putative mechanoreceptor and habituating stimuli is also examined. Finally, we develop methods for the extraction of parameters describing calcium transient events from sequences of fluorescent images, a process that poses a number of technical challenges. Together, these results demonstrate for the first time a generic method for recording the activity of excitable cells in intact, behaving worms. Although this work is specifically focused on measuring the activity of *C. elegans* neurons, the experimental and mathematical techniques developed are of more general use in ratiometric imaging, and use of the technique in other organisms is promising given the success of the approach in *C. elegans.*

Chapter 1

Introduction

The nematode worm *Caenorhabditis* was selected as a model organism in 1963 by Sydney Brenner [Brenner 1988]. Brenner, a bacteriophage geneticist by training, hoped that with a small, easily cultivated organism with a short lifecycle, the powerful tools of molecular genetics could be used to investigate development and behavior. The choice was apparently a good one; in the years since then, *Caenorhabditis elegans* has provided important insights into development, behavior, the cell cycle, aging, and more. However, insight into the cellular and molecular basis of worm behavior proceeded perhaps more slowly than Sydney Brenner had hoped, due in part to the difficulty of using conventional electrophysiology to measure the activity of the worm's nervous system. Alternate approaches to determine activity took a number of years to develop.

Caenorhabditis elegans is a self-fertile soil-dwelling nematode. The adult hermaphrodite is approximately 1.5mm long, has a generation time of 3 days, and has 959 somatic cells of invariant lineage [Wood 1988, Riddle et al. 1997]. Of those, 302 are neurons, whose precise connectivity has been determined through reconstruction using serial electron micrographs. Despite this simple nervous system, the worm displays a variety of behaviors, including chemotaxis to food and certain chemicals and, in males to mates; deposition of eggs regulated by environmental cues; thermotaxis to cultivation temperatures; avoidance of noxious mechanical, chemical, and thermal stimuli, and habituation to repeated application of these stimuli; and associa-

tive learning of pairing of ions with either food or starvation [Chalfie and White 1988, Driscoll and Kaplan 1997, Jorgensen and Rankin 1997].

The primary tool to study the role of individual neurons in these behaviors has traditionally been single-cell laser ablation [Bargmann and Avery 1995]. Typically, animals in the larval L1 stage are viewed under DIC optics with high magnification where the cell bodies of the neurons of interest can be identified by their characteristic positions. A laser is then used to selectively damage that cell; it is particularly convenient if the ablation is performed in transgenic worms expressing GFP in that cell, as a loss of fluorescence will indicate a successful ablation. The function of the cell can then be inferred from behavioral defects exhibited by the ablated worm as compared to unablated controls. Systematic laser ablation has been used in conjunction with the known neuroanatomy of the worm to produce diagrams of functional circuits that are responsible for many of the behaviors mentioned above. Although single-cell ablation is a powerful technique, it has three main drawbacks for studying cellular activity. First, the process is time-consuming; behavioral tests typically must be performed on at least tens of worms, and each of those worms has to individually be mounted, ablated, recovered, checked, and so on, all before testing can even begin. Second, neurons with redundant function or subtle effects on behavior are difficult to detect via ablation. Third, ablation usually provides few insights into the response properties of a neuron and the molecular mechanisms underlying the neuron's activity.

Genetic analysis provides powerful tools for understanding the molecular mechanisms behind behavior. For example, a putative mechanotransduction complex has been defined through the isolation of mutants that are insensitive to low-intensity mechanical stimulation and a subsequent characterization of those genes and the genetic interactions between them. Promoter fusions, immunostaining, and mosaic analysis can be used to determine the site of action of a particular gene product. Neurons can also be genetically ablated by using cell-specific promoters to drive constitutively active potassium channels or cell-death proteins in cases where an appropriate promoter can be found and too many animals are required for laser ablation to be practical.

Unfortunately, despite the great utility of these techniques, they do not overcome the limitations of using behavior as a readout of the activity of individual cells; detailed response properties are still difficult to acquire, and subtle effects on behavior are still liable to be missed.

Recently, methods have been developed which allow electrical recording from neurons in semi-intact animals [Goodman et al. 1998] and in primary cell culture [Christensen et al 2002]. The process of making recordings from semi-intact animals is technically demanding, however, and currently recordings are quite limited in their duration. And while cell culture can be used to investigate the biophysical properties of channels, it is rather difficult to recreate a behavioral response in cell culture. Further development of both techniques, in conjunction with existing methods, promises to overcome most of the deficiencies of cell ablation, albeit with difficulty. Problems which are difficult to address with electrophysiology in other systems, such as simultaneous recording from multiple neurons, are likely to remain difficult in *C. elegans*, however.

Small-molecule indicators such as voltage sensitive dyes and calcium indicators provide another way to measure neuronal activity. Unfortunately, the impermeant cuticle of *C. elegans* prevents easy application of these compounds. Although they could be injected (and, in fact, calcium indicators have been injected into single *C. elegans* intestinal cells [Dal Santo et al. 1999]), accurate injection is difficult for the same reasons that electrophysiology is difficult. Recently, however, a variety of genetically encoded indicators have become available. In contrast to the difficulty of using small molecule indicators in *C. elegans*, protein-based indicators are particularly suited for use in the worm due to the wide variety of tissue-specific promoters available and the relative ease with which transgenic lines can be constructed. Protein-based indicators of neuronal activity therefore provide an exciting opportunity to bridge the gap between the circuit-level analysis of laser ablation and the detailed electrophysiological characterization of single neurons that should soon be possible in cell culture and semi-intact animals. Furthermore, since *C. elegans* is largely transparent, these optical indicators

can be used on intact, behaving worms with a minimum of sample preparation.

The genetically encoded indicators of particular use to us sense either calcium or voltage. Published reports of voltage sensors based on potassium channels show fluorescence intensity changes [Siegel and Isacoff 1997] or ratio changes [Sakai et al. 2001] of at best a few percent. Given the small size of *C. elegans* neurons, signals of this size are unlikely to be visible above the noise. Fortunately, the calcium indicators give larger responses. All of the indicators are currently based on calmodulin and fluorescent proteins. Ratiometric indicators include cameleon [Miyawaki et al. 1997, Miyawaki et al. 1999], the yellow variant of which consists of a CFP-CaM-M13-YFP fusion; M13 is a calmodulin binding peptide; and Persechini-type constructs [Romoser et al. 1997, Persechini et al. 1997] that consist of GFP-CB_{SM}-BFP-CaMCN, where CB_{SM} is a binding peptide and CaMCN is a circularly permuted version of calmodulin. Both constructs give ratio changes of 60-100% from zero to saturating (~1mM) calcium. Constructs that show intensity changes include camgaroo [Baird et al. 1999] and the pericams [Nagai et al. 2001], both of which give intensity changes of an order of magnitude. Of these, we selected cameleons, for several reasons. The kinetics and calcium affinity of cameleon were known to be suitable for reporting calcium transients of the duration we expected. A ratiometric indicator was desired given that small, moving samples can cause substantial intensity artifacts. And, importantly, cameleon was available when this study was begun.

Therefore, the goal is to develop a method for using cameleon to measure the activity of excitable cells in *C. elegans*, and to use this method to begin to characterize the activity patterns and response properties of a subset of these cells.

Chapter 2

Calcium Imaging in the *C. elegans* Pharyngeal Muscle

The manuscript "Optical Imaging of Calcium Transients in Neurons and Pharyngeal Muscle of *C. elegans*" by Rex Kerr, Varda Lev-Ram, Geoff Baird, Pierre Vincent, Roger Y. Tsien, and William R. Schafer follows. This material was originally published in Neuron vol. 26, pp. 583-594 (June 2000).

2.1 Summary

Electrophysiology and optical indicators have been used in vertebrate systems to investigate excitable cell firing and Ca^{2+} transients, but both techniques have been difficult to apply in organisms with powerful reverse genetics. To overcome this limitation, we expressed cameleon proteins, genetically encoded calcium indicators, in the pharyngeal muscle of the nematode worm *Caenorhabditis elegans*. In intact transgenic animals expressing cameleons, fluorescence ratio changes accompanied muscular contraction, verifying detection of calcium transients. By comparing the magnitude and duration of calcium influx in wild-type and mutant animals, we were able to determine the effects of calcium channel proteins on pharyngeal calcium transients. We also successfully used cameleons to detect electrically evoked calcium transients in in-

dividual *C. elegans* neurons. This technique therefore should have broad applications in analyzing the regulation of excitable cell activity in genetically tractable organisms.

2.2 Introduction

Genetically tractable model organisms have many advantages for investigating nervous system function at the molecular and cellular level. For example, the nematode *Caenorhabditis elegans* has a simple and well characterized nervous system, consisting of only 302 neurons of defined position, connectivity, and cell lineage. Since each neuron can be positively identified based on its position, it is possible to evaluate the function of an individual neuron or group of neurons through single cell laser ablation. Moreover, because of their short generation time, small genome size, and accessibility to germline transformation, *C. elegans* is highly amenable to molecular and classical genetics. Thus, in *C. elegans* it is relatively easy to identify genes involved in specific behaviors, and to infer the functions of their products in the neurons and muscle cells controlling those behaviors using genetics and molecular cloning.

To rigorously determine how a particular gene product affects the activity of an excitable cell, it is often important to directly measure its effect on cellular physiology. Unfortunately, the small neurons and hydrostatic skeleton of *C. elegans* have made physiological studies difficult, especially in live animals. Existing protocols for recording electrically from *C. elegans* neurons or muscle cells all involve slicing open or rupturing the cuticle to expose the cell of interest, and recordings from intact behaving animals have not been reported. In principle, calcium imaging offers an alternative approach for monitoring excitable cell activity in vivo. However, the anatomy of *C. elegans* presents a number of difficulties for using traditional dyes for calcium imaging. The relatively impermeant cuticle prevents uptake of bath-applied dye, and the hydrostatic skeleton makes dissection and microinjection difficult. Although large cells such as oocytes and intestinal cells have been successfully loaded with calcium-sensitive dye through microinjection, neurons and even many muscle cells are too small to reli-

ably load in this way. Moreover, even when successful, microinjection has been limited to single cells [Dal Santo et al. 1999].

To circumvent these problems, we are using the calcium indicator protein cameleon [Miyawaki et al. 1997] to image calcium transients in intact *C. elegans*. Cameleons are composed of four domains: cyan fluorescent protein (CFP), calmodulin, M13 (a calmodulin binding domain), and yellow fluorescent protein (YFP). In low calcium concentrations, calmodulin is not bound to M13 and the protein is in a poor configuration for fluorescence resonance energy transfer (FRET) between CFP and YFP. Excitation of CFP leads primarily to CFP emission with lesser energy transfer to YFP and YFP emission. Upon an increase in calcium concentration, calmodulin binds calcium and attracts M13. This brings CFP and YFP into a more favorable location or orientation for FRET; excitation of CFP will then lead to increased energy transfer and an increase in YFP emission at the expense of CFP emission. Hence, an increase in calcium causes an increase in the YFP/CFP fluorescence intensity ratio. The ratiometric nature of the indicator is ideal for in vivo application to moving cells, as motion artifacts that affect total intensity are canceled out in the ratio. Genetically encoded sensors such as cameleon are especially attractive for organisms such as *C. elegans* where a large number of tissue-specific promoters are known. In addition to allowing precise tissue targeting and reducing the effort required to prepare each animal, subcellular localization can be achieved by using appropriate signal sequences attached to the sensor.

Cameleons were previously shown to function as a fluorescent calcium sensor in cultured cells. To develop methods for using cameleon in an intact animal, we chose to concentrate primarily on the pharyngeal muscle of *C. elegans*. The pharynx is a relatively large (around 20 microns in diameter at the terminal bulb) muscular organ that pumps bacteria into the worm's intestine for consumption. The pharynx pumps rapidly in the presence of serotonin, and calcium transients can be independently detected through the visible contraction of the muscle cells. Electrical recordings have been made from the dissected pharyngeal muscles of wild-type and mutant worms, making the pharynx perhaps the physiologically best-characterized excitable tissue in

C. elegans [Avery and Thomas 1997]. Since many of the components involved in production and regulation of calcium transients are common to both muscles and neurons, an investigation of molecular function in muscles may aid in understanding neuronal calcium dynamics. However, the calcium dynamics of the pharynx have not been explicitly studied, due largely to a lack of appropriate calcium sensors.

Here we describe the use of cameleon to image calcium transients in excitable cells of *C. elegans*. We have detected calcium influx in the pharyngeal muscle of intact animals as part of normal feeding behavior, and in neurons in response to an extracellular electrical stimulation. Imaging studies of mutant animals provided insight into the effects of calcium channel proteins on the calcium dynamics of *C. elegans* muscle cells.

2.3 Results

2.3.1 Detection of pharyngeal calcium transients in *C. elegans*

To verify that cameleon could be used to detect calcium transients in the C. elegans pharynx, we created an expression vector driving the YC2.1 (yellow cameleon 2.1) variant of cameleon [Miyawaki et al. 1999] in the *C. elegans* pharynx under the control of the pharyngeal-specific *myo-2* promoter [Okkema et al. 1993]. We then created a line of worms containing an integrated array of this expression vector. The line, *ljIs1*, showed moderately variable expression levels of YC2.1 throughout the pharynx. Typically, the terminal bulb had the highest expression, while the corpus had lower expression levels. Fluorescence was frequently not visible in the isthmus. A typical example of expression in the pharynx is shown in Figure 2.1b.

We recorded from adult hermaphrodite worms from the line *ljIs1*. Feeding behavior was stimulated by exposure to serotonin (Avery and Horvitz, 1990). We used a MultiViewer (Princeton Instruments), a wide-field emission image splitter, to make simultaneous measurements of both the cyan and yellow emission intensities with a single CCD camera, as diagrammed in Figure 2.1a. The cyan-filtered image fell on the top half of the CCD array, while the yellow-filtered image fell on the bottom half, yielding

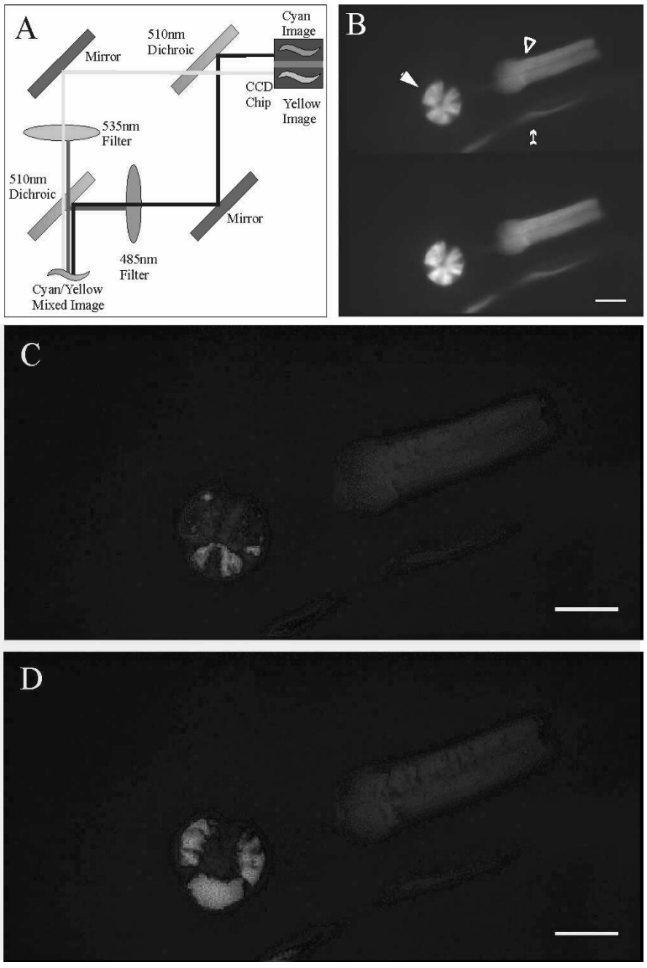

Figure 2.1: Imaging of Cameleon in the *C. elegans* Pharynx

(A) Simultaneous dual-emission recording with an emission image splitter. The emitted light is split with a dichroic mirror and cyan and yellow channels are isolated with filters, then recombined with a small offset and projected onto a single CCD chip.

(B) An unprocessed image of the pharynx under 405nm excitation. The top image is the cyan (485nm) channel; the bottom image is the yellow (535nm) channel. Scale bar is 20μm. The terminal bulb (solid triangle) was used for subsequent analysis. The corpus (open triangle) often also showed expression. Reflections off of bubbles (small arrow) were ignored. The worm's nose is to the upper right; the remainder of the body leaves the field of view to the lower left.

(C) A split and aligned image of the pharynx when the muscle is not contracted. Color indicates the intensity of yellow over the intensity of cyan for each pixel; bright shades indicate high ratios, or higher calcium while dark shades indicate lower ratios, or lower calcium. Brightness reflects mean intensity of the pixels in each channel. Scale bar is 20μm.

(D) Image of the same worm while the pharynx is contracted. There is a marked brightening in the shade-encoded image of the contracted image relative to the uncontracted one, as expected from an increase in calcium levels. Scale bar is 20μm.

raw images like the one shown in Figure 2.1b. The split images were superimposed, aligned, and displayed with the software package MetaFluor (Universal Imaging). A color scale was used to indicate the ratio at each pixel and assist in visual identification of fluorescence ratio changes. Frames showing visible opening of the terminal bulb (caused by muscular contraction) also showed elevated fluorescence emission ratios, consistent with elevated calcium during contraction (Figure 2.1c,d).

To follow calcium transients over time, we recorded streams of images at 20Hz and calculated the mean fluorescent intensity ratio over the terminal bulb of the pharynx. As shown in Figure 2.2a, traces of the mean ratio in terminal bulb showed distinct peaks during active pumping. Observation of contractile events showed that the onset of visible contraction occurred simultaneously with the increase in fluorescence ratio (Figure 2.2a). To verify that the ratio changes were a result of calcium influx and not motion artifacts, we artificially induced motion artifacts by changing the focal plane and moving the stage during recording. Ratio changes were minimal and differed in appearance from the sharp rises accompanying pharyngeal contraction. The slow return to baseline in the ratio signal was also inconsistent with any movement artifacts. Finally, we liberated the worms' heads from their bodies and applied digitonin, a membrane permeabilizing detergent, to gain access to the cytoplasm of the pharynx. External application of intracellular saline with either 0 Ca^{2+} + 4mM EGTA or 10mM Ca^{2+} gave a ratio change of $72 \pm 4\%$ (Figure 2.2c), reasonably consistent with the maximum ratio change of 90-100% in vitro [Miyawaki et al. 1999]. Thus, the cameleon protein expressed within the pharynx showed normal responses to calcium. Taken together, these results indicated that the observed increases in ratio were reliably indicating calcium transients within the muscle.

The ability to effectively image calcium transients in the pharynx was affected by a number of technical considerations. First, ratiometric imaging appeared to be critical for reliable detection of calcium changes. Although it was frequently possible to infer the location of the contractions from an individual wavelength trace, the ratioing process removed a great deal of the noise resulting from sample movement and pho-

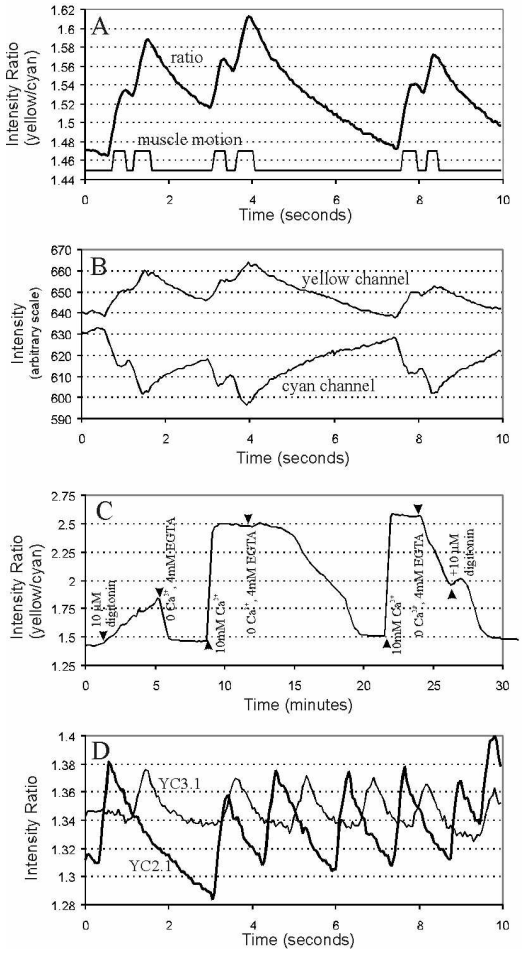

Figure 2.2: Visualization of Calcium Transients

(A) The yellow/cyan intensity ratio (thick line) over the terminal bulb of the pharynx shows rapid rises followed by slower decays; the rises are accompanied by muscular contraction (thin line), indicating that they are caused by a rise in calcium.

(B) The yellow and cyan channels separately show a relative reduction in cyan and increase in yellow intensity with contraction, as expected. However, each individual channel is affected by motion artifact noise, in contrast to the ratio in (A).

(C) Calibration of cameleon. A dissected head was exposed to the membrane permeant digitonin to give intracellular access, then exposed to solutions of 10mM calcium or 4mM EGTA to determine the maximum and minimum ratio. A typical trace is shown here. The maximum-minimum ratio change was 72 ± 4% averaged over 5 worms. Arrowheads indicate solution changes.

(D) Comparison of YC2.1 to YC3.1 in worms pumping at the same rate. The rate of decay is faster for YC3.1 (thin line) than YC2.1 (thick line), most apparent in the sharp transition between descending and rising ratios in YC2.1 that is more rounded in YC3.1, and indicative of a return to near-baseline for YC3.1 but not YC2.1 at the rate shown. This is consistent with faster in vitro kinetics for YC3.1 and sensitivity to lower calcium levels for YC2.1.

tobleaching (Figure 2.2b). Second, while gluing was effective at keeping the worm in the field of view, it was often not sufficient to completely immobilize the head without adversely affecting behavior. This problem could be overcome by manually updating a fixed region of interest each time the worm moves so that the region is always appropriately centered. However, manual tracking greatly limited the number of traces that can be analyzed and may introduce artifacts when comparing strains of worms that move more or less than wild-type. We therefore developed software to automatically track regions of interest while maintaining the proper offset between the two wavelength regions, which reduced noise (mean fluctuation during periods where there was no muscle contraction) to under 0.1% ratio change in most cases. Third, since cameleon is based on the endogenous calcium-binding protein calmodulin, there is a concern about cameleon expression affecting behavior. We were unable to distinguish wild-type worms from those with ljIs1 on the basis of observing pharyngeal pumping, and *ljIs1* did not have a starved appearance. We therefore concluded that the effect of cameleon expression on pharyngeal pumping behavior is minor. Photobleaching did not present technical problems; the loss of intensity was minor (less than 5% in 10s), and recovery was rapid enough to allow us to record for as long as the worm survived on the pad (up to five hours, recording 10s per minute).

The appearance of the ratio traces raised questions about relationship between the fluorescence ratio of cameleon and the calcium dynamics of the pharynx. We observed that it took much longer for the ratio to return to baseline than for the muscle to contract; a rapid series of contractions could cause the ratio to become significantly elevated from baseline. However, in worms expressing YC3.1, a cameleon with lowered affinity for calcium relative to YC2.1 [Miyawaki et al. 1997], the ratio changes were smaller and returned to baseline more rapidly (Figure 2.2d). One explanation for these observations is that the higher affinity of YC2.1 allows it to bind a larger fraction of the total calcium and lowers free calcium to the point where natural calcium export and sequestration mechanisms are affected. This would cause YC2.1 to have a larger ratio change with a slower decay back to baseline, as is observed. Alternatively,

the difference in rate might be a consequence of YC2.1 having slower kinetics of calcium release than YC3.1. Preliminary in vitro experiments in which Ca^{2+}-saturated cameleons were rapidly mixed with EDTA verified that YC2.1 had an approximately twofold slower off rate than YC3.1. These experiments also indicated that release kinetics of both cameleons were at least biexponential with a rapid release phase of approximately 100 s^{-1} that was not observed in worm imaging. Furthermore, the cyan and yellow channels had somewhat different slow-phase rate constants (cyan: $4.7 \pm 0.2\,s^{-1}$, yellow:2.6 ± 0.1 s^{-1} for YC2.1; cyan: 8.8 ± 0.2 s^{-1}, yellow 5.1 ± 0.1 s^{-1} for YC3.1), suggesting that a portion of the fluorescence change could be due to a conformational alteration of YFP or CFP rather than a change in FRET. Since accurate kinetic data is essential for determining exact calcium levels but is not for making quantitative comparisons between different fluorescence ratio measurements, we did not pursue a detailed investigation of cameleon kinetics. We have not yet attempted to analyze the decay phase given the difficulty of determining which factors were contributing to the observed shape. For our analysis of the rising phase, we continued to use YC2.1 in order to maximize our signal.

2.3.2 Quantitative monitoring of pharyngeal calcium transients

We next investigated whether we could quantitatively measure the duration and magnitude of calcium transients in the pharynx. We developed software to automatically extract mean ratio traces from stacks of images of a worm's terminal bulb, and to calculate the duration, total increase, and rate of increase for the rising phase of each calcium transient (Figure 2.3a). In order to interpret these parameters, we first investigated whether calcium buffering by cameleon needed to be corrected for. Although the dye concentration, as assayed by fluorescence intensity, varied by more than a factor of two between worms, we saw essentially no correlation between fluorescent intensity and the magnitude of changes (data not shown). This observation is consistent with the free calcium during calcium influx being set by endogenous buffers with relatively little impact from cameleon. We then attempted to determine whether the slope

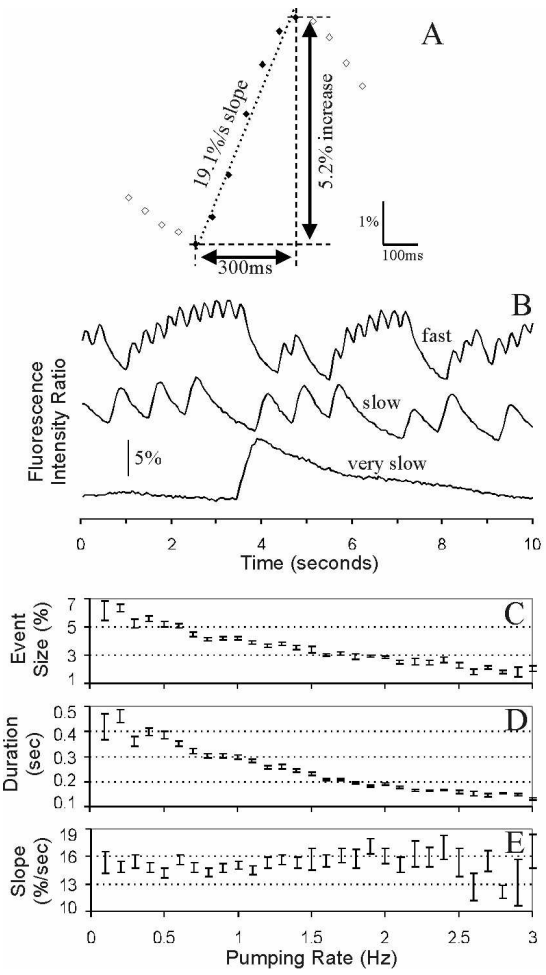

Figure 2.3: Characterization of Dependence of Calcium Transients on Worm Behavior
(A) Illustration of measured parameters for each transient. Duration is in multiples of the frame rate. Total increase is expressed in percent change in ratio. Rate of increase is computed by a least squares fit to the rising slope and has units of (percent change in ratio)/(time).
(B) Sample traces indicating fluorescence ratio traces typical of “fast” (>1.5Hz), “slow” (0.5-1.5Hz), and “very slow” (<0.5Hz) pumping behavior. Note that duration and total increase of transients is dependent on the pumping rate.
(C) Total ratio increase during transients is reduced at higher pumping rates. Ratio increase is calculated separately for each 0.1Hz increment in pumping rate; error bars indicate standard error at that rate. The linear correlation coefficient of pumping rate and total increase is -0.66.
(D) Total duration of transients is reduced at higher pumping rates. Data points and error bars are computed as in (C). The linear correlation coefficient of pumping rate and duration is -0.67.
(E) Slope of ratio increase during transients is relatively unaffected by pumping rate. Data points and error bars are computed as in (C). The linear correlation coefficient of pumping rate and slope is +0.05.

or the magnitude of the transients was more indicative of calcium influx levels. The rising phase of the transients is approximately linear with time in most cases (Figure 2.3a), which means that longer transients will have a greater magnitude simply by virtue of being longer. Two simple hypotheses can explain the approximately linear increase. The influx of calcium could lead to a steady increase in free calcium levels, in which case a greater influx would cause a more rapid increase, causing an increase in slope. Alternatively, the free calcium levels could be approximately constant during the transient and the steady increase could be an indication of the calcium-binding rate of cameleon; greater calcium influx in this case would alter free calcium levels, increasing the binding rate. Fortunately, although it is difficult to distinguish these two effects, both indicate that the slope of the transients is a monotonic increasing function of the calcium influx. This is sufficient to rank mutants in order of calcium influx.

Using our analysis software, we categorized the wild-type feeding behavior roughly into "fast" pumping (>1.5Hz), "slow" pumping (0.5Hz-1.5Hz), or "very slow" pumping (<0.5Hz) as shown in Figure 2.3b. Previous studies [Avery and Horvitz 1989, Raizen et al. 1995] have shown that rapid pumping requires input from pharyngeal neurons, while slow pumping can occur without neural input (very slow pumping in our assay appears to be a sign of impending death). To reduce the impact of alterations to neuronal behavior on our data, and to avoid an elevation of baseline ratio to a point where calcium release rates became significant compared to calcium binding rates, we focused our analysis on the slow pumping behavior. Analysis of ratio traces indicated that rapidly pumping pharynxes exhibited a smaller ratio change per contraction than slowly pumping pharynxes (Figure 2.3c). Likewise, the duration of the rising phase of the calcium transient was shorter during rapid pumping than during slow pumping (Figure 2.3d). However, the slope of the rising phase was independent of pumping rate (Figure 2.3e). Since the differences in the ratio increase between rapidly and slowly pumping pharynxes were proportional to the differences in duration, we concluded that they were simply a consequence of an extended duration of the calcium transient, as predicted by the steady-state approximation. In order to

verify that the observed differences in rate and transient parameters were not both a consequence of varying sensitivity to serotonin, we applied both double and half normal concentrations of serotonin; no significant change in the trends for or values of any parameter were observed (data not shown). We thus were able to calculate mean values for pumping rate and transient parameters in wild-type worms (Table 2.1).

2.3.3 Mutations in the calcium channel subunit EGL-19 affect the duration of calcium influx

The success of our characterization of wild-type worms motivated examination of calcium transients in mutants in the *egl-19* voltage gated calcium channel. *egl-19* encodes the structural (α1) subunit of the pharyngeal voltage-gated calcium channel [Lee et al. 1997]. Since the α1 subunit forms the pore of the channel, one would expect that mutations in *egl-19* could alter the duration or magnitude of calcium transients. *egl-19* null alleles are lethal, but both reduction-of-function and gain-of-function alleles have been identified in genetic screens [Trent et al. 1983, Avery 1993, Lee et al. 1997]. Electrical recordings from dissected mutant pharynxes have demonstrated that the gain-of-function alleles indeed cause extended depolarizations during muscle contraction, while loss-of-function alleles produce somewhat shortened depolarizations [Lee et al. 1997].

To aid comparison with previous electrophysiological results, we selected two gain-of-function alleles (*n2368* and *ad695*) and two reduction-of-function alleles (*n582* and *ad1006*) that had been previously characterized [Lee et al. 1997]. Each allele was crossed into the *ljIs1* background and recordings were made using the same protocol as for the original *ljIs1* strain. As shown in Figure 2.4 and Table 2.1, both *n2368* and *ad695* showed transients of increased duration. In fact, with the stronger allele, *n2368*, the transients frequently had an extended high-calcium plateau (Figure 2.4a, inset). Since the slopes of the transients were not greatly affected, the data suggests that the primary effect of the *n2368* and *ad695* mutant alleles is on the duration of the rising transient and/or the appearance of a plateau phase and not on other aspects of the

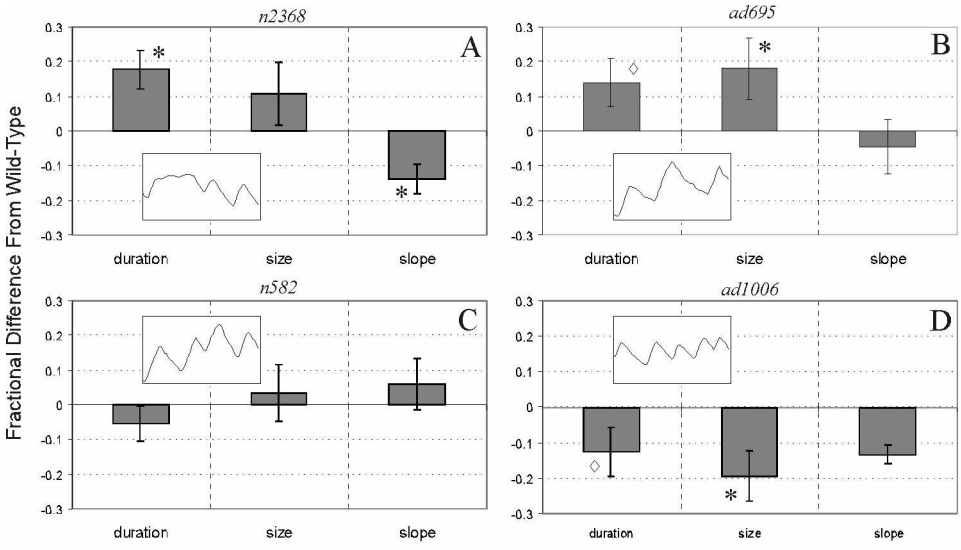

Figure 2.4: Altered Calcium Transients in *egl-19* mutants

Comparison of mutants with wild-type in worms pumping between 0.5Hz and 1.5Hz. Graphs indicate percent difference from wild-type for each parameter. Error bars indicate standard error of both mutant and wild-type. Diamonds indicate possible differences from wild type ($0.05<p<0.10$). Asterisks indicate significant differences from wild type ($0.005<p<0.05$). Insets show 3 seconds of a sample trace; the vertical axis of the inset corresponds to a 12% ratio change.

(A) Gain-of-function mutant *n2368* shows transients of extended duration and diminished slope relative to wild-type. The duration reflects the rising phase only and would be longer if calcium plateaus (inset) were included. The reduced slope may be an artifact of the arbitrary division made between rising and plateau phases.

(B) Gain-of-function mutant *ad695* shows transients of increased duration and total ratio increase; transient slope is not significantly different from wild-type.

(C) Loss-of-function mutant *n582* shows no significant changes in transient parameters from wild-type worms.

(D) Loss-of-function mutant *ad1006* shows transients of decreased duration and size relative to wild type; the data does not have a parametric distribution and hence the apparent decrease in slope is not statistically significant. As expected, the phenotype is opposite from the gain-of-function mutants.

calcium influx. As expected, *ad1006* showed a decreased calcium transient duration without a drastic change in slope, consistent with a partial loss-of-function phenotype. The parameters for *n582* were statistically indistinguishable from wild-type, suggesting that this mutation does not have a major effect on the calcium influx in the pharynx, although the mutation did decrease pumping rate (Table 2.1). Taken together, the close correspondence between our results and earlier electrical recordings supports the hypothesis that calcium is the major charge carrier during pharyngeal depolarization, and suggests that calcium imaging can play a valuable role in the analysis of calcium channel function.

2.3.4 UNC-36 voltage-gated calcium channel α2 subunit implicated in down-regulation of calcium transients

Calcium channels in both vertebrates and C. elegans also contain a number of associated subunits that presumably are involved in dynamic regulation of the channel's activity or static alteration of its properties. For example, all known calcium channels contain a large subunit called α2, a glycosylated integral-membrane protein. The *unc-36* gene encodes a putative α2 subunit of pharyngeal calcium channels [Lobel and Horvitz 1997], and mutants defective in this gene have an observable pharyngeal pumping defect [Brenner 1974, Avery 1993]. This suggests an important role for the UNC-36 protein in the pharynx, yet little is known about the role of the α2 subunit in the muscle cells of nematodes or other animals.

To determine if *unc-36* mutations affect pharyngeal calcium transients, we constructed strains containing a mutant allele of *unc-36* and the *ljIs1* integrated array. In two different *unc-36* loss-of-function mutants analyzed (*e251* and *ad698*), the average rate of pumping was reduced relative to wild-type (Table 2.1). Calcium imaging demonstrated that the *unc-36*(*e251*) allele caused a dramatic increase in the slope of the transients without altering their duration (Figure 2.5a). Likewise, the effect of allele *ad698* was to increase the slope without a major effect on duration (Figure 2.5b). To verify that the difference in slope was not caused by a difference in sensitivity of

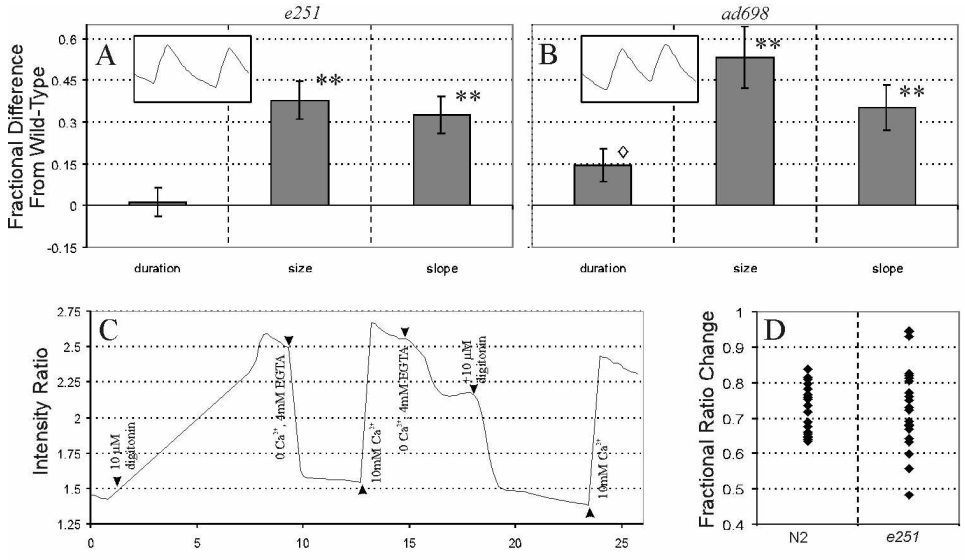

Figure 2.5: *unc-36* Mutants Show Larger Calcium Influx

Comparison of mutants with wild-type in worms pumping between 0.5Hz and 1.5Hz. Graphs indicate percent difference from wild-type for each parameter. Error bars indicate standard error of both mutant and wild-type. Double asterisks indicate highly significant differences from wild type ($p<0.005$). Single asterisks indicate significance ($0.005<p<0.05$). Diamonds indicate possible significance ($0.05<p<0.10$).

(A) Allele *e251* shows markedly larger transients than wild-type worms ($p<0.005$) without a corresponding change in the duration of contractions. Inset shows a sample trace (horizontal length is 3 seconds; vertical length is 12% ratio change).

(B) Allele *ad698* likewise shows larger transients ($p<0.005$) and slope ($p<0.005$) with a possible smaller increase in duration of contractions ($0.05<p<0.10$). Inset shows a sample trace (horizontal length is 3 seconds; vertical length is 12% ratio change).

(C) Control verifying that cameleon is functioning properly in the *e251* background. A dissected head is exposed to digitonin and placed alternately in solutions of 10mM Ca^{2+} or 0 Ca^{2+} + 4mM EGTA to determine maximal and minimal fluorescence ratio. An example trace is shown; over five worms, the maximal ratio was a mean of $73 \pm 11\%$ over the minimal ratio. Arrowheads indicate solution changes.

(D) Comparison of control maximal/minimal ratios for wild-type and *e251*. Each dot indicates one max/min ratio measurement. Left column is wild-type, right is *e251*. The observed pattern is inconsistent with *e251* having a 30% larger response than wild-type ($p < 0.01$).

YC2.1 in an *unc-36* background, we measured the dynamic range of cameleon in the *e251* background; an example trace is shown in Figure 2.5c. No difference between N2 and *e251* was detected in the dynamic range (Figure 2.5d), indicating that the difference in slopes was not due to a higher proportion of inactive cameleon in the *unc-36* background. There also was no difference between baseline ratios (1.410 ± 0.020 for N2, 1.436 ± 0.029 for *e251*), which indicates that the difference is not due to increased responsiveness caused by a greater proportion of calcium-free indicator at baseline in *e251*. Although we cannot rule out an *unc-36* background altering endogenous buffers such that free calcium during calcium influx is elevated even though the influx itself is normal, since *unc-36* is a calcium channel subunit, the most parsimonious explanation is that the effect is on calcium influx itself. Thus, our imaging experiments indicate that loss of *unc-36* function leads to an increase in the magnitude of pharyngeal calcium transients, and suggests that the $\alpha 2$ subunit of the calcium channel might function to negatively regulate the calcium flux into the pharynx.

		Transient Parameters		
Strain	Pumping Rate	Duration	Ratio Increase	Slope
N2 (wild type)	1.16 ± 0.08 Hz	295 ± 10 ms	$4.31 \pm 0.6\%$	$15.9 \pm 0.8\%$/s
		Percentage difference from wild type		
egl-19(n2368)	0.60 ± 0.09 Hz**	$+17.7\% \pm 5.6\%$*	$+18.8\% \pm 9.0\%$	$-13.9\% \pm 4.3\%$*
egl-19(ad695)	1.12 ± 0.12 Hz	$+14.0\% \pm 7.0\%^{\diamond}$	$+18.0\% \pm 9.0\%$*	$-4.6\% \pm 7.9\%$
egl-19(n582)	0.71 ± 0.08 Hz**	$+5.4\% \pm 5.2\%$	$+3.4\% \pm 8.3\%$	$+5.9\% \pm 7.3\%$
egl-19(ad1006)	1.20 ± 0.11 Hz	$-12.6\% \pm 7.0\%^{\diamond}$	$-19.4\% \pm 7.0\%$*	$-13.3\% \pm 2.6\%$
unc-36(e251)	0.58 ± 0.09 Hz**	$+1.2\% \pm 5.0\%$	$+37.9\% \pm 6.7\%$**	$+32.6\% \pm 6.5\%$**
unc-36(ad698)	0.38 ± 0.04 Hz**	$+14.5\% \pm 5.8\%^{\diamond}$	$+53.3\% \pm 11.0\%$**	$+35.1\% \pm 8.0\%$**

Table 2.1: Parameters for calcium transients during pharyngeal pumping for wild-type and mutants.
Values are mean $\pm$ S.E.M.; n varies by strain. Significance levels are determined using the Mann-Whitney rank sum test. All measurements were made on adult hermaphrodites in 1mg/mL serotonin on hydrated 2% agarose pads. Diamonds indicate borderline significance ($0.05<p<0.1$). Single asterisks indicate moderate significance ($0.005<p<0.05$). Double asterisks indicate high significance ($p<0.005$).

2.4 Discussion

2.4.1 Cameleon is a viable sensor for investigating muscle cell physiology in vivo

We have shown that ectopically expressed cameleon can be used to detect and measure calcium transients in the pharynx of live *C. elegans*. These transients are reliably detected, and parameters describing both the duration and level of elevated calcium can be calculated for worms of a given strain. Furthermore, we have shown that this method is sufficiently sensitive to identify mutants that display measurably different calcium dynamics than do wild-type worms.

In addition to the pharyngeal muscle, *C. elegans* contains a number of specialized muscle groups, each dedicated to a particular behavior. In the hermaphrodite, these include the body wall muscles (involved in locomotion), the defecation muscles (involved in defecation), the oviduct muscles (involved in ovulation), and the vulval muscles (involved in egg-laying) [White 1988]. The functional activities of these muscle groups are known to be regulated by a diverse array of neuromodulators. Moreover, a large number of mutants have been described that affect these various behaviors, and the genes defined by these mutations encode potential components of signaling pathways that might regulate muscle excitation and/or contraction. Calcium imaging using cameleon provides a powerful tool for distinguishing mutants that affect calcium influx from those that affect contractile duration without otherwise altering calcium dynamics, and from those that have normal calcium dynamics but abnormal contraction. Using this technique, it should therefore be possible to identify genes whose products regulate calcium channel activity in muscles and to study their effects in vivo, and thereby gain insight into the mechanisms of calcium channel regulation.

2.4.2 Insights into the function of calcium channel subunits

We determined that mutations affecting two subunits of the pharyngeal voltage-sensitive calcium channel altered the dynamics of calcium influx during feeding. Mu-

tations in *egl-19*, which encodes the α1 subunit, affected the duration of the calcium transient without having other major effects on the calcium influx. The duration increases in gain-of-function alleles *n2368* and *ad695* are consistent with prior electrical recordings [Lee et al. 1997], as is the duration decrease in loss-of-function allele *ad1006*. The loss-of-function allele *n582*, which has subtle electrical defects and visually appears to have "weak" contractions, did not appear to have significantly different calcium transients than wild-type despite a decreased average pumping rate. It is possible that *n582* does have a physiologically important effect on calcium in the pharynx, but that the change was below our ability to detect. Alternatively, the mutation may affect the activation potential of the channel or otherwise affect excitability. Analysis of other alleles, preferably using both calcium imaging and electrical techniques, may provide insight into the relationship between the structure of α1 subunits and their activity.

Analysis of mutants in *unc-36* also provided an interesting insight into the possible function of the α2 subunit. *unc-36* mutants show two visible abnormalities in feeding behavior [Avery 1993]. First, in contrast to wild-type, *unc-36* mutants are unable to pump at high frequency in the presence of food or serotonin. Since neuronal input is required for rapid pumping, and since many mutants with specific defects in fast pumping are known to be deficient in synaptic transmission, this aspect of the *unc-36* feeding phenotype is probably due to a lack of neuronal *unc-36* function. Second, *unc-36* mutants also exhibit an abnormality in the pattern of pharyngeal muscle contraction, a phenotype known as the "slippery pharynx". Since the slippery pharynx is not a hallmark of synaptic transmission mutants, and since GFP reporters indicate that *unc-36* is expressed in the pharynx itself [T. Tam and W. Schafer, unpublished], it is logical to suppose that this phenotype results from a defect in the muscle itself. However, the visible phenotype of *unc-36* provided little insight into how it might affect the activity of calcium channels in the pharyngeal muscle. Cameleon imaging showed that loss-of-function alleles of *unc-36* caused increased calcium influx. This indicated that the α2 subunit directly or indirectly functioned as a negative regulator of calcium influx in the pharynx. Potentially, UNC-36 could physically affect the α1 subunit and be a site of

regulation itself. Alternatively, it could interact with negative regulators that acted on the $\alpha 1$ subunit, or it could be required for proper localization of or increased turnover of the channel complex. Overexpression studies in Xenopus oocytes and vertebrate cell culture have shown that the $\alpha 2$ subunit both increases the conductance and the rate of inactivation of coexpressed $\alpha 1$ channels, especially when the β subunit is coexpressed [Singer et al. 1991, De Waard and Campbell 1995, Bangalore et al. 1996]. Our results are consistent with an inactivation defect that leads to increased calcium influx, though we saw no evidence for decreased conductance. Although more work would be needed to distinguish between these and other possibilities, this finding illustrates the benefit of calcium imaging, as there was no way to infer the effect of this protein on calcium dynamics from its behavioral phenotype alone.

2.4.3 Technical considerations for calcium imaging with cameleon

Our experimentation with different imaging systems provided a number of lessons about the technical requirements for cameleon imaging in behaving organisms where calcium changes occur rapidly. Perhaps the most important aspect of an effective system is the ability to perform video-rate ratiometric imaging. The susceptibility of the individual wavelength traces to movement artifacts and photobleaching makes it critical to obtain simultaneous measurements of both emission wavelengths at a speed adequate to detect relatively brief events. An emission splitter as used here, unlike a filter wheel system, records the two images simultaneously on a single CCD at the full frame rate of the camera, although the field of view is reduced twofold. Video-rate confocal and two-photon microscopes with nonimaging detectors [Tsien and Backsai 1995, Fan et al. 1999] are important alternatives to split-emission CCDs and provide the advantages of optical sectioning, stroboscopic illumination, and inherent registration of the two emission wavelengths. Preliminary trials with video-rate two-photon excitation microscopes showed pharyngeal Ca^{2+} transients similar to those characterized here, but the CCD system proved more reliable and better in signal-to-noise with less photobleaching, probably because the wide-field observa-

tion could collect more photons from a greater thickness of sample volume. In our very transparent preparation, targeted gene expression already restricted the cameleon quite accurately to the tissue of interest, so the optical sectioning capability of confocal or two-photon imaging was unnecessary or even counterproductive for maximizing photon collection. The ability of two-photon excitation to confine photobleaching to just the plane of focus was of little value when that plane was being observed constantly and when diffusion of unbleached indicator molecules from other planes was probably quite slow, as expected for a ~70 kDa protein. However, many other preparations and biological questions will still require confocal or two-photon excitation instruments.

2.4.4 Prospects for using cameleon in other cell types

Calcium imaging using cameleon is in principle applicable to a wide variety of tissues in *C. elegans*. For example, intestinal cells, which are neither muscular nor neuronal, have recently been implicated in control of the periodic defecation of the worm [Dal Santo et al. 1999]. Transient increases in calcium were observed in intestinal cells injected with fura-2; these transients preceded the first defecation-related muscle contractions. However, due to the technically challenging nature of the injection procedure, it was only possible to inject and image from a single intestinal cell in each animal. Intestinal expression of cameleon would allow transients to be monitored over the entire length of the intestine simultaneously, which would help determine the nature of spatial coordination of intestinal calcium transients. Also, avoiding the step of single-cell injection would greatly facilitate the analysis the calcium transient phenotype of known defecation-defective mutants. Since the intestine is comparable in size to the pharynx, has several strong cell-type specific promoters, and is known to undergo robust calcium transients, cameleon imaging should be possible in this tissue without substantial modification to the methods described here.

We found (see section 3.3.1) that electrical stimulation could reliably induce visible ratio changes in neurons. Thus, it should be possible to use cameleon-based calcium

imaging to study voltage-gated calcium channel function in neurons, as we have begun to do in the pharynx. Moreover, if a single neuron were driven electrically, the response of its synaptic partners could be recorded to begin building a map of functional connectivity to complement the known physical connectivity [White et al. 1986]. This approach would also allow noise to be averaged out over multiple trials and could enhance comparisons between small ratio changes. The ability to simultaneously monitor the activity of multiple identified neurons in an intact behaving animal would be enormously useful for understanding the cellular basis of behavior. Existing protocols for recording electrically from *C. elegans* neurons involve slicing open or rupturing the cuticle to expose a cell of interest, so an electrical alternative is not immediately obvious. Electrophysiology in *C. elegans* and another nematode, *Ascaris*, indicate that calcium is the main carrier of inward positive current [Davis and Stretton 1989, Goodman et al. 1998], and the *C. elegans* genome contains no recognizable voltage-gated sodium channels [Sequencing Consortium 1998, Bargmann 1998]. Thus there is little doubt that neuronal calcium transients are ubiquitous in *C. elegans*. Since neuronal cell bodies in *C. elegans* are small (~2μm diameter), in vivo recordings from neurons are more difficult to obtain than muscle recordings due to increased sensitivity to movement and background noise. Nonetheless, neuronal activity in response to the application of a stimulus-an odorant or neurotransmitter, for instance-should be detectable without major modifications to the protocol used here. Additionally, with further optimizations to the imaging equipment, protein expression levels, and recording protocols, detection of neuronal calcium transients in intact *C. elegans* may be practical even in the absence of pairing with a stimulus.

Although *C. elegans* is particularly suited to cameleon imaging due to its transparency and facile genetics, this method may be useful in other organisms as well. For example, *Drosophila* has equally powerful genetics and a even more diverse set of cell-type specific promoters to direct localized cameleon expression. Moreover, although still relatively small, the neurons of *Drosophila* are somewhat larger, and may contain larger calcium transients, than the neurons of *C. elegans*. While the opaque exoskeleton

of *Drosophila* may make imaging from intact adult animals difficult, existing methods for recording from larvae should be applicable, and strong promoters may facilitate imaging in all developmental stages [Sun et al. 1999]. Other genetically manipulable organisms, such as mouse, present their own set of challenges as well as potential advantages for use of cameleon in imaging studies. Further modification of the methods described here should make it possible to overcome these species-specific challenges and realize the prospective power of genetically encoded sensors as probes for nervous system function.

2.5 Experimental Procedures

2.5.1 Construction of cameleon expression plasmids

A pharyngeal-specific expression vector was constructed using the backbone of the Fire Lab '97 Vector Kit plasmid L3613, the promoter sequence of the *myo-2* gene, and the coding sequence of either yellow cameleon 2.1 or yellow cameleon 3.1. Restriction sites BamHI and EcoRI were used to remove the existing promoter and coding sequence from L3613. PCR was used to amplify the *myo-2* promoter from C. elegans genomic DNA using primers 5'-GGATCCGAGGCATTTGAATTGGGGGTGGTGG-3' and 5'-AAGCTTCTGTGTCGGACGATCGAGGG-3' corresponding to 1170 base pairs upstream of the translation start site, and sufficient for pharyngeal-specific expression according to [Okkema et al. 1993]. Primers include a 5' BamHI site and a 3' HinDIII site. The cameleon coding sequence was removed using HinDIII and EcoRI, and the cameleon, promoter, and backbone fragments were ligated to produce the final expression vector. A neuronal-specific expression vector was constructed in the same manner. PCR was used to amplify 2355 base pairs upstream of the *unc-119* translation start site; the primers used were 5'-GGATCCCTCTTGGGGAAAACGGGCG-3' and 5'-GCTCTGCCTTCATATAAGCTTTTGTAGCTG-3'.

2.5.2 Construction of transformed strain of *C. elegans* carrying cameleon expression plasmid

Purified plasmid DNA of the pharyngeal expression vector was injected into *dpy-20*(*e1282ts*) worms along with a co-injection marker plasmid carrying the *dpy-20*(+) gene according to the protocol in [Mello and Fire 1995] to obtain a strain carrying the expression vector on an extrachromosomal array. The strain carrying YC2.1 was then subjected to gamma-ray irradiation as outlined in [Mello and Fire 1995, p. 467] to generate a strain carrying an intrachromosomal array. Two independent integrants were obtained. Both showed strong tissue-specific expression of the protein; one of the two (*ljIs1*) was used for all crosses. The neuronal expression vector was introduced similarly, but not irradiated to give an intrachromosomal array, generating the extrachromosomal array *ljEx3*.

2.5.3 Optical recordings

Optical recordings were performed on a Zeiss Axioskop with a PentaMAX EEV 512x1024 CCD camera (Princeton Instruments). A MultiViewer emission image splitter (Princeton Instruments) was used to display two wavelengths simultaneously on the single CCD chip. Recordings were made on a 100MHz Pentium running MetaFluor 3.6 (Universal Imaging) under Windows 95. A 40x water immersion objective (Olympus) was used for all recordings. For most recordings, 50msec/frame exposures were taken with 4x4 binning. Image stacks were occasionally converted to ratio pairs for visual inspection using the PI MultiViewer plugin for MetaFluor. Fluorescence ratio measurements were made using custom software described below. Filter/dichroic sets consisted of: excitation (405nm, 40nm bandwidth), cyan emission (483nm, 25nm bandwidth), yellow emission (535nm, 25nm bandwidth), and 510nm dichroic mirrors.

2.5.4 Dissected head sample preparation and recording

Individual worms were transferred to a dried agarose pad on a coverslip to immobilize them and were covered with halocarbon oil to prevent dehydration. A razor was used to sever the head just posterior to the pharynx, exposing the pharynx to external solutions. The severed head was skewered through the cuticle using a glass microinjection needle and transferred to C. elegans intracellular saline solution containing 136.5mM potassium gluconate, 17.5mM potassium chloride, 9.0mM sodium choride, 1.0mM magnesium choride, 10mM HEPES at pH 7.2 [Avery et al. 1995]. An initial application of 20μM digitonin was used to provide intracellular access; the bath solution was then switched repeatedly between intracellular saline with 0 Ca^{2+} + 4mM EGTA and 10mM Ca^{2+}. Images were taken at 0.1Hz during these experiments; solutions were switched after the ratio had reached a plateau. Occasional reapplication of digitonin was needed to maintain good intracellular access. Analysis was performed online in MetaFluor by measuring the fluorescent intensity of each wavelength over the terminal bulb of the pharynx. After recording was complete, the image stack was analyzed with the custom measurement software described below.

2.5.5 Whole worm sample preparation and recording

Six to ten worms were transferred to a hydrated 2% agarose pad in M9 solution with 1mg/mL serotonin and partially immobilized by using a drawn capillary tube to dot cyanoacrylate glue on or near their tails. An additional 5 μL of 1mg/mL serotonin in M9 was added to keep the sample hydrated during recordings and induce pharyngeal pumping [Avery and Horvitz 1990]. Worms whose heads or entire bodies were accidentally mired in glue were not used in the recordings. In most cases, two worms were recorded from each pad. Each pharyngeal recording consisted of twenty 10s image streams at 20Hz, taken one minute apart. This protocol allowed sufficient time (50s) for the images that had been streamed to RAM to be stored on the computer hard drive. Neuronal recordings ranged from 3-5 seconds per neuron, with several

widely separated neurons imaged in each worm; sample preparations were otherwise identical.

2.5.6 Automated extraction of mean fluorescence ratio from image series

To facilitate the rapid analysis of large numbers of image stacks, a command-line Windows 95 program was designed that extracts the mean fluorescence ratio from each frame in the stack. The fundamental operation of the program is to locate the center of the target tissue with sub-pixel accuracy. In the case of the pharynx, which was unambiguously the brightest object in the field of view, an approximate location was determined using that criterion. For neuronal data, the approximate initial position of each neuron of interest was specified by hand. The exact position is then computed iteratively by computing the intensity-weighted center of a region of interest large enough to encompass the target tissue and updating the region center if the intensity-weighed center differs significantly from the region center. The optical splitting of the two wavelengths does not produce a perfect bisection of the CCD array and can change slightly from day to day. Therefore, the program has the ability to compute the mean difference in position between two regions of interest and use that difference to determine the offset between the two wavelength images. Once an offset is specified, for each frame in the stack the center of the tissue of interest can be computed as described above. A single region of interest is used for the neuronal recordings, while a series of concentric circles are taken about the center of the pharynx; average intensity is measured for each and output to a log file. The smallest circle entirely containing the pharynx (judged by recording noise, which is reduced when the circle does not intersect the pharynx) was used for further analysis; this usually corresponded to a radius of eleven pixels. Optimal region size for neurons was determined by hand. Sub-pixel resolution is achieved by interpolating between adjacent pixels; this prevents excessive noise from single pixels flickering in and out of the region of interest from frame to frame.

2.5.7 Detection and measurement of transients in fluorescence ratio

The numerical computation and matrix manipulation program GNU Octave, an open source clone of MATLAB (The MathWorks, Inc.), was used for all data processing. The intensity was ratio from the average intensity log file described above; then the derivative of the ratio was calculated and smoothed by using an 8Hz triangular window. With 20Hz data, this turned out to be equivalent to averaging adjacent measurements. Empirically, transient rises in calcium accompanying pharyngeal contraction were observed to last at least 100ms and to have a rate of rise of at least 5%/sec. Smaller transients would have been difficult to distinguish from noise by eye, and automatic detection of transients using the 5%/sec criteria seemed as reliable as making measurements by eye. One exception was in mutants with very extended contractions; for those, only the initial rise was detected, not the extended elevated plateau. The entire transient was considered to be all frames surrounding the triggering frames (two adjacent rises of at least 5%/sec) that either showed an increase in ratio themselves or were immediately between rises of at least 5%/sec. The duration, maximum increase, and slope of each transient was recorded. Duration was considered to be (frame rate) $\times$ (number of frames in transient - 1). Maximum increase was calculated as (highest ratio in transient) - (lowest ratio in transient). Slope was calculated by a least-squares fit to the trace during the transient.

2.5.8 Statistical analysis of recording parameters

Variation in the three parameters measured for each transient was observed from transient to transient, trace to trace, and worm to worm within the same train. Worm behavior-the average rate of pumping-was observed to change in many cases over the duration of the 20 minute recordings. However, within each 10s recording stream, behavior seemed fairly stable. Therefore, mean duration, increase, and slope of transients were calculated for each 10s stream. Since there was worm-to-worm variation, statistical comparison had to be at the worm level. Since the parameters were affected

by the worm's pumping rate, only streams with the appropriate pumping rate (0.5-1.5Hz) were considered. Further, when wild-type and mutant worms were compared, streams were excluded until both data sets contained the same number of streams at each frequency. The resulting rank-normalized streams were then averaged worm-by-worm. The values for the wild-type worms and those for that mutant strain were compared for statistically significant differences by using the non-parametric Mann-Whitney rank-sum test. One should note that since multiple comparisons were made to wild-type, a result of $p<0.05$ is valid only for the exact comparison being made. If the data were to be treated as a survey of mutants to catalog which were different from wild-type, the non-parametric Dunnett's test should be used instead. The Mann-Whitney test was used for simplicity, but as with any pairwise test, if there are enough comparisons a result of $p<0.05$ occurring somewhere would be expected by chance. To calculate mean values and parametric deviations for each strain, mutant data was normalized for pumping rate against wild-type as described above. The mean and standard error for each worm was calculated, then the results for each worm were used to calculate the mean for the strain. Error was taken to be the standard error on the average over the worms, plus the error propagated from each worm using the standard formula for propagation of error.

2.5.9 Kinetic measurements of cameleon

Solutions containing 10mM Tris, 500μM Ca^{2+}, and 5μM YC2.1 or YC3.1, at pH8, were mixed with equal volumes of 10mM Tris, 4mM EDTA, at pH 8, using a stopped-flow fluorimeter (Applied Photophysics). Fluorescence intensity in cyan and yellow wavelengths were measured in separate experiments using an excitation monochromator at 405nm (5nm bandwidth) in each case and 483nm (25nm bandwidth) and 535nm (25nm bandwidth) emission filters for cyan and yellow, respectively. The sampling rate was 2kHz for the first 200 data points (100ms) and 200Hz for an additional 200 data points (1000ms). Curve fitting to determine relaxation times was performed on the software package SigmaPlot (Jandel Scientific).

2.6 Acknowledgements

We are grateful to Mark Ellisman for the use of his video-rate two-photon microscope for neuronal imaging, and to Gary Fan for assistance in using the scope; and to Joseph Adams for the use of his stop-flow fluorimeter to analyze the in-vitro kinetics of cameleon. We also thank Leon Avery and the Caenorhabditis Genetics Center for strains, and Tim Yu and members of our labs for discussions. This work was supported by grants from the National Science Foundation (IBN-9723250), the National Institutes of Health (DA11556), the Joseph and Esther Klingenstein Foundation, the Alfred P. Sloan Foundation, and the Arnold and Mabel Beckman Foundation (to W.R.S.), predoctoral training grants from the Markey Foundation and the National Institutes of Health (to R.K.), and grants from the National Institutes of Health (NS27177) and the Howard Hughes Medical Institute (to R.Y.T.).

The text of this chapter, up to this point, is a reprint of the material as it appears in Neuron in the article "Optical imaging of calcium transients in neurons and pharyngeal muscle of C. elegans." Neuron *26*, 583-594 by Kerr, R., Lev-Ram, V., Baird, G., Vincent, P., Tsien, R.Y., Schafer, W.R. (2000). The material has been reformatted to fix references and to fit this format, and the original Figure 3 and the text describing electrical stimulation of neurons has been moved to Chapter 3 where it fits more naturally with subsequent work. The dissertation author was the primary researcher and author and the co-authors listed above contributed advice and technical expertise and in part directed and supervised the research which forms the basis for Chapter 2.

Chapter 2 was reprinted from Neuron, Vol. 26, Kerr, R., Lev-Ram, V., Baird, G., Vincent, P., Tsien, R.Y., Schafer, W.R., Optical imaging of calcium transients in neurons and pharyngeal muscle of C. elegans, Pages 583-594, Copyright (2000), with permission from Elsevier Science.

2.7 Application of Muscle Imaging: Detecting Vulval Muscle Activity

2.7.1 Introduction

Egg-laying in *C. elegans* hermaphrodites is a regulated intermittent process that is inhibited by high salt or an absence of food and is stimulated by the presence of serotonin [Chalfie and White 1988]. Under normal conditions with food present, the worm is either in an inactive state, during which eggs are not laid, or an active state, during which eggs can be laid [Waggoner et al. 1998]. In the active state, egg-laying models as a Poisson process with a time constant of approximately 20 seconds; the transition from the inactive state to the active state also models as a Poisson process with a time constant of approximately 20 minutes [Zhou et al. 1998]. The transition from the inactive state to the active state is regulated by serotonin; application of exogenous serotonin causes the animals to remain constantly in the active state, while serotonin-deficient mutants cause a significant decrease in the rate of transition from the inactive state to the active state [Waggoner et al. 1998]. Laser ablations of the neurons in the egg-laying circuits suggest that serotonin acts directly on the vulval muscles, and therefore that the state of the vulval muscles determines the egg-laying behavioral state.

Observation with DIC optics shows that an egg-laying event does not occur every time the vulval muscles contract. However, direct observation of the single-cell vulval muscles is difficult even with DIC optics. Further, the muscles can contract repeatedly too rapidly to be scored by hand, necessitating an automated approach. Pharyngeal muscle activity is easily measured using cameleon to detect calcium transients [Kerr et al. 2000], so we decided to use a similar approach to measure vulval muscle activity.

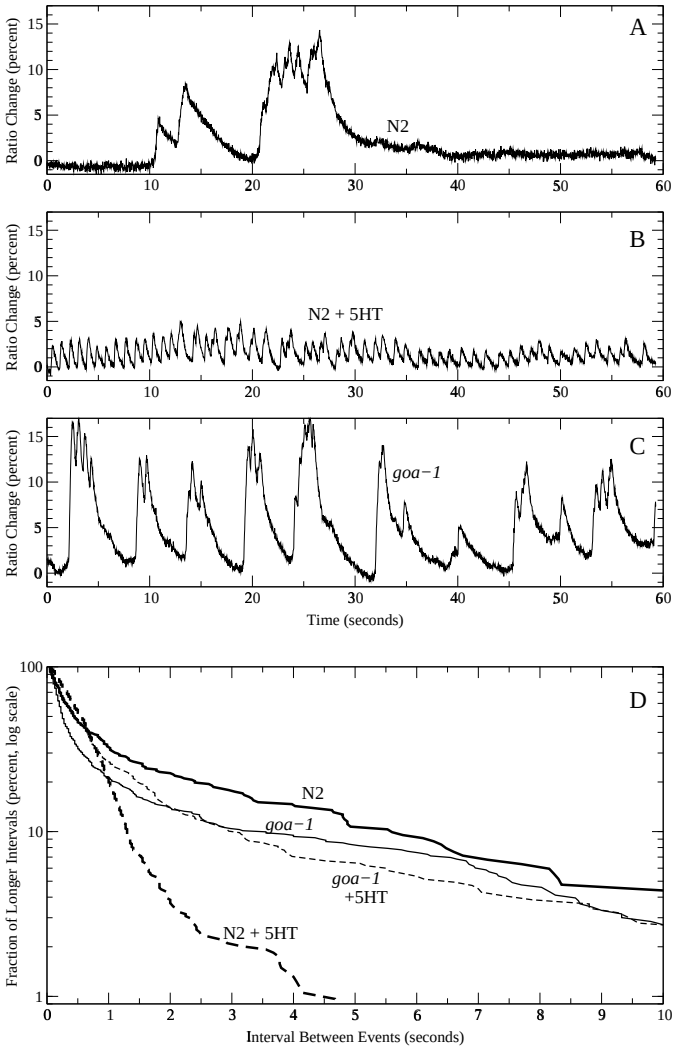

Figure 2.6: Spontaneous and serotonin-induced activity of the vulval muscles.
(A) Vulval muscles in wild-type worms show intermittent clusters of activity in worms glued to 2% agarose pads made of Dent's saline.
(B) Application of serotonin causes rapid semi-regular activity in the vulval muscles.
(C) Worms carrying a mutation in the G-protein *goa-1* show an increased rate of clusters, consistent with the behavioral phenotype of hyperactivity and constitutive egg-laying.
(D) Comparison of the effects of serotonin on wild-type and *goa-1* worms. Log-tail distributions of the intervals between calcium transient events are plotted for wild-type (thick lines) and *goa-1* (thin lines) both off (solid lines) and on (dashed lines) 0.5mg/mL serotonin. Wild-type worms show very few long intervals between transients when placed on serotonin (<1% intervals longer than 5s, as compared to ~5% intervals longer than 10s off drug). *goa-1* worms show a slight shift towards shorter interval times compared to wild-type off drug, but are largely resistant to the effects of serotonin. The primary effect of serotonin on *goa-1* worms appears to be to reduce the fraction of very short intervals.

2.7.2 Serotonin increases *C. elegans* vulval muscle activity

In order to detect calcium transients in the vulval muscles, we used a line of worms expressing yellow cameleon 2.0 under control of the *myo-3* promoter, a generous gift from Tim Yu of the Bargmann lab. *myo-3* drives expression in the body wall muscles as well as the vulval muscles [Okkema et al. 1993], but the interference from the body wall is minor when imaging the vulval muscles. Although the conditions required for microscopy are inhibitory to egg-laying, we observed intermittent activity in the vulval muscles in wild-type animals even in the absence of serotonin (Figure 2.6a). This activity typically took the form of large calcium transients with small spikes of calcium superimposed on top. Addition of 0.5mg/mL (1.3mM) serotonin caused the muscles to exhibit nearly continual activity consisting of small calcium spikes (Figure 2.6b), consistent with its proposed role in switching the vulval muscles into an active state. In contrast to observation with DIC, these fluorescent signals were relatively clear and quantifiable, even upon addition of serotonin where the muscles visually appear at best to twitch very slightly, highlighting the utility of cameleon as an indicator of single cell activity.

How might serotonin act to increase the activity of the vulval muscles? The *goa-1* gene, which encodes an α subunit of the *C. elegans* G_o, is expressed in the vulval muscles and in most tissues shows a mutant phenotype opposite from the effect of serotonin [Segalat et al. 1995, Mendel et al. 1995]; *goa-1* mutant animals are resistant to the effects of serotonin, suggesting that serotonin acts through G_o. However, curiously, *goa-1* mutants show increased rates of egg-laying despite their serotonin-resistance, suggesting an antagonistic G_o activity. To examine this phenotype in more detail, we crossed the loss-of function allele *goa-1(n1134)* into lines carrying the *myo-3::YC2.0* expression construct. In the absence of serotonin, *goa-1* animals showed a vulval muscle activity pattern similar to wild type (Figure 2.6c). However, the level of activity was substantially increased; on average we observed ~6 calcium transients (large rises plus small spikes) per minute in wild-type, as compared to ~27/min in *goa-1* animals. Sero-

tonin had little effect on the *goa-1* mutants (Figure 2.6d) as compared to the effect on wild-type. Thus *goa-1* appears to be necessary for serotonin to induce continual spiking, even though loss of *goa-1* causes increased clustered activity. One explanation for this observation is that *goa-1* acts in opposite ways in muscle and in neurons. Alternatively, the increased activity in *goa-1* mutants may be a developmental compensation to increase baseline activity to compensate for a lack of activity evoked from endogenous serotonin release. A third possibility is that a mutation in *goa-1* causes both serotonin-resistance and increased activity in the vulval muscles regardless of neuronal input.

To distinguish the three possibilities, we are currently recording from animals in which the neuronal inputs to the vulval muscles are ablated. If the increased activity in *goa-1* animals is because of an effect on neurons, ablated animals should show a similar low level of activity in both a *goa-1* and wild-type background. If the vulval muscles are compensating for a lack of serotonergic input, laser or genetic ablation of the serotonin-releasing HSN neuron should give a similar increase in spontaneous activity in both wild-type and *goa-1* backgrounds. Finally, if the effect of *goa-1* is entirely specific to the vulval muscles, the ablated animals should show the same phenotype as unablated, namely, increased baseline activity in the mutant as compared to wild-type.

2.7.3 Experimental technique

Adult hermaphrodites were glued on 2% agarose pads dissolved in Dent's saline as described in section 2.5.5. For drug experiments, 5-hydroxytryptamine was added to the 2% agarose solutions along with a small volume of NaOH to correct for acidification. Calcium imaging was performed as described in section 3.5.2. Events were detected using a peak finding algorithm based on the methods described in section 4.4. For presentation purposes, traces were corrected for ~15%/min photobleaching using an algorithm based on Eq. (4.27).

2.7.4 Acknowledgements

All work in section was performed by Stanley Shyn, a graduate student in the Schafer lab, save for the initial verification that vulval muscle calcium transients were visible in wild-type worms, and the creation of photobleaching correction and event-detection algorithms and MATLAB scripts, which were performed by the author of the dissertation. We would like to thank Tim Yu of the Bargmann lab for providing lines of worms containing the *myo-3::YC2.0* expression construct.

Chapter 3

In Vivo Imaging of Induced Activity in *C. elegans* Mechanosensory Neurons

3.1 Summary

Caenorhabditis elegans senses gentle mechanical stimuli along its body wall with a set of six touch receptor neurons. Although the role of these cells in regulating behavior has been determined using genetic and cell ablation studies, the activity and response properties of the neurons themselves are not well understood due to the difficulty in making electrical recordings in *C. elegans*. Here we report an initial characterization of the response properties of the ALM touch neuron using the calcium indicator cameleon to make optical recordings of stimulus-induced calcium transients in intact worms. We show that ALM is primarily an all-or-none motion sensor rather than a pressure or deformation sensor, and that ALM activity requires the putative mechanoreceptor subunit *mec-4*, a member of the DEG/ENaC family known to be expressed in ALM and which is required for a behavioral response to gentle touch. Also, the desensitization of ALM to repeated stimuli is compared to known habituation responses, suggesting

that part but not all of habituation may arise from changes in responsiveness of the touch neurons. In addition, we demonstrate that sensory stimuli can produce calcium transients in other touch neurons and in the avoidance neuron ASH, and that electrical excitation produces global calcium transients. As such, cameleon imaging is a promising approach to investigate the neuronal activity underlying a variety of behaviors in *C. elegans*.

3.2 Introduction

The nematode worm *Caenorhabditis elegans* exhibits a simple characteristic behavior in response to being touched: it moves backwards if the touch was delivered to its anterior half, and forwards if the touch was delivered to its posterior half. Single cell laser ablation has identified the neuronal circuit responsible for mediating this behavior: five touch receptor neurons detect gentle touch and provide input to two pairs of interneurons that control forward and backward movement.

The five functional touch receptor neurons fall into four classes of mechanosensory neurons of the touch receptor type found in the adult hermaphrodite. These consist of: ALML and ALMR, a bilaterally symmetric pair of neurons with cell bodies in the lateral midbody and processes running anteriorly; AVM, a single neuron with a cell body near the ventral midbody and an anteriorly-directed process in the ventral midline; PLML and PLMR, a bilaterally symmetric pair of neurons with cell bodies near the tip of the tail and lateral processes running to the midbody; and PVM, a ventral tail neuron that sends a ventral process to the midbody. Three of these classes, excluding PVM, have been shown to mediate touch-sensitive behavior in the worm [Chalfie and Sulston 1981]; PVM is called a touch neuron on the basis of morphological similarity to the other three. All four classes have long processes surrounded by an extracellular mantle that is connected to the worm's cuticle at several attachment points. Deformation of the worm's body wall is thought to cause stresses on the mantle which are transmitted to the process of the touch receptor neuron.

The touch receptor neurons are responsible for sensing both gentle touch and tap [Driscoll and Kaplan 1997]. Gentle touch is delivered by brushing the tip of an eyelash or eyebrow hair against the body wall of the worm by hand; a tap is a nonlocalized vibrational stimulus delivered by an agar plate on which a worm has been placed. Worms usually respond to taps by backing, but occasionally respond by accelerating forward; this is thought to result from a competition between inputs from the anterior and posterior touch receptor neurons at the interneuron level. In contrast to these behaviors, response to harsh touch–prodding with a platinum wire–does not require the touch receptor neurons, although the interneurons are still needed to mediate forward and backwards motion.

Isolation of mutants defective in the gentle touch/tap mechanosensory response have enabled the identification of proteins required for a putative mechanically gated channel complex (reviewed in [Driscoll and Kaplan 1997]). These include extracellular factors, including MEC-1 which is necessary for proper formation of the extracellular mantle around the touch neuron process, and MEC-9 and MEC-5 which are thought to be secreted; intracellular factors, including the MEC-7 and MEC-12 tubulins and MEC-2 which is thought to link the cytoskeleton to the channel; and membrane factors, including the MEC-4, MEC-10, and MEC-6, proteins of the degenerin/epithelial Na^+ channel family, which are thought to form the pore of the mechanically gated channel.

Despite this wealth of knowledge about the mechanosensory response in *C. elegans*, surprisingly little is known about the response properties of the touch neurons themselves. Electrophysiology is complicated by the small size of *C. elegans* neurons and by the worm's tough cuticle. The touch neurons are a particularly difficult target for *in vivo* recording, as rupturing the cuticle will have poorly defined effects on the mechanical environment of the touch neuron processes, and delivery of mechanical stimulation may complicate the maintenance of good electrical access to the cell. Therefore, we are using the calcium indicator cameleon [Miyawaki et al. 1997] to investigate the activity of the touch neurons *in vivo*. Briefly, cameleon is a ratiometric indicator based on CFP, YFP, and calmodulin; in response to increasing calcium, cameleon partially

shifts its emission from CFP to YFP through fluorescence resonance energy transfer. This change in emission spectrum can be monitored by following the ratio of YFP to CFP emission intensity; an increase in calcium causes an increase in this ratio. Calcium transients can be reliably detected by cameleon in *C. elegans* muscles [Kerr et al. 2000].

We describe here the use of cameleon to image calcium transients in the touch neurons of *C. elegans*, and perform a preliminary characterization of the response properties of these neurons. We also show that the transients we image require MEC-4 and thus are part of the gentle touch response.

3.3 Results

3.3.1 Evoked ratio changes in *C. elegans* neurons

(Note: this section is reproduced without alteration from [Kerr et al. 2000].)

To image calcium transients in neurons, we used the strain *ljEx3*, which expresses YC2.1 under the control of the pan-neuronal *unc-119* promoter [Maduro and Pilgrim 1995]. As shown in Figure 3.1a, application of external calcium in a membrane permeabilized preparation showed that neuronally expressed cameleon was responsive to calcium (Figure 3.1b), although noise levels were increased by an order of magnitude or more due to the small size of *C. elegans* neurons. Use of a video-rate two-photon microscope [Fan et al. 1999] decreased the background fluorescence from neighboring neurons, which would dilute any signal, but did not decrease noise levels a great deal.

We next investigated whether cameleon could be used to detect voltage-dependent calcium transients in live neurons. A survey of neurons in intact worms showed occasional small ratio changes that were not immediately attributable to motion artifacts. However, since there are no independent indicators of neuronal activity in *C. elegans* that work in behaving animals, we were unable to verify that any ratio changes seen in such animals were a result of neuronal activity and not artifactual. Therefore, to verify that cameleon could detect authentic neuronal calcium transients, we used an extra-

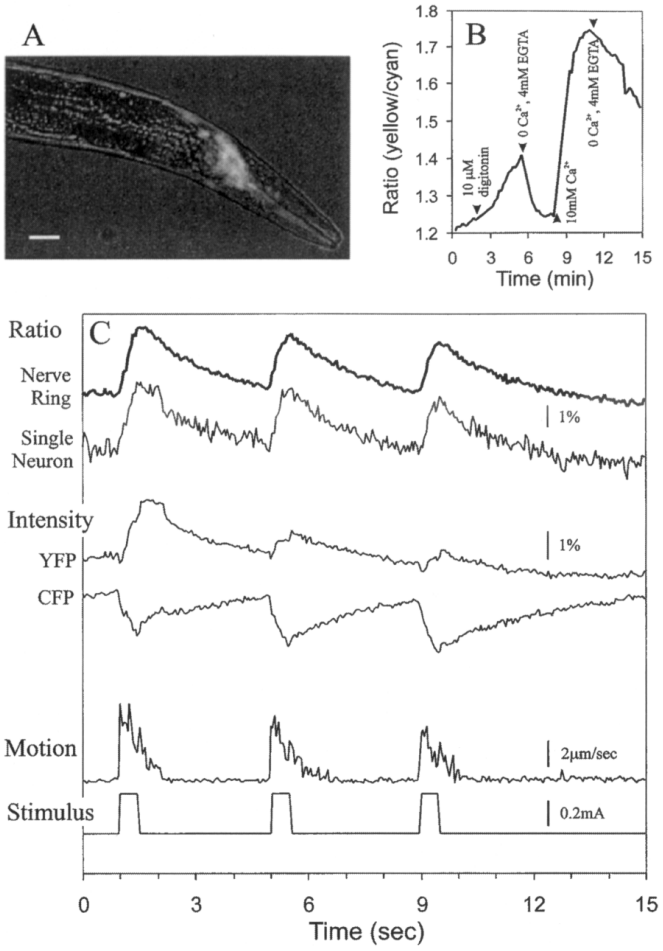

Figure 3.1: Preliminary Investigation of Neuronal Calcium Transients

(A) Expression pattern of YC2.1 under the *unc-119* promoter. Fluorescence is most noticeable in the nerve ring clustered around the pharynx in the head, though expression patterns and intensity varies from worm to worm. The image shows merged fluorescence and transmitted light. The worm's head is to the lower right. Scale bar is 20μm.

(B) Cameleon retains activity in *C. elegans* neurons. The head of a *ljEx3* worm was removed, exposed to the detergent digitonin, and switched between calcium-free (4mM EGTA) solution and 10mM calcium solution to determine the maximal response of cameleon in neurons. Although intracellular access to all neurons in the field of view may not be uniform, neuronal cameleon is clearly responsive to calcium changes. Arrowheads indicate solution changes.

(C) Response of neurons to electrical stimulation. Both the entire nerve ring (top trace) and individual neurons within the nerve ring (second trace) show transient increases in fluorescent ratio coupled to electrical stimulation (bottom trace; each stimulus consists of a train of 100 0.1ms current pulses at 200Hz). The individual wavelengths (middle two traces) show roughly opposite changes in intensity over the entire nerve ring, as expected for a change in FRET, though both traces have significantly increased noise, especially during periods of motion caused by muscle contraction (second to bottom trace). Intensities were corrected for photobleaching by removing the exponential trend before and after stimulation; without correction, the YFP channel decreased by approximately 10% during the recording.

cellular glass electrode to induce activity through electrical stimulation. The electrode was used to pierce the worm's cuticle and was positioned in close proximity to neurons in the nerve ring. Electrical stimulation produced ratio changes in ring neurons as shown in Figure 3.1c. Although activity was synchronous throughout the nerve ring, transients in individual neurons were large enough to be detectable. The electrical stimulation caused muscle contraction that created motion in the sample, causing additional noise in the individual wavelength intensities that was roughly correlated with the motion. In instances where motion of the sample made the individual wavelengths difficult to interpret, such as was the case for the single-neuron trace in Figure 3.1c, the ratio changes nonetheless appeared very similar to those cases where motion effects were minor. This indicates the value of the ratiometric nature of the indicator in a moving sample.

3.3.2 Mechanically evoked calcium transients in mechanosensory neurons

Since electrical stimulation produced calcium transients visible in single neurons, we expected that a more natural stimulus could also produce an observable response in appropriate sensory cells. We therefore used the *mec-4* promoter [Monica Driscoll, pers. comm] to drive expression of the YC2.12 version of cameleon [Nagai et al. 2002] in the mechanosensory neurons of the worm. The construct was integrated in the Driscoll lab to produce two separate stable lines *bzIs17* and *bzIs18*. A glass probe with a rounded tip approximately 15μm in diameter was connected to a miniature motorized stage and driven forwards and backwards to deliver brief (150ms) deformations of approximately 10μm depth into the body wall of *bzIs17* or *bzIs18* worms. Initially, we directed these stimuli just anterior of the cell body of the ALM touch receptor neuron (Figure 3.2a). These stimuli reliably elicited transient ratio changes in the cell body of ALM as seen in Figure 3.2c. Although the process of ALM is too small to image reliably, ratio changes in the processes appeared grossly similar in those cases where the process was sufficiently bright to allow imaging (data not shown). Longer stimulations, given by continuously moving the probe back and forth in 1μm steps while in contact with

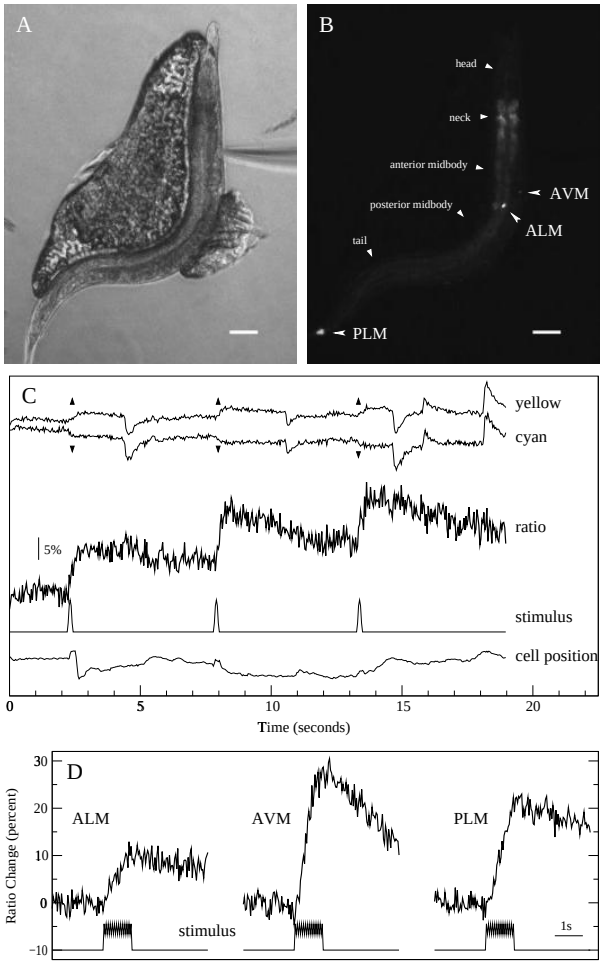

Figure 3.2: Mechanical Stimuli Induce Calcium Transients in Touch Neurons
(A) An adult hermaphrodite glued on a 2% agarose pad with the glass tip of a stimulator ready to give a mechanical stimulus. The probe is driven forward at a 45 degree angle from vertical 10 microns into the worm. Scale bar is 50 microns.
(B) Expression pattern of the integrated *mec-4*::*YC2.12* line *bzIs17*. The three functional classes of touch receptor neurons are marked. Small white triangles indicate typical targets for stimulus, as labeled. Scale bar is 50 microns.
(C) Three mechanical stimuli (4th trace), each a 150ms long poke of the probe causing a 10 micron deflection of the worm's body wall, elicited robust ratio increases (center trace) from cameleon in the ALM touch neuron. Black arrowheads indicate reciprocal change in the intensities (top two traces), as expected from a FRET-based ratiometric indicator. The large intensity artifacts are due to lamp instability. The motion of the cell (bottom trace; distance from mean position) was minimal during the stimulus and has a different profile than the ratio changes, indicating that motion artifacts are not contributing significantly to the ratio signal.
(D) Fluorescent ratios from the three functional classes of touch receptor neurons were recorded and indicate a robust calcium response (upper lines). The stimulus (lower lines) consisted of a 10 micron deflection of the worm's body followed by repeated 1 micron motions back and forth for a total duration of one second. Differences in amplitude between types are within observed variation in ALM.

the worm, caused larger calcium transients (Figure 3.3b). We call this latter stimulus a buzz and the brief stimulus a poke.

We were able to elicit responses from all three classes (Figure 3.2d), although stimulation of the pair of ALM neurons gave the most consistent response. Expression of our indicator in AVM was often weak or nonexistent, and we found it difficult to immobilize the extreme tip of the tail where the PLM cell bodies are, causing a large fraction of PLM recordings to be unusable due to focus changes. Therefore, we elected to restrict further observations to the ALM neurons.

3.3.3 Response to mechanical stimulation requires the MEC-4 putative mechanoreceptor

Withdrawal behavior in response to gentle touch or tap requires the expression of the MEC-4 protein in the mechanosensory neurons [Chalfie and Sulston 1981]. *mec-4* encodes a putative mechanoreceptor [Driscoll and Chalfie 1991] of the DEG/ENaC family [Welsh and Xie 2001] and is part of a genetically identified mechanotransduction complex expressed in the mechanosensory neurons [Driscoll and Kaplan 1997]. However, response to harsh touch relies on other unidentified molecules and does not require the MEC-4 complex, instead requiring the PVD neurons in the absence of the touch neurons [Way and Chalfie 1989]. In order to determine whether the calcium transients we observed were due to gentle touch or harsh touch receptors, we obtained *bzIs17;mec-4(u253)* worms from the Driscoll lab. In contrast to wild-type worms, these mutants showed no response to either pokes or buzzes (Figure 3.3a), suggesting that both types of stimuli correspond to gentle touch stimuli. Harsh touch is typically delivered by prodding worms by hand with a platinum wire; we gave a variety of harsher stimuli to see if we could see a harsh touch response in ALM. Large amplitude deflections failed to induce a response, as did varying the size and composition of the probe tip. However, we were able to elicit long-lasting responses in worms carrying mutant alleles of *mec-4* by using very abrupt 10μm motions of a probe with a tip made of Tygon tubing with a flat face pressed against the body wall (Figure 3.3c). Thus ALM may

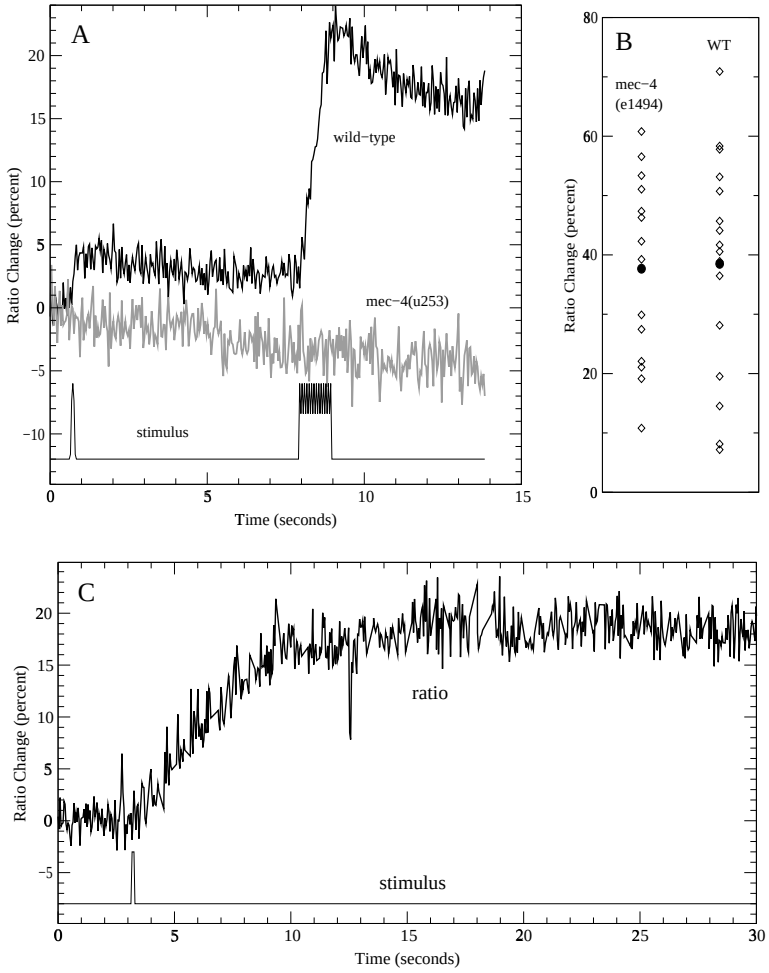

Figure 3.3: Touch neurons require *mec-4* for sensitivity to poking but not for excitability.
(A) *mec-4* is required for sensitivity to poke and buzz stimuli. Wild-type (black line) and mutants in the putative mechanoreceptor subunit *mec-4(u253)* (gray line) carrying the *bzIs18* cameleon array were individually stimulated with both 150ms poke (10 micron deflection) and 1s buzz (10 microns+1 micron agitation) stimuli (thin line).
(B) *mec-4* is not required for calcium response to potassium-induced depolarization. Cameleon-expressing neurons grown in culture from both *mec-4(e1494)* and wild-type worms were placed in a perfusion chamber and the bath solution was switched between normal and high-potassium buffer that is expected to cause approximately 100mV depolarization. Ratio changes induced in single trials (open diamonds) and the mean response (closed circles) are shown; the two populations are not significantly different.
(C) Sufficiently harsh agitation intermittently excites touch neurons in a *mec-4* background. *mec-4(u253)* worms were stimulated with an extremely abrupt 10 micron deflection using a Burleigh inchworm drive. A subset of animals had responses similar to the one shown here; the remainder were inactive.

also produce calcium transients in response to harsh touch stimuli.

Although genetic evidence and localization is consistent with DEG/ENaC channels functioning as mechanoreceptors, electrophysiological confirmation has been difficult due to the difficulty in reconstituting mechanoreceptor activity of these channels in heterologous expression systems. Thus it is possible that mutations in *mec-4* merely disrupt generic properties of the touch neurons, preventing mechanical stimulation from leading to excitation. The ability to induce a harsh touch response in some animals in a *mec-4* mutant background argues against a complete loss of cell excitability, however. To further investigate the excitability of touch neurons in a *mec-4* mutant background, we created cell cultures [Christensen et al 2002] of both wild-type and *mec-4* mutant touch neurons expressing cameleon and assayed their responses to K^+-induced depolarization. As shown in Figure 3.3b, neurons from both wild-type and mutant animals had similar calcium responses, consistent with a direct role for *mec-4* in mechanotransduction.

3.3.4 Response properties and receptive field of the ALM touch neuron

Although behavioral data has defined the importance of the touch neurons, including ALM, it is difficult to measure many of the response properties of the mechanosensory neurons with behavioral assays. The cause of the difficulty is twofold: first, given the small size of *C. elegans*, it is difficult to give localized stimuli of repeatable strength by hand; second, behavioral responses typically take hundreds of milliseconds to begin and several seconds to complete. In vertebrates, mechanoreceptive neurons have a variety of response properties [Koltzenberg et al. 1997] including subclasses with rapid or slow adaptation to constant pressure, either of which is grossly consistent with behavioral data.

To begin to characterize the response properties of the ALM mechanosensory neuron, we first gave stimuli consisting of pokes of varying displacement to determine whether there was some threshold that needed to be reached before a response could be observed. Responses were observed with displacements just sufficient for the probe

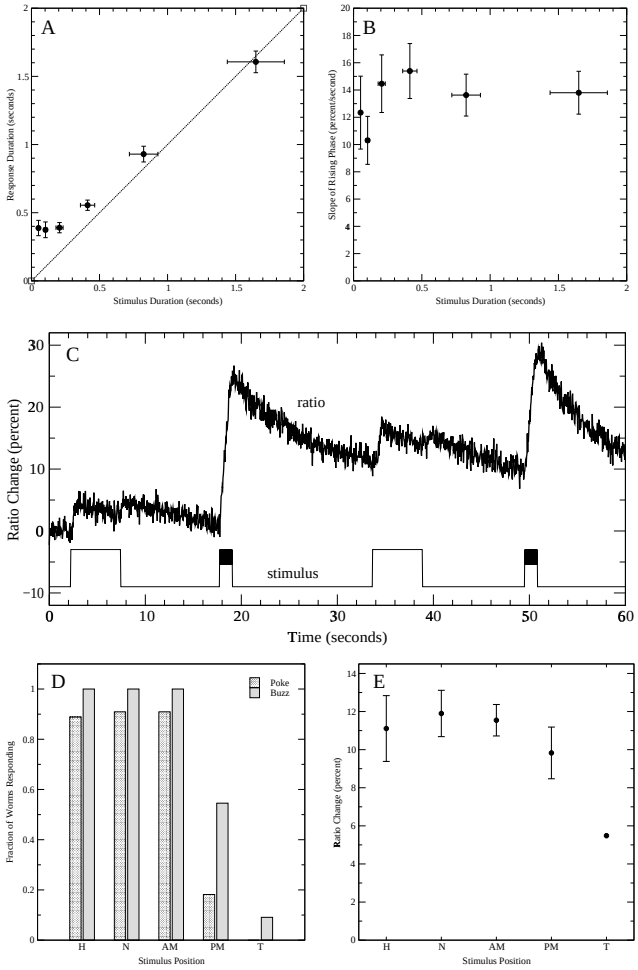

Figure 3.4: Response characteristics and receptive field of ALM.
(A) Poking elicits a calcium response with a ~400ms minimum average duration. Worms were poked with a variety of velocities and a constant 15 micron deflection. The duration of the ratio change response (black circles, mean±S.E.M.) exceeded the duration of the stimulus (dashed line) for shorter stimuli. $n = 15$ for each point.
(B) The speed of a poke does not substantially affect the rate of calcium entry. Filled circles show the slope of events (mean±S.E.M.) induced in (A); none of the classes are significantly different. We would expect a stimulus that caused greater calcium entry to show a larger rise in ratio with a higher slope.
(C) Touch neurons sense motion rather than deflection. The ratio response (thick line) to a stimulus (thin line) consisting of alternating 5s deflections of 10 microns and 1.25s deflections of 10 microns with 1 micron agitation at the forward position is shown; note that there is both an on response and off response to the static 5s deflection and a continual rise during the 1.25s agitation.
(D) Receptive field of ALM. Worms were stimulated with either a 150ms poke (dappled bars) or a 1s buzz (gray bars) at five positions along the body (see Figure 3.2b): H (head), N (neck), AM (anterior midbody), PM (posterior midbody), T (tail) and the fraction of worms responding was recorded. $n \geq 10$ for each location.
(E) Sensitivity over receptive field. Black circles indicate the amplitude of ratio changes induced by stimulation in (D) at each position (mean±S.E.M). $n > 5$ for each location save the tail, which is a single trial. None of the differences in amplitude are significant.

to touch the body wall (data not shown), to within the accuracy of our stage's motion (~1μm). Larger displacements resulted in somewhat larger responses, but since the larger displacements also lasted longer, it was difficult to tell whether the increase was due to the increased duration of the poke or the increased displacement. We therefore used a constant displacement of approximately 15μm and varied the velocity of our probe to generate pokes with a continual motion but of varying duration and speed. Even with very short (<100ms) pokes, we observed ratio increases lasting approximately 400ms on average (Figure 3.4a); long (~1600ms) pokes elicited responses that lasted for the full duration of the poke. Furthermore, as shown in Figure 3.4b, the slope of these rises was approximately constant across all poke durations (equivalently, the amplitude of the ratio response was proportional to the duration of the response). This suggests that there is some minimum duration of calcium flux (perhaps due to a long open time of the mechanosensory channels, or the triggering of secondary intracellular or extracellular calcium release) and that this minimum duration can be extended by continued mechanical stimulation. Although the relationship between total calcium entry and ratio increase is not precisely linear, comparison of the brightness of neurons expressing YC2.12 and microdroplets of purified CFP suggested that the protein concentration is in the tens of micromolar. Since this concentration is well above the K_d of the high-affinity calcium binding sites of cameleon, we expect the total ratio increase to reflect the total calcium flow into the cytosol, and therefore the slope should represent the rate of calcium influx (see section 4.3.3). The constancy of the slope suggests a fairly steady rate of calcium entry over the entire duration of the response.

Two sets of mechanosensory response properties could explain the approximately constant calcium flux during stimulations of different lengths. First, ALM could be functioning as a non-adapting pressure or deflection sensor. In this case, from the moment the probe touched the worm until the moment it left, the mechanosensory channels would be activated, inducing (perhaps indirectly) the observed calcium flux. Alternatively, ALM could be a high-sensitivity motion sensor, where the constant motion of the probe would be sufficient to induce a maximal response, but where any

specific position of the probe would be rapidly adapted to. To distinguish these two possibilities, we stimulated worms with both a 1.5s buzz stimulus and a pressing stimulus where the probe was held motionless in the forward position for 1.5s. In most cases, the press induced responses during forward and backward motion of the probe, but not while the probe was held in the forward position (Figure 3.4c). In contrast, the buzz produced a large response with nearly linear slope. Thus, ALM appears to function primarily as a high-sensitivity motion sensor rather than a deflection or pressure sensor. However, in some cases, we also observed large responses to a press stimulus, particularly (but not reliably) in cells with lower cameleon expression levels. There are several possible explanations for this observation. First, some worms may attempt to back away from the stimulus, causing the worm to move against the stationary probe and inducing a motion-detection response. Second, adaptation may be incomplete, with enough residual activity to cause a feedback-driven calcium response when cameleon levels are too low to buffer intracellular calcium; in this case, ALM would be a high-sensitivity motion detector and a low-sensitivity pressure/deflection detector. Finally, ALM may express two or more different mechanically gated channels, with the high-sensitivity *mec-4* dependent channel functioning as a motion sensor and the low-sensitivity harsh-touch channel functioning as a pressure/deflection detector. We attempted to determine whether response to the press stimulus was *mec-4* dependent by giving such stimuli to animals carrying mutations in *mec-4*, but we were unable to reliably induce a press response in wild-type, making comparisons to mutants inconclusive.

Laser ablation studies have shown that ALM is required for a full response to touch on the anterior half of the body, consistent with the morphology of the cell. To verify that the receptive field of ALM to our stimuli matched the receptive field measured behaviorally, we gave both 150ms poke and 1s buzz stimuli at varying locations along the length of the animal. We delivered stimuli in five locations: the head, past the structurally specialized part of the ALM process; the neck, just posterior of the terminal bulb of the pharynx; the anterior midbody, just anterior of the ALM cell body; the

posterior midbody, immediately posterior to the ALM cell body; and the tail (positions shown in Figure 3.2b). We observed reliable responses to a 1s buzz at the three anterior stimulus locations and almost never saw a response to tail stimulation (Figure 3.4d); responses to posterior midbody stimulation were intermediate in occurrence. Since the worm's body consists of a contiguous fluid-filled cavity, we suspect that stimulation at the posterior midbody often (and the tail, rarely) causes enough motion along the ALM process to induce a response. Interestingly, in the successful trials, the slope of transients caused by posterior midbody stimulation was not significantly less than that caused by anterior stimulation, suggesting that there is a sharp threshold for stimulation; below the threshold, no calcium flux occurs at all, while above the threshold a near-maximal flux is rapidly attained.

3.3.5 Reversible desensitization of the ALM touch neuron mechanosensory response after repeated stimulation

When worms are given repeated gentle touch or tap stimuli, their behavioral response undergoes a characteristic habituation that depends on the interstimulus interval (ISI) and the type of stimulus [Jorgensen and Rankin 1997]. Laser ablations have been used to assess the dependence of habituation on the various interneurons that receive input from the touch neurons [Wicks and Rankin 1997]. However, it is difficult to devise a behavioral assay to directly measure aspects of habituation that are dependent on the touch neurons alone. We therefore investigated whether ALM would desensitize in response to poke or buzz stimuli. We initially gave 1.5s buzzes to induce large calcium transients with a 60s ISI and observed a 50% decrease in response by the fourth stimulus, followed by gradual recovery (Figure 3.5a), indicating that the ALM response can reversibly desensitize.

To determine whether this desensitization plays a part in the habituation of the behavioral response to tap, we devised stimulation protocols analogous to standard habituation protocols. Previous studies have shown that habituation to tap occurs within 10 stimuli delivered with a 10 second interstimulus interval (ISI); habituation protocols

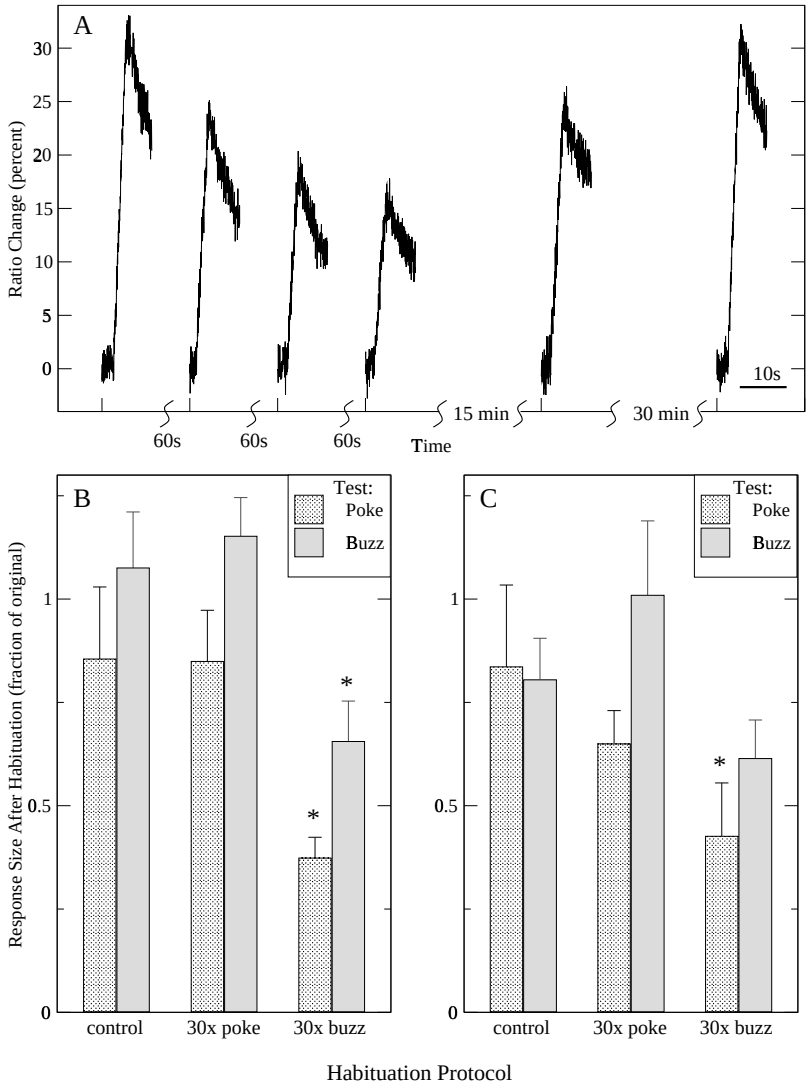

Figure 3.5: Desensitization of the mechanosensory response

(A) A single worm was stimulated six times with a 1.5s buzz at the intervals indicated and the response from ALM was recorded; after a rapid reduction in the response with a 60 second interstimulus interval, the response recovered after 15 and 30 minute rest periods.

(B) Calcium transients induced by poke and buzz stimuli were imaged both before and after a habituation protocol, and the magnitude of the responses was compared. The habituation protocol consisted of a five-minute wait (control), a 150ms 10μm poke once every 10 seconds for 5 minutes (30 pokes total), or a 1s buzz once every 10 seconds for 5 minutes (30 buzzes total). Only the buzz protocol induced desensitization of the response; responses to both pokes and buzzes were affected. The habituation stimuli and test stimuli were given at the same location at the neck of the worm. Asterisks indicate significant differences from control ($p<0.05$). n=7 for each condition; error bars are S.E.M..

(C) As in (B), but test stimuli were given at the anterior midbody, away from the direct site of mechanical stimulation. Again, the buzz protocol induced desensitization to poke and buzz test stimuli, suggesting that the mechanism of desensitization acts at the whole-cell level. Asterisks indicate significant differences from control ($p<0.05$). The decrease in the buzz test stimulus did not reach the level of significance ($p\approx0.10$), but is more consistent with the decrease seen in (B) than with being unchanged. n=7 for each condition.

typically consist of 20-40 stimuli at 10 seconds ISI. Since excessive photobleaching prevented us from recording responses during the entire habituation protocol, we elected to compare test stimuli delivered one minute before and one minute after habituation. Also, since it was unclear whether a poke (150ms stimulation) or buzz (1s stimulation) was more analogous to the stimulation a worm receives in the behavioral assay (tap delivered to the worm's plate), we used both for test stimuli and in the habituation. Both test and habituating stimuli were given at the same location. As shown in Figure 3.5b, a habituation protocol of 30 buzzes delivered with 10s ISI caused an approximately 50% decrease in the worm's response to both types of stimuli. However, 30 pokes delivered with 10s ISI caused no significant decrease in response, comparable to a control condition where the worms were left unstimulated for the same duration (Figure 3.5b). However, we observed that worms often responded behaviorally when poked before the habituation protocol, but not afterwards. This suggests that desensitization of the mechanosensory neurons is insufficient to fully explain behavioral habituation.

The reduction of the response of ALM to repeated stimulation could be either a desensitization of the entire cell or an adaptation of the mechanoreceptors or downstream signaling components at the site of stimulation. In order to distinguish these possibilities, we gave a second set of test stimuli at the anterior midbody before and after a habituation stimulus protocol delivered to the neck (see Figure 3.2b for locations). As shown in Figure 3.5c, these test stimuli showed a similar decrease. We therefore conclude that desensitization is cellular in scope and therefore is unlikely to involve the mechanoreceptors directly. However, we cannot rule out the possibility that the stimulation at the neck is mechanically transmitted along the process of ALM, causing global desensitization of the mechanoreceptors.

Since cameleon is a calcium buffer and plasticity often requires elevated calcium levels, the presence of our indicator could be disrupting normal behavioral habituation. In order to test this possibility, we observed the response to tap of both wild-type and *bzIs17* worms. On the first tap, both wild-type and *bzIs17* worms gave robust backwards responses; after repeated stimulation, both wild-type and *bzIs17* worms

habituated, indicating that habituation was not severely disrupted by cameleon (data not shown). In fact, surprisingly, *bzIs17* appeared to habituate more rapidly than wild-type.

3.3.6 The polymodal avoidance sensory neuron ASH shows calcium transients in response to chemical but not mechanical stimuli

The touch neurons are not the only mechanosensory cells in *C. elegans*. Nose touch causes retraction of the nose and backing and does not require the anterior touch neurons; instead, it requires ASH, FLP, and OLQ, with ASH responsible for approximately 50% of responses [Kaplan and Horvitz 1993]. We therefore expressed YC2.12 under control of the *sra-6* promoter to drive expression in ASH [Troemel et al. 1995] and attempted to observe calcium transients in response to mechanical stimulation. However, we were unable to produce any detectable calcium transients with mechanical

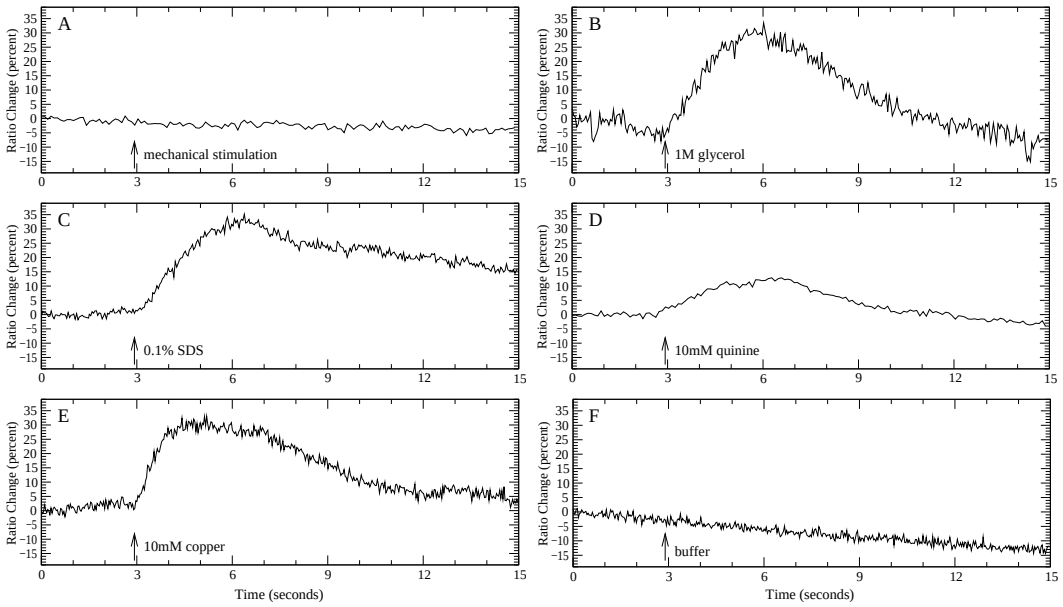

Figure 3.6: Application of noxious stimuli to ASH.
(A)-(F) ASH gives calcium transients in response to soluble repellents. In each case, a single worm was placed in a perfusion chamber with a constant flow of neutral buffer. In (A), a piece of glass was pressed against the worm's nose. In (B)-(E), the worm was exposed to a repellent for 3s (starting at arrow). In (F), a control solution containing no repellent was used in place of the repellent.

stimulation (Figure 3.6a).

ASH also detects various noxious soluble chemical stimuli including high osmolarity [Bargmann et al. 1990], detergents [Hilliard et al. 2002a], alkaloids [Hilliard et al. 2002b], and heavy metals [Sambongi et al. 1999]; the behavioral response to these stimuli is also backing. To test these stimuli we placed worms in a perfusion chamber with a constant flow of neutral buffer. We continuously delivered soluble repellents in solution through a micropipette. To apply the repellent to the worm, we positioned the tip of the pipette next to the worm's head. To remove the stimulus, the micropipette was moved 1mm downstream from the worm's head. As shown in Figures 3.6b-e, ASH was responsive to 1M glycerol (high osmolarity), 0.1% SDS (detergent), 10mM quinine (alkaloid) and 10mM Cu^{2+} (heavy metal). The concentrations used all give a robust behavioral response when delivered to worms on plates. Control delivery of neutral buffer produced no response (Figure 3.6f). Thus we concluded that ASH produces a calcium response when presented with soluble repellents, but may not in response to mechanical stimuli. Perhaps this reflects the different signaling mechanisms used for each substance, as determined by the observation that habituation to nose touch does not affect detection of noxious substances and vice versa [Hart et al. 1999]. Alternatively, it is possible that we were simply unable to deliver a suitable mechanical stimulus for ASH, although we did often observe a reaction to a probe hitting the worm's nose. Since the experiments were performed on wild-type worms, we can't rule out that this behavioral response was mediated by the anterior touch neurons, FLP, or OLQ, and that ASH was never appropriately stimulated mechanically.

3.4 Discussion

3.4.1 Sensory neuron activity in *C. elegans* can be monitored with cameleon

We have demonstrated that stimulus-invoked activity in the touch neurons of *C. elegans* can be reliably and quantitatively monitored with the cameleon indicator. In ad-

dition, we showed that chemical stimulation of ASH and electrical stimulation of the entire nerve ring also produced detectable activity. Many sensory cells have been identified in the worm, including those involved in chemotaxis, thermotaxis, chemoavoidance, and sensitivity to dauer pheromone [Bargmann and Mori 1997]. Our results suggest that many of these cells may also be amenable to analysis with cameleon, potentially allowing a more precise characterization of cellular properties, and defects caused by mutations, than is currently possible with behavioral analysis. In addition, there are a variety of neurons with a morphology that appears sensory, but for which no sensory function has been identified; this is especially true in male animals [Bargmann and Mori 1997] and the phasmids of the hermaphrodite tail. Measurement of the activity of these cells using cameleon may provide insight into what compounds or other stimuli these neurons are responsive to. This would be particularly useful in cases where the behavioral effect is too subtle to be easily identified. In addition, with appropriate promoters, multiple neurons could be tested in a single worm; this is likely to be less time-consuming than laser ablation of every sensory neuron, especially in the male where there are many uncharacterized sensory neurons.

Despite our success with both touch neurons and ASH, cameleon recording is not entirely straightforward. A number of factors proved essential for reliable recording. First, it was not enough to simply obtain expression of cameleon in a neuron of interest. We tried a number of promoters to drive expression in ASH, and although expression was detectable, expression levels were too low for reliable imaging. An *osm-10::YC2.1* construct containing the full coding sequence of *osm-10* fused to the N-terminal of YC2.1 was sufficiently bright, but failed to give any activity in ASH. Transgenic worms with the *osm-10::YC2.1* construct had defective chemoavoidance behavior, suggesting that the function of ASH was disrupted, possibly because of the overexpression of OSM-10. Thus, an appropriate construct is critical for obtaining observable activity. Unfortunately, in cases where a behavioral response is unknown, it may be difficult to assess whether a given construct is functional or is disrupting the cell of interest.

The second factor that greatly aided the success of our recordings was the ability to

give precisely delivered and timed stimuli with motorized micropositioning devices. Previous attempts to deliver mechanical stimuli using a manual micromanipulator or the motion of an off-the-shelf speaker gave intermittent results. (Another standard technique of applying constant force using von Frey hairs was unavailable to us given the small size of our experimental organism.) Similarly, applying repellents to ASH by switching the bath solution gave broad and poorly-timed transients, in contrast to the relatively sharp responses evoked by local perfusion from a micropipette. The third important factor was the availability of suitable analysis tools. Even with worms glued for imaging, the neuronal cell bodies frequently moved several microns. Since the cell bodies are only several microns in diameter themselves, methods for automatic tracking of regions of interest were of great value in recovering usable data from a majority of experiments. In addition, tools that allowed rapid display and analysis of the results of an experiment allowed us to adjust conditions with minimal delay; although this was less critical when experimental conditions had been finalized, it was of great value for debugging and pilot experiments. As mentioned previously [Kerr et al. 2000], simultaneous imaging of both CFP and YFP channels of cameleon was also essential for obtaining usable data.

Given the positive results from electrical stimulation, ASH, and the touch neurons, we have no reason to suspect that this technique will not also work on non-sensory neurons, given appropriate promoters and recording conditions. It may be difficult to detect spontaneous activity of unknown frequency due to the photobleaching of the indicator. However, we anticipate that recordings of interneuron activity in response to various stimuli are likely to be successful under essentially the same conditions that we have used here.

3.4.2 Receptive properties of the *C. elegans* touch neurons

Although a wide variety of vertebrate mechanosensory cells have been identified in the skin [Munger and Ide 1988], none of them are obviously homologous to the *C. elegans* touch neurons. Vertebrate studies have identified a variety of response

classes [Koltzenberg et al. 1997], including rapidly adapting (RA), slowly adapting (SA), D-hair (DH), and high-threshold mechanosensitive nociceptive A (AM) fibers. Our results indicate that the *C. elegans* response is similar to the rapidly adapting response, which has a characteristic strong on response and weaker off response [Koltzenberg et al. 1997]. Specifically, a response is observed for the entire duration of a moving stimulus, but only on and off responses are observed when a constant deflection is applied. Further, the response appears to be all-or-none; stimuli given at different speeds and at different positions along the body produced responses of similar slope, even when the stimulus had a high failure rate. This type of sharp threshold response is also seen in RA fibers, in contrast to the more graded responses seen in SA and AM fibers. Thus, in terms of response properties, the *C. elegans* touch neurons appear grossly similar to the RA class of mechanoreceptor neurons. Interestingly, the RA mechanoreceptor neurons are thought to mediate the response to gentle touch in vertebrates, and members of the DEG/ENaC family of putative mechanoreceptor proteins have been found localized to sensory endings in these neurons [Price et al. 2000]. Although there are obvious differences between the *C. elegans* touch neurons and vertebrate RA mechanoreceptor neurons–for instance, the structural specializations around the sensory endings are different, and *C. elegans* neurons are not thought to have sodium-driven action potentials–our results reinforce the similarity between *C. elegans* and vertebrate low-threshold touch receptors.

The *Drosophila* bristle mechanosensory neuron also shows rapid adaptation and a fairly sharp threshold for activation, although it requires a novel non-DEC/ENaC mechanotransduction channel [Walker et al. 2000]. However, unlike the *Drosophila* electrical response which lasted tens of milliseconds, we observed a minimal calcium response of approximately 400ms duration in *C. elegans*. There are a number of possible explanations for this observation. One is simply that the calcium transient lasts longer than the depolarization of the cell, possibly because of release of calcium from intracellular stores. Another possibility is that although the stimulus is delivered for only a very brief time, the worm takes a while to relax to its original position after be-

ing compressed by the stimulus, and this relaxation of the worm's body stimulates the mechanoreceptors. If this is the case, we would expect small deflections to relax more readily and thus produce shorter responses than large deflections, all else being equal. Finally, the observation could reflect a real difference in the duration of activation of the neuron. In this case, the 400ms transient could reflect the minimum duration of a calcium-mediated active current. Consistent with the presence of some active current, stimulation to the head and neck, far from the ALM cell body, gave responses similar in magnitude to those near the cell body; however, our results cannot distinguish between a lengthy active calcium current and a rapid current followed by continued release of calcium from intracellular stores.

3.4.3 Contribution of sensory neuron desensitization to touch habituation

Behavioral habituation to 30 taps with 10s ISI is nearly complete, with no recovery after 30s and recovery to about 60% of the initial response within 10 minutes [Rankin and Broster 1992]. In contrast, we observe a desensitization in the calcium response of only about 50% after 30 buzzes with 10s ISI. The simplest interpretation of this result is that desensitization of the touch neurons is only partially responsible for the observed habituation of the behavioral response to tap. However, due to the differences in experimental conditions, a number of other possibilities must be considered. One possibility is simply that the behavioral response is only triggered when events in the touch receptor cell are larger than a certain threshold. If that threshold is above 50% of the initial response, the desensitization would bring the response below threshold and give no behavioral response, as is observed in habituation. Alternatively, the buzz stimuli may not be a good analog of the tap stimuli. Although it is difficult to envision a tap on a plate causing it to vibrate for longer than the one second buzz stimuli, the delocalized tap presumably provides a stimulus along the entire length of the touch neuron process, and may causing more rapid desensitization. Unfortunately, observing behavior requires a worm which is largely free, while microscopy and delivery of poke and buzz stimuli requires a worm which is stationary, so it is difficult to perform

a behavioral assay during imaging. Also, since it is not practical to image from worms glued to agarose plates while the plates are being tapped, it is not feasible to mimic the stimulus used for the behavioral assay during calcium imaging. A direct approach to determining the role of touch neuron desensitization in behavioral habituation is therefore difficult.

The gentle touch / tap withdrawal circuit has been defined by laser ablation of single neurons (see [Driscoll and Kaplan 1997] for an overview). Of note, the touch receptor neurons, along with other sensory neurons that signal for avoidance behavior, synapse onto two pairs of interneurons which control forward (AVB and PVC) and backing (AVA and AVD) movement (a portion of the proposed locomotion pattern generator). A number of promoters are known which drive expression in these cells, including the promoter for the glutamate receptor *glr-1* [Hart et al. 1995, Maricq et al. 1995]. Since this receptor (presumably excitatory) is required for normal mechanosensation, and the touch neurons also form gap junctions (almost certainly excitatory) with the interneurons that signal for movement in the opposite direction, we expect mechanical stimulation to activate these neurons. We therefore expect that mechanical stimulation will produce calcium transients in these interneurons. By examining the changing coupling between mechanical stimulation and interneuron response, we should be able to detect plasticity between the touch neurons and these interneurons. If there is habituation that is not simply a result of desensitization of the touch neuron, it is likely to be a property of plasticity of the touch neuron-interneuron coupling, since multiple sensory neurons connect to these interneurons and tap habituation is independent of habituation to other avoidance stimuli [Wicks and Rankin 1997]. Thus, the cellular localization of behavioral habituation to tap should be revealed with cameleon imaging of the locomotion pattern generator in addition to the touch neurons, assuming that the pattern generator neurons generate calcium transients when they are active.

Our preliminary observation that behavioral habituation appears more rapid in cameleon-containing worms than wild-type worms complicates matters somewhat.

Since *bzIs17* worms have grossly normal mechanosensory responses, and since they still undergo habituation, it is likely that qualitative results on the localization of habituation will remain valid. However, the mechanism of more rapid habituation in *bzIs17* worms has implications for the nature of behavioral habituation. One explanation of the result is that cameleon inhibits the activity of the touch neurons somewhat, and less habituation is required before this weak stimulation produces a behavioral response. Alternatively, if intracellular calcium is required for desensitization of the touch neurons, cameleon's buffering effect could prevent desensitization of the touch neurons, causing a larger stimulation of the pattern generator neurons and inducing a stronger depression in the touch neuron-pattern generator neuron coupling. These two situations could be distinguished by recording from the pattern generator neurons in worms with or without cameleon in the touch neurons. In addition to explaining the cameleon phenotype, these experiments could also help uncover the properties of any plasticity.

3.4.4 Prospects for genetic dissection of the *C. elegans* gentle touch mechanoreceptor

A wide variety of genes that are necessary for touch receptor function have been identified through genetic screens (see [Driscoll and Kaplan 1997] for an overview). We have shown that mutants in *mec-4*, a degenerin channel thought to form part of the pore of the gentle touch mechanoreceptor complex, fail to produce calcium transients in response to our poke and buzz stimulus protocols. While this is unsurprising, it indicates that the responses we observe require the putative *mec-4* mechanoreceptor complex. We expect other *mec* mutants to fall into three classes. First, defects that abolish the activity of the mechanoreceptor complex should show no calcium transient response to normal stimulation. Second, defects that act downstream of calcium transients should produce an essentially normal calcium response. Third, some mutations may produce specific defects in the observed responses, allowing us to infer the function of specific gene products or specific residues within a given gene. For example, we

predict that mutations that decrease the effectiveness of the mechanical coupling of the receptor will show an increased failure rate, but little change in response magnitude with successful trials, analogous to our results for posterior midbody stimulation in Figure 3.4D. We therefore expect analysis of the various *mec* genes to yield additional insight into the function of the mechanoreceptor complex.

In addition, combining genetic analysis with calcium imaging provides a way to investigate the mechanism of signaling downstream of the mechanoreceptor complex. For instance, mutations have been isolated in L-type (*egl-19*), non-L-type (*unc-2*), and T-type (*cca-1*) voltage gated calcium channels, each of which is expressed in multiple neurons. Using behavioral assays alone, it is difficult to determine which, if any of these, is required for activation of the touch neurons; mutations in these genes may also disrupt downstream neurons, preventing a behavioral response to touch even when the touch neuron functions normally. With calcium imaging, we can directly assess the effect of these mutations on the touch neuron's calcium response. Also, mutations in the ryanodine (*unc-68*) and IP3 receptors (*itr-1*) should provide insight into the contribution of calcium release from intracellular stores to the observed transients.

3.5 Experimental Procedures

3.5.1 Construction of cameleon expression plasmids and integrated lines

Construction of *mec-4*::YC2.12 and *sra-6*::YC2.12 plasmids, and expression of those plasmids from lines containing extrachromosomal arrays, was performed by Hiroshi Suzuki using methods and reagents similar to those described in sections 2.5.1 and 2.5.2; the coinjection marker was *lin-15*. The *mec-4*::YC2.12 line was integrated by Dan Sloan in the Monica Driscoll lab to generate integrated lines *bzIs17* and *bzIs18*, using standard methods ([Mello and Fire 1995, p. 467]). Mutant lines expressing cameleon were constructed by Dan Sloan in the Driscoll lab by crossing lines carrying *bzIs17* or *bzIs18* with mutant lines using standard techniques.

3.5.2 Optical recordings

Optical recordings were performed on a Zeiss Axioskop 2 upright compound microscope fitted with a Hamamatsu Orca ER II CCD camera, a Hamamatsu W-View emission image splitter, and a Uniblitz Shutter (Vincent Associates), save for electrical stimulations which were observed using the equipment described in section 2.5.3. Recordings were taken on a 1200MHz Athlon (Advanced Micro Devices) computer running MetaVue 4.6 (Universal Imaging) under Windows 98 (Microsoft). Samples were typically taken at 25Hz (40ms exposure time) with 4x4 or 8x8 binning, using a 63x Zeiss Achroplan water immersion objective. Filter/dichroic pairs were: excitation, 420/40; excitation dichroic 455; CFP emission, 480/30; emission dichroic 505; YFP emission, 535/30 (Chroma).

3.5.3 Electrical stimulation of *C. elegans* neurons

(Note: this section is reproduced from [Kerr et al. 2000] without alteration, save for fixing references.)

Worms were glued to 2% agarose pads, without serotonin, as described in section 2.5.5. It was necessary to apply glue more liberally in order to immobilize the worm sufficiently. The worm and pad were then immersed in Dent's saline [Avery et al. 1995]. A standard silver-chloride glass electrode, pulled to a tip diameter of ~0.5μm, was used to puncture the worm's cuticle on the side of the head; the tip was then located near the center of the nerve ring but not embedded in the pharyngeal muscle. 0.3mA of current was applied through an Isoflex isolation unit (AMPI) driven by a Master 8 multichannel pulse generator (AMPI). Fluorescent recordings were made as described previously. The bleaching rate for the YFP component of the signal was approximately 10% over a 20s recording. Since the changes were only a few percent, this bleaching made visualization difficult, although it did not affect the ability to detect transients. We therefore removed the exponential trend as measured by fitting a single exponential to the pre-stimulus and post-stimulus portions of the trace. The CFP

component was not affected significantly by bleaching, but FRET was reduced somewhat due to YFP bleaching, causing a slight upward trend which we removed for ease of visualization using the same method.

3.5.4 Mechanical stimulation

Worms were glued as described above, except that the 2% agarose pads were made with extracellular saline (see section 3.5.6), and the worms were immersed in this saline during recording. Glued worms seemed slightly happier in extracellular saline than in Dent's solution, possibly due to a better osmotic balance.

For most of the experiments presented here, a M-111.1DG microtranslation stage (Polytec PI) mounted at a $45°$ angle on a three-axis micromanipulator (built from Newport 422-1S translation stages) was used to drive a probe against the side of a glued worm. The tip of the probe consisted of a pulled glass microcapillary needle that had its tip briefly flamed in a bunsen burner to produce a rounded tip approximately 15μm in diameter. This tip was placed against the worm's cuticle using the micromanipulator in the desired position of contact, usually so that the direction of motion was directly into the worm (making contact 70% of the way towards the edge of the body from the midline, as viewed from above). The stage was then retracted by 14μm to avoid accidental stimulation of the worm from vibration. A poke stimulus was delivered by driving the stage forwards 22μm and then immediately returning to the original position, causing a deflection of at least 8μm and on average typically 10μm (i.e. the initial positioning with the micromanipulator caused ~2μm deflection). This motion was typically made with an acceleration of 3.5mm/s^2, giving a total travel time of 320ms, a contact time of 140ms, and a maximum velocity at the point of contact of 250μm/s. A buzz stimulus was given similarly, except that the probe was kept in the forward position and then moved forwards and backwards in 1μm steps, taking approximately 70ms per cycle (a 14Hz buzz). A typical buzz gives 1s of total stimulation (12 cycles plus contact time). A press stimulus was also given similarly, except that the probe was held in the forward position for a length of time.

The positive responses from *mec-4* mutants were observed using an inchworm drive (Burleigh). The protocol was similar, but there were several differences. First, the tip of the probe was made from a sliver of Tygon tubing cut to a flat surface approximately 25μm across, using a razor blade. The probe was placed in contact with the worm during the entire recording and the stimulus was given as a forward and backward motion of 10μm. The inchworm drive has extremely rapid acceleration and was driven at approximately constant 1mm/s velocity.

3.5.5 Chemoavoidance stimulation

Worms were glued to a 2% agarose pad made with neuronal bath and placed in a perfusion chamber (Warner Instrument Corp. RC-26GLP) with a gravity-fed 5mL/min flow of neuronal bath. Chemical stimulants were added to neuronal bath and gravity-fed into a microinjection needle with ~30μm diameter opening. A motorized stage was used to move the injection needle from a holding position 1mm downstream of the worm's head to immediately adjacent to the worm's head for stimulation of a certain duration, and then back again.

3.5.6 Potassium depolarization in cell culture

Primary cell cultures from wild-type and *mec-4(e1494)* worms expressing cameleon in the touch neurons from the *bzIs17* array were prepared from synchronized worms as described in [Christensen et al 2002]. Coverslips with adherent 2-4 day old cells were placed in the perfusion chamber and attached to the bottom of the well with vacuum grease. Cells were perfused with an extracellular saline solution (145 mM NaCl, 5 mM KCl, 2 mM CaCl2, 1 mM MgCl2, 10 mM HEPES, 10 mM d-Glucose, pH 7.2 and brought to 340 mOsm with sucrose) to remove culture medium and non-adherent cells. Prior to recording, the cells were perfused with extracellular solution for 5 s to stabilize the solution level in the recording chamber. The recording protocol consisted of a 3-5 s extracellular saline perfusion, 3 s potassium depolarization (extracellular saline solu-

tion with 110mM KCl and 40mM NaCl), and 7-9 s extracellular saline. The solutions were delivered with a gravity feed perfusion system, with 6 solution tubes reaching a manifold (Warner Instruments) and one tube entering the recording chamber with a flowrate of approximately 0.5 mL/s.

3.5.7 Extraction of ratios from samples of interest in image stacks

MetaVue (Universal Imaging) was used to acquire image stacks and save them to disk. A custom Java-based program with a graphical user interface was then used to define regions of interest, and automatically track them and report the YFP and CFP intensities inside the region, as described in section 4.4. Ratios were plotted for inspection using MATLAB R12 (The MathWorks).

Correction parameters for crosstalk were measured to be: YFP emission crosstalk $C_a/D_a = 0.01$, CFP emission crosstalk $C_d/D_d = 0.60$, and YFP excitation crosstalk $A = 0.13$ (see section 4.2.3). Given the small size of the other factors, and difficulty in measuring the total quantum efficiency ratio ζ (necessary to correct for A) we only applied the correction for C_d/D_d.

We attempted to estimate ζ from reciprocal intensity changes, but artifacts in the intensity traces caused enormous variability, giving $\zeta \approx 1.96 \pm 0.19$ (mean $\pm$ SEM). We also reasoned that if artifacts caused intensity to be a factor a times the original, then a ratio change would give $I_{y2} = a\,(I_{y1} + \Delta I)$, $I_{c2} = a\,(I_{c1} - \Delta I/\zeta)$. Solving this for a in terms of ζ (with ΔI canceling), and assuming that on average $a = 1$ (i.e. on average artifacts are uncorrelated with ratio changes) gave $\zeta \approx 1.85$ with no error estimate.

3.5.8 Detection and quantification of ratio change events

Ratio changes were detected and parameterized as described in sections 4.5.2 and 4.5.3, using in most cases a detection blur of width σ = 4 frames, minimum slope and duration for detection = 2.5%/sec for at least 4 frames, measurement blur of width 1.5 frames. Detection was verified by eye; when an event was failed to be detected, the

parameters were modified slightly until good detection was achieved. In order to avoid skewing the parameters, the blur width was not altered. The routines were implemented as function files for GNU Octave, an open-source clone of MATLAB. The routines were tested with these parameters on sample (fake) data with a S/N ratios between 4 and 20 (typical of our data) and was found to have a systematic error at a given S/N ratio of less than one frame (40ms) in duration and less than 0.003 in amplitude of ratio change (0.3% ratio change).

3.6 Acknowledgements

All constructs used were designed and constructed by Hiroshi Suzuki in the Schafer lab. Strains used were constructed by Hiroshi Suzuki or in the Driscoll Lab by Dan Sloan. Development of initial mechanical stimulation protocols was conducted jointly with Hiroshi Suzuki, as was the initial investigation of touch neuron desensitization. Harsh touch stimulation of *mec-4* mutants was performed by Hiroshi Suzuki. Cell culture experiments were performed by Christian Frokjaer-Jensen in the Schafer Lab. Protocols for chemical stimulation of ASH were developed jointly with Massimo Hilliard in the Schafer Lab; recordings of chemical stimulation were performed by Massimo Hilliard.

We would also like to thank members of the Schafer and Tsien labs for valuable discussions; the Miaywaki lab for providing us with their improved YC2.12 cameleon; and Serge Lamont in the Lockery lab for advice on delivering chemical stimuli.

The text of sections 3.3.1 and 3.5.3 are a reprint of the material as it appears in Neuron in the article " Optical imaging of calcium transients in neurons and pharyngeal muscle of C. elegans." Neuron *26*, 583-594 by Kerr, R., Lev-Ram, V., Baird, G., Vincent, P., Tsien, R.Y., Schafer, W.R. (2000). The material has been reformatted to fix references and fit this format. The dissertation author was the primary researcher and author and the co-authors listed above contributed advice and technical expertise and in part directed and supervised the research which forms the basis for these sections.

Chapter 4

Technical Aspects of In Vivo Ratiometric Calcium Imaging

4.1 Introduction

The basic concept of calcium imaging is relatively straightforward: calcium enters into a cell and binds to an indicator molecule causing a change in the optical properties of that cell–in this case, the spectrum of its fluorescence. However, there are a number of complicating factors that can interfere with attempts to make reliable quantitative measurements of calcium levels or even of calcium changes. In order to develop a detailed understanding of these factors, and in some cases craft corrections, we consider four different aspects of in vivo calcium imaging with cameleon.

First, we examine the process of using fluorescence microscopy to measuring intramolecular FRET changes via changes in emission intensity. The utility of FRET has been understood for some time [Lakowicz 1983], but recent reports in the literature [Gordon et al. 1998, Xia and Liu 2001] are not entirely appropriate for our situation of intramolecular FRET where the donor and acceptor are at equal concentration and paired, and are not focused on the measurement of FRET changes. Second, we examine artifacts specific to calcium imaging and use of a protein indicator, such as calcium buffering and protein degradation. Third, since the data that we collect differs

somewhat from that of standard microscopy–our samples may move, and ratio images require precise alignment of the two measured channels–we discuss methods for obtaining reliable intensity ratios from image stacks. Finally, we discuss algorithms for analyzing the intensity ratios to identify calcium transients and extract parameters that describe those transients. For convenience, a table of frequently used variables is provided at the end of section 4.2.

4.2 FRET Ratiometric Imaging Theory

Fluorescence Resonance Energy Transfer (FRET) is a process whereby an excited donor fluorophore will transfer its energy to a nearby acceptor fluorophore with much higher efficiency than would be expected for emission of a photon by the donor and recapture by the acceptor. This process involves dipole-dipole coupling and is highly dependent on the distance and orientation between the donor and acceptor [Forster 1948, Lakowicz 1983]. The scale of distance involved is a few nanometers, making FRET an ideal candidate for examining conformational changes of single proteins and physical interactions between proteins. Indicators based on FRET changes between a fluorescent donor and acceptor are particularly useful when imaging living, behaving samples: movement caused by behavior can easily affect the intensity of light incident on the sample and the amount of emitted light detected, but these intensity changes affect both donor and acceptor equally. If we measure the ratio of acceptor to donor emission, artifacts proportional to intensity cancel out. In the following sections we briefly review the photophysics of FRET relevant to emission ratiometric imaging, and develop mathematical methods to measure the output of ratiometric indicators in a way that will allow quantitative comparison of results under a variety of conditions (such as with different filters, bleaching, and so on).

4.2.1 Kinetic model of fluorescence imaging with FRET

An isolated ground-state fluorophore in excitation light of intensity I (photons/cm^2·sec) will transition to an excited state with a rate constant of $k_e = \sigma I$ where σ is the optical cross section (cm^2) and depends on the spectrum of the excitation light (see, for example, [Tsien and Waggoner 1995]). The excited fluorophore will decay with first-order kinetics either radiatively with a rate constant of k_r or nonradiatively with a rate constant of k_n (for our purposes, we include all nonfluorescent decay modes in k_n, including intersystem crossing). Thus, following the approach used in [Sandison et al. 1995], in steady-state we have

$$N_1 (k_r + k_n) = N_0 k_e$$

where N_1 and N_0 are the number of fluorophores in the ground and excited states, respectively. The total rate of photon emission is $N_1 k_r$; each fluorophore therefore emits photons at a rate of

$$i = \frac{N_1 k_r}{N_1 + N_0} = \frac{k_r}{k_r + k_n} \frac{N_0 k_e}{N_1 + N_0} = Q \sigma I \frac{N_0}{N_1 + N_0}$$

where $Q = k_r / (k_r + k_n)$ is the emission quantum efficiency of the fluorophore. Typically, wide-field fluorescence microscopy occurs in the realm where $k_e \ll k_r + k_n$ and therefore $N_0/(N_1 + N_0) \approx 1$; this condition can be checked by varying the intensity J of the excitation light and making sure that i varies linearly. For the remainder of this section we will assume that this condition holds and therefore the per-molecule emission intensity is simply

$$i = Q \sigma I \tag{4.1}$$

with units of photons/molecules·sec.

To achieve fluorescence resonance energy transfer, we need a both donor fluorophore, which is excited directly, and an acceptor fluorophore, which is excited through energy transfer. From here on, we will denote quantities pertaining to the donor with a subscript d and to the acceptor with a subscript a.

The rate of energy transfer, k_t, depends on both the distance between and the relative angle between the fluorophores [Lakowicz 1983]; for our purposes it is sufficient

to know that for our FRET-based indicators, k_t is of the same order of magnitude as $k_r + k_n$ and varies depending on the state of the indicator. Our donor leaves the excited state with a rate of $k_{dr} + k_{dn} + k_{dt}$. Although it is possible to directly observe the difference in relaxation rate between $k_{dr} + k_{dn}$ and $k_{dr} + k_{dn} + k_{dt}$ by monitoring fluorescence lifetimes, specialized equipment is needed. However, we can observe energy transfer by looking directly at emission intensities. Let us define the FRET efficiency $f = k_{dt}/\left(k_{dr} + k_{dn} + k_{dt}\right)$ Now the donor will emit a photon

$$\frac{k_{dr}}{k_{dr} + k_{dn} + k_{dt}} = (1 - f)Q_d$$

of the time when excited; the acceptor will receive the energy and then emit a photon

$$\frac{k_{dt}}{k_{dr} + k_{dn} + k_{dt}} \cdot \frac{k_{ar}}{k_{ar} + k_{an}} = fQ_a$$

of the time; and the energy will be lost to non-fluorescence relaxation the remainder of the time. The donor will still be excited at a rate $k_{de} = \sigma_d I$. Thus, as in (4.1) we have

$$i_d = (1 - f)\, Q_d \sigma_d I \tag{4.2}$$

$$i_a = fQ_a \sigma_d I \tag{4.3}$$

Of course, we cannot measure i directly. Not all the emitted light can be collected, and not all collected light will activate our detector. We therefore define D_d and D_a, the quantum efficiency of detection of light emitted by the donor and by the acceptor. If we excite N donor-acceptor pairs, we measure emission intensities

$$\begin{aligned} I_d &= N D_d i_d \\ I_a &= N D_a i_a \end{aligned} \tag{4.4}$$

Note that the quantum efficiency of detection is affected by the microscope optics, filter sets, CCD camera (or other detector) sensitivity, and so on.

For fluorescence imaging, the fluorescence intensity emission ratio $R = I_a/I_d$ is a more natural measure of FRET than FRET efficiency, as it is easy to calculate from

the measured quantities and does not require one to know detection efficiencies. The FRET efficiency and emission ratio are related by

$$R = \frac{I_a}{I_d} = \zeta \frac{f}{1-f} \tag{4.5}$$

where $\zeta = Q_a D_a / Q_d D_d$ is the total quantum efficiency ratio. Although R is convenient to measure, it does not reflect the underlying physical processes as directly as f does. We therefore use FRET efficiency as the starting point for subsequent analysis and then relate the FRET efficiency to the emission ratio.

In the case of cameleon, we are interested in the change in FRET efficiency caused by the binding of calcium. If the mean FRET efficiency changes by a small amount $\Delta f \ll f$, either because of a small conformational change causing a small change in k_t, or because of a small fraction of molecules undergo a large change in k_t, we find that the photon emission ratio changes by

$$\Delta R = \zeta \left(\frac{f + \Delta f}{1 - f - \Delta f} - \frac{f}{1-f} \right) \approx R \frac{\Delta f}{f\,(1-f)} \tag{4.6}$$

Direct measurement will yield ΔR and R, which in general will depend on the filter set, camera, and so on. However, note that the fractional ratio change $\Delta R / R$ depends only on the FRET intensity, not details of the imaging setup. Note also that

$$\frac{\Delta I_a}{\Delta I_d} = -\zeta \tag{4.7}$$

which gives us a means to directly measure ζ. We can then, if desired, use (4.5) to determine the total FRET efficiency.

4.2.2 Photobleaching compensation

Some of the modes of decay of an excited-state fluorophore leave the molecule in a long-term inactive state; these modes are collectively called photobleaching. When using a pair of fluorophores for FRET, bleaching of the donor reduces the total intensity of both the donor and acceptor, as pairs with a bleached donor do not fluoresce at either wavelength. However, bleaching of the acceptor creates a more complex situation.

Consider a situation where a fraction α of the acceptors are unbleached and a fraction β of the donors are unbleached. We will denote the measurements affected by bleaching with a prime; the bleached emission intensities are I_d' and I_a' and the bleached emission ratio is R'. If the unbleached pair has FRET efficiency f (and the acceptor-bleached pair has efficiency 0), from (4.1), (4.2), and (4.3) we obtain

$$I_d' = ND_d\beta\left(\alpha\left(1-f\right)Q_d\sigma_d I + \left(1-\alpha\right)Q_d\sigma_d I\right) = ND_d\beta\left(1-\alpha f\right)Q_d\sigma_d I$$

$$I_a' = ND_a\beta\alpha f Q_a\sigma_d I$$

From the definition of the emission ratio, we therefore have

$$R' = \zeta\frac{f}{1/\alpha - f} \tag{4.8}$$

In a sample with a fixed FRET efficiency we can measure R' as a function of exposure to light and compare to the initial unbleached ratio R to determine α:

$$\alpha = \frac{R'}{R}\cdot\frac{R+\zeta}{R'+\zeta} \tag{4.9}$$

Once α is known, we can compare I_a' (during bleaching) and I_a (before bleaching) to determine β.

Knowing the fraction of unbleached acceptors is necessary to accurately compare ratio changes between bleached and unbleached samples. If we have a FRET efficiency change Δf (with $\Delta f \ll f$) in the unbleached samples, then

$$\Delta R' = \zeta\left(\frac{f+\Delta f}{1/\alpha-\left(f+\Delta f\right)} - \frac{f}{1/\alpha - f}\right) \approx R'\frac{\Delta f}{f\left(1/\alpha - f\right)} \tag{4.10}$$

Comparing this to (4.6) and using (4.5) and (4.8) gives us the approximation

$$\frac{\Delta R}{R} \approx \frac{\Delta R'}{R'}\cdot\frac{R}{R'} \tag{4.11}$$

for small FRET efficiency changes. Thus, in photobleached samples, it is not enough to simply calculate the fractional ratio change $\Delta R'/R'$–we must also estimate the bleaching $B = R'/R$.

There are two primary methods we use to determine bleaching. The first is to take a reference sample with a constant FRET efficiency, expose it to light, and measure $R'(t)$. Since $R(t) = R(0) = R'(0)$, we can find $B(t)$. We then simply need to know how long our sample has been exposed to light of that intensity, and use the appropriate value of $B(t)$. Unfortunately, this method is somewhat inconvenient in practice since it relies on illumination that is the same for the experiment as for the reference sample. An alternative is to fit an expected bleaching curve to points of inactivity in an experimental trace (i.e. where we expect $R(t) = R(0)$); a method for finding such points is outlined in section 4.5.1.

Given a time-series measurement $R'(t)$, an estimate of bleaching $B(t)$ for each time, and a baseline (unbleached) ratio level R_0, the appropriate correction to preserve the magnitude of ratio change measurements is

$$R(t) \approx R_0 + \left(R'(t) - B(t)R_0\right)/B(t)^2 \tag{4.12}$$

The sequence produced using this manipulation will preserve both absolute ratio values and the magnitude of ratio changes. Typically the fractional ratio change will be of interest, which is simply $(R(t) - R_0)/R_0$.

When taking a series of ratio measurements over time, it would be convenient to have an expected bleaching curve. If the donor is relatively unbleachable and the FRET efficiency is constant, the acceptor bleaching will be exponential given a first order kinetic model; one might use an exponential of the form $\alpha = A + Be^{-t/\tau}$. In fact, given the complication of directly measuring α, we typically use a fit of the form $R' \approx R((1 - A) + A \cdot e^{-t/\tau})$. While this may incur moderate error, our goal is to use this in intact, behaving animals where there is a wide variability of responses. This inherent variability is expected to be much larger than the error introduced by fitting an inappropriately-shaped curve to estimate bleaching.

Nonetheless, it is worth briefly examining when this estimate is likely to be poor. First, R' is not linear in α, so we do not expect R' to follow an exponential; comparison of (4.5) and (4.8) shows that the approximation is a bad one when α is small (i.e. a large

fraction of the acceptor has bleached). Second, α is also not expected to be a single exponential if the donor also undergoes significant bleaching. If the donor bleaching rate is k_{db} then the fraction of excitations that result in bleaching is $k_{db}/(k_{dr}+k_{dn})$ when the acceptor is bleached and $k_{db}/(k_{dr}+k_{dn}+k_{dt})$ when it is not. With a little algebra, we find that the paired donor bleaches a factor of $1-f$ more slowly than the unpaired donor, which makes the situation more complicated than first-order. Exponential estimation is therefore only good for modest levels of bleaching. Direct measurement of baseline bleaching also is problematic: the rate of bleaching is activity dependent. We saw above that the donor bleaching depends on $1-f$, and f is activity dependent. And the acceptor's excitation is proportional f, so its bleaching also is proportional to f and thus varies with activity. Consequently, baseline photobleaching measurement is best avoided unless activity is minimal. Thus, in the absence of complex models and extensive fitting, (4.12) should only be used to correct for minimal bleaching–perhaps on the order of 25%. We typically observe bleaching of this level after a minute or two when imaging *C. elegans* neurons. Longer recordings could be corrected by waiting for a period of inactivity and performing a new fit from there on.

4.2.3 Crosstalk

Thus far we have been assuming that we can excite our donor fluorophore and measure fluorescence emitted by the donor alone, and by the acceptor alone. Unfortunately, microscopy is rarely this ideal. The acceptor will be directly excited at a rate $\sigma_a I$. Further, a fraction C_d of light emitted by the donor may be detected on the acceptor channel, and vice versa. We need a replacement for (4.4). If we denote the measured intensities by $I_a^\dagger$ and $I_d^\dagger$ we have

$$\begin{pmatrix} I_a^\dagger \\ I_d^\dagger \end{pmatrix} = N \begin{bmatrix} D_a & C_d \\ C_a & D_d \end{bmatrix} \begin{pmatrix} i_a + Q_a\sigma_a I \\ i_d \end{pmatrix} \tag{4.13}$$

where D_d and D_a are the detector quantum efficiencies through the desired channels and C_d and C_a are the efficiencies through the wrong channel. D_d/C_d can be deter-

mined by measuring the intensity from lone donor; D_a/C_a can be determined by looking at the emission when directly exciting lone acceptor. If we invert the matrix we can obtain the corrected measured intensities

$$\begin{pmatrix} I_a^\star \\ I_d \end{pmatrix} = \frac{1}{1 - \frac{C_a}{D_a}\frac{C_d}{D_d}} \begin{bmatrix} 1 & -C_d/D_d \\ -C_a/D_a & 1 \end{bmatrix} \begin{pmatrix} I_a^\dagger \\ I_d^\dagger \end{pmatrix} \tag{4.14}$$

where $I_a^\star$ is the measured acceptor intensity including excitation crosstalk, and thus

$$\begin{pmatrix} I_a^\star \\ I_d \end{pmatrix} = \begin{pmatrix} ND_a i_a + ND_a Q_a \sigma_a I \\ ND_d i_d \end{pmatrix} \tag{4.15}$$

as before, that is, simply scalar multiples of the emitted intensities. C_d/D_d can be determined by measuring the intensity of a solution containing the donor fluorophore only; C_a/D_a can be determined by looking at the emission when directly exciting a solution containing only acceptor. Thus, if we know the emission crosstalk, we can use the "emission unmixing" matrix in (4.14) to obtain emission-crosstalk-free intensities valid for use in the equations of the previous section. (It is also perfectly acceptable to omit the constant $1/\left(1 - C_a C_d / D_a D_d\right)$ and just treat that as part of the measurement quantum efficiencies; since it is just a constant, it will cancel out in all ratios.)

So far, we have removed emission crosstalk but the excitation crosstalk $ND_a Q_a \sigma_a I$ remains. We can measure $ND_a Q_a \sigma_a I$ relative to $ND_d Q_d \sigma_d I$ by observing an equimolar mixture of donor and acceptor and exciting at the donor wavelength. Since there is no energy transfer, $i_a = 0$ and we measure $I_a^\star / I_d = D_a Q_a \sigma_a / D_d Q_d \sigma_d = A$. With this measured factor we can use (4.15) to write

$$R^\star = \frac{I_a^\star}{I_d} = \zeta \frac{f}{1-f} + \frac{A}{1-f} \Rightarrow f = \frac{R^\star - A}{\zeta + R^\star}$$

for the donor acceptor pair. Solving for I_a using equation (4.5) gives

$$I_a = I_a^\star \left(1 - \frac{A}{R^\star} \cdot \frac{1 + R^\star/\zeta}{1 + A/\zeta}\right) \tag{4.16}$$

To review, there are four steps for compensating for excitation and emission crosstalk. First, use solutions of isolated donor and acceptor to determine the crosstalk

coefficients C_d/D_d and C_a/D_a and find the emission unmixing matrix in (4.14). Second, excite an equimolar mixture of donor and acceptor at the donor frequency to determine the excitation crosstalk efficiency ratio A. Third, induce FRET changes and measure $\Delta I_a^\star$ and ΔI_d to estimate ζ. Finally, find I_a using (4.16) and compute $R = I_a/I_d$ as always. (The calculations for the last two steps can easily be done repeatedly to improve the estimate of ζ.)

When combining crosstalk corrections with photobleaching corrections, one should apply unmixing in all cases, but should only use (4.16) on the unbleached fraction. That is, one should use $R^\star/\alpha$ in place of $R^\star$ in that equation. To compute α itself, one can just use bleached and unbleached $R^\star$ in (4.9) instead of R' and R. Again, the computations can be done iteratively (correcting α, then R, then α, etc.) each time to get a more accurate result. Also, it may become necessary to take the donor-bleached population into account if there is significant excitation crosstalk and significant donor bleaching.

4.2.4 Signal-to-Noise maximization

Currently, the most economical system for rapid ratiometric imaging is a cooled CCD camera with a device to project both donor and acceptor channels simultaneously onto the same CCD chip (see, for instance, Figure 2.1a). CCD cameras have several sources of noise, including photon shot noise, readout noise, and dark current [Christenson 2000]. Photon shot noise arises from the variation in the number of photons captured by the detector (strictly speaking, the number of electrons, as an incident photon will send an electron into an excited state where it can relax into a potential well). Since the capture of photons is a Poisson process, the noise is proportional to the square root of the number of captured photons, and therefore is intensity-dependent. Readout noise arises in the process of converting current from electrons in a potential well to a digital number, and is typically constant for a given camera (although some cameras provide slower readout with reduced readout noise). Dark current comes from the leak of thermally excited electrons into potential wells; although the mean can be easily subtracted, the deviation in the leak causes noise. Noise from dark cur-

rent is independent of the sample intensity but is proportional to the square root of the exposure time. In addition to these sources of noise, which are independent from pixel to pixel, timepoint to timepoint, and from each other, fluctuations in the light source can cause excitation intensity changes on a variety of timescales, and sample motion can affect both excitation and emission intensities.

Let us denote a noise-perturbed signal with a tilde. Combining all the noise sources above gives us

$$\begin{aligned} \widetilde{I_a} &= I_a + n_{s,I_a}\sqrt{I_a} + n_{rd,I_a} + n_{lm}I_a \\ \widetilde{I_d} &= I_d + n_{s,I_d}\sqrt{I_d} + n_{rd,I_d} + n_{lm}I_d \end{aligned} \tag{4.17}$$

where n_{rd} is the combined dark current and readout noise, n_{lm} is the combined noise from light source fluctuations and motion artifacts, and $n_{s,I_a}\sqrt{I_a}$ and $n_{s,I_d}\sqrt{I_d}$ are the photon shot noise for acceptor and donor respectively. To maximize the signal-to-noise ratio, our first instinct might be to increase the illumination intensity until I_a or I_d is near the maximum that our detector can handle. The last noise term scales with the intensity, making this approach of limited use in improving the intensity S/N ratio. However, the noise perturbed ratio is given by

$$\widetilde{R} = \frac{\widetilde{I_a}}{\widetilde{I_d}} = R\frac{1 + n_{lm} + \frac{n_{s,I_a}}{\sqrt{I_a}} + \frac{n_{rd,I_a}}{I_a}}{1 + n_{lm} + \frac{n_{s,I_d}}{\sqrt{I_d}} + \frac{n_{rd,I_d}}{I_d}} \approx R\left(1 + \frac{n_{s,I_a}}{\sqrt{I_a}} - \frac{n_{s,I_d}}{\sqrt{I_d}} + \frac{n_{rd,I_a}}{I_a} - \frac{n_{rd,I_d}}{I_d}\right) \tag{4.18}$$

when all noise terms are small relative to the intensities. As is often claimed, ratioing removes the illumination and motion artifact noise (at least to the first approximation). Note that this only occurs if the two intensities are measured simultaneously; otherwise n_{lm} may change between measurement of the two channels.

Equation (4.18) also gives us insight into how to minimize noise in the ratio. Note that the dimmer of I_a and I_d will contribute the dominant noise terms to $\widetilde{R}$. This suggests that we should try to have I_a and I_d as close as possible so that both can be raised to near the maximum possible for our detector; one way to do this is to use neutral density filters or narrower bandpass emission filters to lower the brighter intensity until it is equal to the dimmer one. Then the intensity of the excitation light can be increased to compensate. But, alternatively, one could increase the excitation

light by the same amount, and acquire images more rapidly, then average multiple frames to reduce the noise. To decide which method is superior, suppose that I_a is k times brighter than I_d, with $k > 1$. (The analysis is similar with $I_d > I_a$.) With the neutral density approach, I_d becomes kI_d and our noise term is

$$\frac{n_{s,I_a}}{\sqrt{I_a}} - \frac{n_{s,I_d}}{\sqrt{kI_d}} + \frac{n_{rd,I_a}}{I_a} - \frac{n_{rd,I_d}}{kI_d}$$

Alternatively, if we average k frames ($k > 1$), we will reduce all noise terms by factor $\sqrt{k}$ (possibly more, if dark current is large relative to readout noise, since the decreased exposure time should decrease dark current), giving

$$\frac{n_{s,I_a}}{\sqrt{kI_a}} - \frac{n_{s,I_d}}{\sqrt{kI_d}} + \frac{n_{rd,I_a}}{I_a\sqrt{k}} - \frac{n_{rd,I_d}}{I_d\sqrt{k}}$$

Comparing the size of these two factors gives us our answer. The condition is a little easier to evaluate if we note that n_{rd} is similar for both channels and we write everything in terms of I_a and k. Then, if

$$|n_{s,I_a}|\sqrt{I_a} + |n_{rd}|\sqrt{2} < \frac{1}{\sqrt{k}}|n_{s,I_a}|\sqrt{I_a} + |n_{rd}|\sqrt{1+k^2}$$

the neutral density method is superior; otherwise we should acquire images faster, if possible. The key for evaluating this inequality is the relative size of the photon shot noise, n_{s,I_a}, and the readout and dark-current noise n_{rd}. If the readout noise is larger, we are better off using the neutral density method since $\sqrt{2} < \sqrt{1+k^2}$; if photon shot noise dominates, $1 < 1/\sqrt{k}$ so we should increase our image capture rate. Both sources of noise can be estimated by making measurements of pixel-to-pixel intensity variation of a uniform brightfield under different illumination intensities; the variation should fit a curve of the form $A + B\sqrt{I}$, where A is n_{rd} and B is n_s. On our system, $B\sqrt{I} \gg A$, so we try to use increased capture rates to reduce our noise. Note that both approaches increase incident light by a factor of k and therefore increase photobleaching; when this is unacceptable, we typically decrease light levels until n_{rd} becomes an important factor, then increase exposure time.

Most of the quantities we wish to measure are ratios or are functions of ratios and the noise analysis is similar to the above. However, we are not as fortunate with the

total quantum efficiency ratio ζ. If we consider only the illumination/motion noise n_{lm}, we find that

$$\widetilde{\zeta} = -\frac{\widetilde{\Delta I_a}}{\widetilde{\Delta I_d}} = -\frac{\widetilde{I_{a2}} - \widetilde{I_{a1}}}{\widetilde{I_{d2}} - \widetilde{I_{d1}}} = -\frac{\Delta I_a + I_{a2}n_{lm2} - I_{a1}n_{lm1}}{\Delta I_d + I_{d2}n_{lm2} - I_{d1}n_{lm1}} = \zeta\frac{1 + \frac{n_{lm2}I_{a2}}{\Delta I_a} - \frac{n_{lm1}I_{a1}}{\Delta I_a}}{1 + \frac{n_{lm2}I_{d2}}{\Delta I_d} - \frac{n_{lm1}I_{d1}}{\Delta I_d}}$$

Since ΔI_a and ΔI_d have opposite sign, intensity errors reinforce each other in the ratio rather than canceling. As such, to make an accurate measurement of ζ, one needs large intensity changes ΔI_a and ΔI_d and as little illumination and motion noise as possible. Averaging over a large number of trials may also be necessary.

If we wish to measure noise directly, the easiest place to do it is directly on the ratio. If we have a series of timepoints, we expect the point-to-point variation in the ratio to be, on average $\sqrt{2}$ times the deviation from the mean. However, time-varying signals which are infrequent or slow relative to the rate of data acquisition will have a minimal impact on the point-to-point variation. Therefore, if one of these conditions holds,

$$\overline{n}_R \approx \frac{1}{\sqrt{2M}}\sqrt{\sum_{t=1}^{M-1} |R(t+1) - R(t)|^2} \tag{4.19}$$

is a reasonable estimate of the mean noise in the ratio. We typically make recordings where only a small fraction (<5%) of the recording exhibits rapid ratio changes, so (4.19) is usually a good measure for us. In cases where it is not, our frame rate is still faster than the ratio change events we are measuring, so events show temporal correlation; this correlation can be detected to remove the offending timepoints, if desired.

Variable	Description
A	fractional excitation crosstalk
$B(t)$	bleaching profile of baseline ratio
C_a	quantum efficiency of acceptor emission (crosstalk) into donor channel
C_d	quantum efficiency of donor emission (crosstalk) into acceptor channel
D_a,D_d	quantum efficiency of acceptor/donor detection in desired channel
I	excitation (illumination) intensity
I_a,I_d	measured acceptor/donor intensity
K_d	dissociation constant for cameleon binding calcium
N	number of molecules illuminated
N_0,N_1	number of molecules in ground state/first excited state
Q_a,Q_d	quantum efficiency of acceptor/donor
R	emission ratio
ΔR	change in emission ratio
f	FRET efficiency
Δf	change in FRET efficiency
i	emission intensity per unit molecule
i_a,i_d	emission intensity per acceptor/donor
$k_{a\square}$,$k_{d\square}$	rate $k_\square$ for acceptor/donor, $\square \in \{b, e, n, r, t\}$
k_b	rate of photobleaching from excited state
k_e	rate of excitation of ground state
k_n	rate of nonfluorescent decay from excited state
k_r	rate of fluorescent decay from excited state
k_t	rate of energy transfer from excited donor to ground state acceptor
$\overline{n}_R$	mean noise in ratio
n_{lm}	fractional noise from illumination and motion artifacts
n_{rd}	readout noise and dark current
n_s	photon shot noise
α	fraction of unbleached acceptor
β	fraction of unbleached donor
ζ	total quantum efficiency ratio
σ_a ,σ_d	absorbance cross section of acceptor/donor
Decoration	**Description**
I'_a,I'_d,R'	measurements perturbed by photobleaching
$I^\dagger_a$,$I^\dagger_d$	intensity measurements corrupted by crosstalk
$I^\star_a$,$R^\star$	measurements altered by direct excitation of acceptor
$\widetilde{I}_a$,$\widetilde{I}_d$,$\widetilde{R}$,$\widetilde{\zeta}$	measurements perturbed by noise
$R^\clubsuit$	measured ratio with altered dynamic range

Table 4.1: Summary of commonly used variables introduced in sections 4.2 and 4.3.

4.3 Considerations for Using Protein-Based Calcium Indicators

There are a number of factors that arise when using protein-based calcium indicators as opposed to a generic small molecule or protein indicator based on a FRET efficiency change. In particular, proteins are degraded and compartmentalized; they may interact with endogenous proteins; and calcium indicators also function as calcium buffers, which may perturb the cell and its apparent response. We treat each of these considerations below.

4.3.1 Degradation and compartmentalization of indicator

Protein-based indicators present in the environment of the cell are expected to be subject to the same processes as any other cellular protein. Of particular interest to us is the possible presence of partially degraded yet still fluorescent proteins, and compartmentalization of a fraction of the indicator in organelles, which will leave some of the indicator molecules in a different microenvironment.

Degraded molecules with the donor still intact will have all the same properties as molecules with a bleached acceptor; either way, the acceptor is inactive. This form of degradation will manifest itself as decreased ratio in the cell as compared to an in vitro sample of fully intact protein; if the difference is especially large, one may wish to use (4.12) to correct the measurements. Smaller differences can be partially offset by simply using $\Delta r/r$ to report changes.

Degraded molecules which are no longer responsive to calcium, but are still fully fluorescent, effectively add a background to both donor and acceptor channels. Likewise, if the indicator is compartmentalized into an organelle, it may be have an altered resting ratio and may be unresponsive to changes in cytosolic calcium, also contributing to background. This background can be determined by setting the calcium levels in the tissue to zero and saturating concentrations (for example, by incubating with ionomycin and either 1mM EGTA or 1mM calcium) and measuring the ratio change.

In the ideal case, if I_{a0} and I_{d0} are the zero-calcium intensities and I_{aM} and I_{dM} are the high-calcium intensities, from (4.7) we expect that

$$\left(I_{aM} - I_{a0}\right) / \left(I_{dM} - I_{d0}\right) = -\zeta$$

and with a little algebra we find that

$$\frac{I_{a0}}{I_{aM}} = \frac{1/\zeta + 1/R_M}{1/\zeta + 1/R_0} \qquad \frac{I_{d0}}{I_{dM}} = \frac{\zeta + R_M}{\zeta + R_0}$$

Since by definition the backgrounds I_{aB} and I_{dB} are unchanged with changing calcium, we expect the measured ratios $R_0^{\clubsuit}$ and $R_M^{\clubsuit}$ in zero and high calcium to be

$$R_0^{\clubsuit} = \frac{I_{a0} + I_{aB}}{I_{d0} + I_{dB}} = \frac{I_{a0}}{I_{d0}} \left(\frac{1 + I_{aB}/I_{a0}}{1 + I_{dB}/I_{d0}} \right) = R_0 \frac{1 + x_a}{1 + x_d}$$

$$R_M^{\clubsuit} = R_M \frac{1 + I_{aB}/I_{aM}}{1 + I_{dB}/I_{dM}} = R_M \frac{1 + x_a \frac{R_M}{R_0} \frac{\zeta + R_0}{\zeta + R_M}}{1 + x_d \frac{\zeta + R_0}{\zeta + R_M}} \tag{4.20}$$

We can solve these for x_a and x_d which are the fractional correction factors we'll need to apply to the intensities (or ratios):

$$x_a = \frac{\frac{\zeta + R_0}{\zeta + R_M} \left(\frac{R_0}{R_0^{\clubsuit}} - 1 \right) - \left(\frac{R_M}{R_M^{\clubsuit}} - 1 \right)}{\left(\frac{R_M}{R_M^{\clubsuit}} \cdot \frac{R_M}{R_0} - \frac{R_0}{R_0^{\clubsuit}} \right) \frac{\zeta + R_0}{\zeta + R_M}}$$

$$x_d = \frac{\frac{R_M}{R_0} \cdot \frac{\zeta + R_0}{\zeta + R_M} \left(\frac{R_0^{\clubsuit}}{R_0} - 1 \right) - \left(\frac{R_M^{\clubsuit}}{R_M} - 1 \right)}{\left(\frac{R_M^{\clubsuit}}{R_M} - \frac{R_0^{\clubsuit}}{R_0} \cdot \frac{R_M}{R_0} \right) \frac{\zeta + R_0}{\zeta + R_M}}$$

These formulas are admittedly unattractive, but once the constants x_a and x_d are determined we can note that (4.20) holds with any R_i substituted for R_M and solve for R_i in terms of $R_i^{\clubsuit}$ to get the correction formula:

$$R_i = R_i^{\clubsuit} \left(\frac{1 - \zeta/R_i^{\clubsuit}}{2 + 2x_a\left(1 + \zeta/R_0\right)} + \sqrt{\left(\frac{1 - \zeta/R_i^{\clubsuit}}{2 + 2x_a\left(1 + \zeta/R_0\right)} \right)^2 + \frac{\zeta/R_i^{\clubsuit} + x_d \frac{R_0 + \zeta}{R_i^{\clubsuit}}}{1 + x_a\left(1 + \zeta/R_0\right)}} \right) \tag{4.21}$$

While one would certainly hope not to have to use this formula, the point remains that arbitrary accumulation of background fluorescence can be fully compensated for simply by measuring ratios at maximum and minimum fluorescence.

Given the time-consuming nature of finding the maximum and minimum ratio, in most cases one will wish to merely check that degradation and compartmentalization is minor and then proceed to ignore it. In the cases where we checked, the majority of the protein seemed functional, and we therefore assumed that we had a high fraction of functional, accessible protein in all preparations and samples that we observed.

4.3.2 Disruptive interactions with endogenous proteins

The cameleon indicator uses the native calcium binding protein calmodulin and the M13 peptide, which has high affinity for the calcium-bound state of calmodulin, to generate a conformational change that alters the FRET efficiency between CFP and YFP domains on the ends of the protein. Native calmodulin interacts with many different proteins in vivo, raising the question of whether cameleon will also interact with these proteins and possibly disrupt their function. Further, cameleon might impair normal calcium signaling if M13 binds to endogenous calmodulin rather than the calmodulin in cameleon. Although we cannot rule out these interactions, we have a number of lines of evidence to suggest that the cameleon is functioning normally and is not disrupting biologically relevant interactions in *C. elegans*.

1. Measurements of maximum and minimum ratio in the pharyngeal muscle gave a near-normal magnitude of ratio change, suggesting that the dynamic range of cameleon has not been altered.

2. The presence of calcium transients was not strongly affected by levels of cameleon; if interactions with cameleon were preventing calcium transients we would expect to see a dependence on cameleon concentration.

3. Worms expressing cameleon in the pharnyx, body wall muscles, nervous system, and mechanosensory neurons showed normal pharyngeal pumping rates, movement, coordination, and responsiveness to light touch (plate tapping), respectively, consistent with cameleon having little or no effect on behaviorally relevant cellular processes.

However, there is some evidence that cameleon may have an effect in some cell types.

1. Some, but not all constructs with cameleon expression driven in the mechanosensory neurons by the *mec-4* promoter showed abnormal cell morphology. In particular, when the cameleon construct was in the *mec-4* mutant background, a significant number of worms showed abnormal neuronal morphology.

2. A construct expressing cameleon in the ASH chemoavoidance neuron using the *sra-6* promoter was behaviorally normal. However, when cameleon was fused to the *osm-10* promoter plus a short N-terminal peptide of the OSM-10 protein, chemoavoidance was diminished or abolished in a majority of the animals, and no calcium transients were observed. While the *sra-6* result suggests that cameleon is not wholly at fault, it is not known whether the *osm-10* defect was a result of the peptide alone.

3. There are reports [Varda Lev-Ram, pers. comm.] that transgenic mice expressing cameleon throughout the body show smaller ratio changes in some tissues than is obtained from transient transfection of viruses. This suggests that partial inactivation of cameleon may occur developmentally, or that mice with properly functioning cameleon constructs are inviable.

4. Rates of habituation to classical tap stimulation protocols were increased in animals expressing cameleon in the touch neurons, although initial sensitivity to tap was similar to wild-type.

Thus, although cameleon seems to have a minimal impact in many tissues, it is advisable to verify that the expression is not altering behavior or other known properties. Presumably, similar precautions should be taken for other protein-based calcium indicators.

4.3.3 Calcium buffering

Cameleon, like most calcium indicators, is a calcium binding protein. Even if the calcium binding does not produce behavioral defects, buffering can affect the apparent total concentration of calcium and the kinetics of the return to baseline calcium.

Calmodulin has four calcium binding sites; in many versions of cameleon (for example, the YC2 series), all four binding sites are active. In general, there may be multiple calcium-bound configurations with different FRET efficiencies, but to simplify the analysis we will consider the simple case where n calcium atoms bind cameleon in the absence of any other calcium buffers:

$$\mathrm{YC} + n \cdot \mathrm{Ca}^{2+} \rightleftharpoons \mathrm{YC.Ca}^{2+}$$

If the FRET efficiency of calcium-unbound and calcium-bound cameleon is f_{YC} and $f_{\mathrm{YC.Ca^{2+}}}$ respectively, the mean FRET efficiency will depend on the concentration of each species:

$$f = \frac{[\mathrm{YC}]}{[\mathrm{YC}] + [\mathrm{YC.Ca}^{2+}]} f_{\mathrm{YC}} + \frac{[\mathrm{YC.Ca}^{2+}]}{[\mathrm{YC}] + [\mathrm{YC.Ca}^{2+}]} f_{\mathrm{YC.Ca^{2+}}} \tag{4.22}$$

To simplify our analysis again, we will assume a first-order reaction (i.e. that calcium binding is perfectly cooperative), giving

$$K_d = \frac{[\mathrm{YC}] \cdot [\mathrm{Ca}^{2+}]}{[\mathrm{YC.Ca}^{2+}]}$$

Now we can consider the case where there is an influx of calcium into an initially zero-calcium environment. If calcium influx yields a total calcium concentration of $[\mathrm{Ca}^{2+}]_0$ and the initial concentration of cameleon is $[\mathrm{YC}]_0$, we have

$$[\mathrm{YC.Ca}^{2+}] \cdot K_d = \left([\mathrm{YC}]_0 - [\mathrm{YC.Ca}^{2+}]\right) \cdot \left([\mathrm{Ca}^{2+}]_0 - n[\mathrm{YC.Ca}^{2+}]\right) \tag{4.23}$$

From (4.22) we see that our measurement scales as $[\mathrm{YC.Ca}^{2+}]/[\mathrm{YC}]_0$; in the case where both $[\mathrm{YC}]_0$ and $[\mathrm{Ca}^{2+}]_0$ are significantly less than K_d, we can rearrange (4.23) to find that $[\mathrm{YC.Ca}^{2+}]/[\mathrm{YC}]_0 \approx [\mathrm{Ca}^{2+}]_0/K_d$. Therefore, the ideal indicator is one with a relatively high K_d but a great enough dynamic range to detect small fractions of calcium-bound indicator.

Unfortunately, the K_d of the first binding of the YC2 versions of cameleon appear to be in the sub-micromolar range, making the condition $[\mathrm{YC}]_0 \ll K_d$ rather implausible. Indeed, comparison of neuronal expression of cameleon in *C. elegans* to microdroplets of purified CFP indicate that concentrations on the the order of 10μM are necessary for imaging. In this case, we can solve (4.23) for $[\mathrm{YC.Ca}^{2+}]$ and use approximations based on $[\mathrm{YC}]_0 \gg K_d$ and $[\mathrm{YC}]_0 > [\mathrm{Ca}^{2+}]_0$ to find

$$\Delta\overline{f} \propto \frac{[\mathrm{YC.Ca}^{2+}]}{[\mathrm{YC}]_0} \approx \frac{[\mathrm{Ca}^{2+}]_0/n}{[\mathrm{YC}]_0} \tag{4.24}$$

Thus we expect FRET efficiency changes to be linear in total calcium influx and inversely proportional to the concentration of the indicator; the rate of FRET efficiency change should therefore be proportional to the rate of calcium influx. Given the relationship between FRET efficiency and ratio in (4.5), we do not expect the linearity to extend to ratio measurements, but the point remains that the size of signals will be inversely related to the concentration of the indicator. This also means that cameleon will function as a calcium buffer, which may have significant biological effects, including causing the upregulation of calcium flux to compensate. Of course, cells contain endogenous calcium buffers, which will affect the above results. Buffers with a significantly higher affinity than cameleon (and similar or faster kinetics) will essentially soak up calcium until they are full and cameleon will measure the remainder. Buffers with significantly lower affinity (e.g. tens of micromolar) will not affect calcium binding to cameleon. If we have buffers of similar affinity ($\sim 1\mathrm{mM}$) of concentration $[\mathrm{B}]_0$ then our above analysis holds with $[\mathrm{B}]_0 + [\mathrm{YC}]_0$ substituted in for $[\mathrm{YC}]_0$ and $[\mathrm{YC.Ca}^{2+}] + [\mathrm{B.Ca}^{2+}]$ for $[\mathrm{YC.Ca}^{2+}]$. $[\mathrm{YC.Ca}^{2+}]/[\mathrm{YC}]_0$ is still proportional to our ratio readout, giving

$$\Delta\overline{f} \propto \frac{[\mathrm{YC.Ca}^{2+}]}{[\mathrm{YC}]_0} \approx \frac{[\mathrm{Ca}^{2+}]_0/n}{[\mathrm{B}]_0 + [\mathrm{YC}]_0} \tag{4.25}$$

Thus the reciprocal of the measured (mean) FRET efficiency change should be linear in the concentration of the indicator; if fluorescent intensity can be used to measure the concentration of the indicator, this potentially provides a way to estimate the effective

concentration of intracellular buffer $[\mathrm{B}]_0$ where

$$[\mathrm{B}]_0 \approx \sum [\mathrm{B}_i]_0 \left(\frac{K_{d,\mathrm{YC}}}{K_{d,\mathrm{B}_i}} \right)$$

i.e., weighted by the relative K_d of each endogenous buffer relative to that of cameleon. A word of caution–at this point we are making so many approximations that this is at best a very rough estimate. An extensive treatment of using the small molecule calcium indicator fura-2 to measure calcium fluxes and buffers is given in [Neher 1995]; the results derived there are readily applicable to cameleon also.

4.4 Automated Low-Noise Measurements in Living, Moving Samples

In order to use imaging techniques to detect activity in behaving animals, we need recording techniques that are compatible with living, moving organisms. Since organism-to-organism variability typically necessitates dozens of trials for any given condition, any computational methods used to improve the quality of the data should require a minimum of input from the experimenter. In this section we consider how to use ratiometric imaging to monitor FRET efficiency changes in cameleon in a tissue of interest, and the computational techniques necessary to automatically correct for noise and calculate ratio changes within the tissue over time.

4.4.1 Advantages and requirements of ratiometric imaging

The primary advantage of ratiometric imaging as compared to intensity-based imaging is its independence from many sources of noise. For example, an unstable light source can make intensity measurements completely unintelligible. Indeed, our mercury arc lamp routinely introduces spikes and dips into intensity measurements that make it difficult to determine changes in intensity due to a change in FRET efficiency. However, the intensity ratio (4.5) is independent of intensity; the artifacts in intensity in each channel cancel–see, for example, Figure 3.1c.

In order to achieve this cancellation, it is necessary for the intensity measurements in each channel be made simultaneously, or at least a short time apart relative to the timescale of artifactual fluctuation and changes in FRET efficiency. With a very stable light source and nonmoving samples with slowly-changing ratios, it can be sufficient to take alternating images of the donor and acceptor channels every second or so. However, to image the activity of excitable cells in a moving *C. elegans*, rapid simultaneous imaging is critical. For example, the pharyngeal muscle can contract and relax in a few tens of milliseconds, causing both motion artifacts and changes in FRET efficiency.

The basic method for making simultaneous intensity measurements relies on using a dichroic mirror that will pass the acceptor's emission frequencies while reflecting the donor's. In confocal microscopes, photomultiplier tubes then detect the intensity of each channel. Since we don't need the optical sectioning capability of a confocal microscope–indeed, in the transparent body of the worm, with only tissues of interest expressing our indicator, off-axis light is actually a valid signal–we instead use a wide-field image splitter that recombines the two separated light paths onto a single CCD chip. The two intensities are thus perfectly synchronized and successive images can be taken at up to the maximum frame rate of the camera (50+Hz in our case). We can then calculate the intensity ratio on a pixel-by-pixel basis. (See section 4.4.6.)

4.4.2 Frame alignment

Wide-field imaging poses a particular problem for ratiometric measurements: the image of the donor channel and of the acceptor channel need to be properly aligned in order to compute an accurate pixel-by-pixel ratio. The problem is particularly acute at the edges of bright objects. Simply aligning the two images to within one pixel is not sufficient to avoid huge artifacts at the edges of bright objects. For example, if the optics allow neighboring pixels to differ by a factor of two in intensity, and the two images are off by just 0.1 of a pixel, we can have $I_a = 0.9 \cdot RI_d + 0.1 \cdot R\left(2I_d\right) = 1.1 \cdot RI_d$, or an error of 10%. When we are dealing with ratio changes in the single digits, as is common, errors of this magnitude can be significant.

Fortunately, alignment artifacts are relatively easy to spot, as the edges of bright objects have abnormally high and abnormally low ratios on opposite edges. Manual adjustment followed by inspection of the results, or the difference between the position of the same object on each frame (see section 4.4.3), can yield the offset (x, y) between the two images. Then interpolation methods can be used to re-align the frames exactly. We favor linear interpolation since it is rapid and preserves total intensity. Specifically, if the acceptor frame is shifted a distance (x, y) relative to the donor frame, we define the linear interpolation function

$$\begin{aligned} L(i, j, \Delta x, \Delta y, I) &= (1 - \Delta x)(1 - \Delta y) I_{(i,j)} + (1 - \Delta x) \Delta y I_{(i,j+1)} + \\ &\quad \Delta x (1 - \Delta y) I_{(i+1,j)} + \Delta x \Delta y I_{(i+1,j+1)} \end{aligned} \tag{4.26}$$

where $0 \leq \Delta x < 1, 0 \leq \Delta y < 1$, and I is an array of intensity values. We then compute the interpolated pixel values as

$$I^{(\text{new})}_{a(i,j)} = L\left(\left\lfloor i + \frac{x}{2} \right\rfloor, \left\lfloor j + \frac{y}{2} \right\rfloor, i + \frac{x}{2} - \left\lfloor i + \frac{x}{2} \right\rfloor, j + \frac{y}{2} - \left\lfloor j + \frac{y}{2} \right\rfloor, I_a\right)$$

$$I^{(\text{new})}_{d(i,j)} = L\left(\left\lfloor i - \frac{x}{2} \right\rfloor, \left\lfloor j - \frac{y}{2} \right\rfloor, -i + \frac{x}{2} + \left\lfloor i - \frac{x}{2} \right\rfloor, -j + \frac{y}{2} + \left\lfloor j - \frac{y}{2} \right\rfloor, I_d\right)$$

Note that the two frames are shifted equal and opposite amounts. Linear interpolation also functions as a blur of up to a half-pixel, and by moving the two frames in opposite and equal directions until they overlap, the amount of blur is guaranteed to be equal.

4.4.3 Region-of-interest measurement and tracking

We typically want to examine ratio changes in a specific tissue of interest, for example, a single neuron. In order to accomplish this, we can define a region of interest around the tissue of interest and examine the total intensity within that region. However, if the sample is mobile and the region of interest is static, motion can cause inaccurate intensity readings throughout successive frames. If the sample does not have a perfectly uniform ratio, this can cause artifacts in the ratio also (especially a problem if the two

frames are not perfectly aligned). And, of course, if the sample completely leaves the region of interest, the measurements are worthless.

To overcome this problem, we use mobile regions of interest. Since our tissues of interest are almost uniformly brightly fluorescent against a dark background, we use regions that center themselves on local maxima in intensity. In order to achieve this, if our region of interest is A with its center at

$$(x, y) = \frac{1}{\int_A dz\, dw} \left(\int_{(z,w)A} z\, dz\, dw, \int_{(z,w)\in A} w\, dz\, dw \right)$$

we calculate the intensity centroid

$$(c_x, c_y) = \frac{1}{\int_A I(z,w)\, dz\, dw} \left(\int_A z\, I(z,w)\, dz\, dw, \int_A w\, I(z,w)\, dz\, dw \right)$$

where $I(z,w) = L(\lfloor z \rfloor, \lfloor w \rfloor, z - \lfloor z \rfloor, w - \lfloor w \rfloor, I)$ is the linearly interpolated intensity. Note that the intensity centroid is the equivalent of the center of mass or balance point of the region of interest if intensity is interpreted as density. If the region is centered over the local maximum, the center of mass will coincide with the center of the region; if not, the region will be "lopsided" and (c_x, c_y) will be in the direction of the intensity maximum relative to (x, y). We set a threshold ε to determine whether the region is appropriately centered. If $|(x, y) - (c_x, c_y)| < \varepsilon$ we consider the region centered; otherwise, we set (x, y) equal to (c_x, c_y) (or at least move a step in that direction) and compute the centroid at the new position. Through successive iterations we thus approach the intensity maximum.

Although this algorithm is not robust (it can get caught at local minima and saddle points, can get caught in cycles, and so on), in practice it is very fast. Further, due to intrinsic noise in the images, it is extremely unlikely for the centroid-finding algorithm to get caught in a cycle or non-maxima for more than one frame. Thus, although this may not be a perfect method for analyzing single images, it is suitable for automatically positioning regions on long sequences of successive images. Indeed, when trying to analyze thousands of frames of data, automated methods are essential. The above algorithm has therefore been implemented with a graphical user interface in a Java-based program.

In some cases, we may want to measure over a region that is not at a local maximum of intensity. To allow for this, we can also define regions that are at a fixed offset from an intensity-maximum tracking region. Using an offset is inappropriate if the tissue is undergoing distortions or rotations, but it works well for translations, and the primary observed motion of worm tissues is linear translation. In all cases, the intensity is simply calculated as

$$I_{total} = \int_A I(z,w)\,dz\,dw$$

Since $I(z,w)$ is piecewise linear, the integral turns into a sum of linear pieces (approximately one per pixel). The details of how to most efficiently compute the sum will not be described here, save to say that at the moment, our implementation only allows elliptic and rectangular regions of interest. Extension to arbitrary regions of interest is straightforward, if tedious.

Note that perfect alignment is unnecessary and indeed impossible with noisy images. If each pixel has a fractional noise n, a $2m \times 2m$ square of pixels of identical intensity will have a centroid that deviates from the true center on average approximately

$$\sqrt{\frac{1}{(4m^2)^2}\cdot\sum_{i=1}^{m} 4m\,(in)^2} = n\sqrt{\frac{\sum i^2}{4m^3}} = \frac{n}{\sqrt{12}}\sqrt{1+\frac{3}{2m}+\frac{1}{2m^2}} \approx \frac{n}{\sqrt{12}}$$

pixels in each direction. Thus the error in image positioning is essentially independent of region size and depends only on the noise in the image. Since noise in positioning affects only the perimeter of the image, the fractional error of an intensity measurement caused by inaccurate positioning is proportional to $1/m$. With a 12-bit camera operating near the 1 count/photon limit, we will have no less than 6 bits of shot noise, giving at best a region positioning accuracy of about $2^{-6}/\sqrt{12} \approx 0.005$ pixels. We use this number as a guideline to set our centering error threshold ε; typically we use $\varepsilon = 0.02$.

During a single experiment, the offset between two frames does not change physically. However, if corresponding regions on each frame track independently, they may not maintain the same offset. As such, the error in ratio measurement can be slightly

reduced by fixing the offset between regions on donor and acceptor frames. Given the accuracy of the intensity-centering mechanism, the offset only (erroneously) varies significantly when there is an uncorrected fluorescence background in a gradient in the region of interest, and the region of interest moves in and out of this gradient. This condition can be caused by autofluorescence in the *C. elegans* gut, but is rare enough so that we typically track the object of interest independently on each frame. Note that independent tracking is actually an advantage if there are large motions in the image plane and one of the two channels is distorted.

4.4.4 Global and local background subtraction

When we make intensity measurements, we only want to record the intensity of emission from our tissue of interest. However, in addition to fluorescent emission from our sample, there is also often autofluorescence from the worm's gut, dark current in the camera, slight autofluorescence in the agar pad used to mount the worm and the glue used to hold them immobile, stray light from computer monitors, and so on. As a result, there is both a diffuse background signal over the entire field of view as well as individual patches of increased fluorescence that may overlap the tissue of interest.

A histogram of intensity values across the entire image typically shows a large bulge at a low intensity value equal to the global background across the image, plus a small high-intensity hump corresponding to the tissue of interest. The fluorescent emission of the tissue of interest is equal to the difference in intensity between the two, since the background does not come primarily from the focal plane where the tissue of interest is. Although it is possible to use curve-fitting techniques to accurately estimate the peak of the histogram and thus the typical background intensity, if the tissue of interest is small relative to the field of view, the peak falls very close to the mean of all intensities in the image. The median lies even closer (since the few bright pixels skew the mean in proportion to their brightness), and both the median and the mean require $O(n)$ time to compute; however, the slight improvement is not worth the extra work of implementing a Quicksort-like median-finding algorithm.

When the tissue of interest is in a region where there is out-of-focus or scattered light from a nearby brightly fluorescent object, global background subtraction alone is insufficient. In this case, we use local background subtraction by setting a region of interest over a representative patch of background fluorescence near the tissue of interest. We then use the measurement of mean intensity in that region to correct the measured intensity over the tissue of interest, which presumably is the sum of the background and the emission intensity of the tissue of interest. Local background subtraction is especially critical when motion causes a dim tissue of interest to travel through background fluorescence of varying intensities, which would normally cause an artifact in the measured ratio. In these cases, we observe that the artifact is markedly reduced when applying local background subtraction.

Consider a case where the background has not been perfectly subtracted (denoted with a diamond), giving measured intensities of $I_a^{\diamondsuit} = I_a + B_a$ and $I_d^{\diamondsuit} = I_d + B_d$ respectively, where B_a and B_d are the uncompensated background. This gives an error in the ratio:

$$R^{\diamondsuit} = \frac{I_a + B_a}{I_d + B_d} \approx R\left(1 + \frac{B_a}{I_a} - \frac{B_d}{I_d}\right)$$

and in the fractional ratio change:

$$\frac{\Delta R^{\diamondsuit}}{R^{\diamondsuit}} = \frac{\frac{I_a+\Delta I_a+B_a}{I_d+\Delta I_d+B_d} - \frac{I_a+B_a}{I_d+B_d}}{(I_d + B_d)\,/\,(I_a + B_a)} \approx \frac{\Delta R}{R} + \left(1 + \frac{\Delta R}{R}\right)\left(\frac{\Delta I_a B_a}{I_a\,(I_a + \Delta I_a)} - \frac{\Delta I_d B_d}{I_d\,(I_d + \Delta I_d)}\right)$$

which despite the more complicated appearance, still has a first-order error term involving B_a/I_a and B_d/I_d. These formulas cannot be used to correct errors since if we knew B_a and B_d we would have already subtracted them. However, it allows one to estimate the order of magnitude of the error in the ratio for a given error in background subtraction.

4.4.5 Identifying uncompensated errors

Despite our best efforts at removing artifacts from our images, it is not always possible to remove all of them. It then becomes important to be able to identify when the data does not accurately reflect FRET efficiency changes in the tissue of interest.

The primary source of apparent FRET efficiency changes when there are none is probably z-axis movement. The ratio is not guaranteed to be uniform in the z-axis unless the background is perfectly corrected, the imaging system has no chromatic aberration, and the sample has no local variation in the state of the indicator along the z-axis. These conditions are rarely met, so although slight z-axis movements usually result in minimal error, changes large enough to render the tissue of interest significantly out of focus also usually result in a significant ratio change. One method for determining the magnitude of these changes is simply to record several frames while manually changing the focus. Alternatively, one can simply discard data where ratio changes are accompanied by focus changes.

Motion in the xy-plane can also cause artifacts when there is imperfect background subtraction. This tends to manifest itself as a very tight coupling between motion and ratio. Although stimuli that cause excitable cell activity may also cause motion (especially if the cell is a muscle), the timecourse of the motion and the onset and especially the offset of the calcium transient are expected to be different. We typically observe rapid ratio rises followed by gradual decays in response to a calcium transient; motion rarely follows this pattern.

Excitation intensity changes can also cause artifacts when there is imperfect background subtraction. Such errors are usually easy to spot, since the changes in the ratio either are follow correlated changes in both intensities, or are a mirror image of them.

A positive method to identify real FRET efficiency changes is to examine the donor and acceptor intensities for reciprocal changes. Very often, the intensities are too noisy for any reciprocal changes to be detected even if they exist. However, in the cases where reciprocal changes can be detected, they are a good indication of a FRET efficiency change since none of the sources of artifacts are expected to give reciprocal changes (although motion artifacts may). Once the presence of FRET efficiency changes has been established, continued monitoring of reciprocal intensity changes is unnecessary unless there is doubt as to whether a particular ratio change corresponds to a real event.

Finally, note that in a sufficiently long string of random noise, one will tend to get reciprocal intensity changes and therefore a ratio change. Indeed, on average, changes will be reciprocal (though not with the characteristic ratio ζ) half the time. As such, it is important to be able to take images fast enough so that we do not rely on a single data point for any ratio measurements.

4.4.6 Visualization of ratiometric image data

Pixel-by-pixel ratios can yield appealing images of ratios across an entire field of view. Typically, the average intensity of fluorescence is encoded by brightness, while the ratio at each pixel is encoded by color (see, for example, [Tsien and Harootunian 1990]). In addition to generating an aesthetically appealing image, direct visualization of color-coded images and movies can potentially enable one to identify nonuniformities in ratios and ratio changes within tissues of interest. It also makes alignment errors visually obvious (see section 4.4.2).

In choosing a color-encoding scheme, there are a number of desired properties, not all of which can be fulfilled simultaneously. Perhaps most important, if the images are to be used to judge the relative size of ratio changes, is that the color scale be perceptually uniform, that is, that equal steps in ratio at different positions along the color scale result in approximately equal steps of discriminability (or, equivalently, that they feel "about the same distance" perceptually). Second, it is preferable if the coding scheme represents all colors at the same apparent intensity so that color and intensity are orthogonal in the image. Third, to obtain maximum discrimination, we wish to use as much of the display capacity of our monitor or projection device as possible. Fourth, the path through perceptual space should be intuitive, e.g. a rainbow or a fading from color to gray. Finally, the images will be more aesthetically appealing if they are relatively saturated and bright.

We have tried a number of hue-varying color schemes, none of which are ideal for display on RGB monitors. In general, lowered intensity is displayed as a linear combination of black with the full-intensity color corresponding to a given ratio. One

possibility for encoding ratio as a hue is simply to use the HSV color system, where hue is measured in degrees, and is linear between the six corner-points of red $(1,0,0)$, yellow $(1,1,0)$, green $(0,1,0)$, cyan $(0,1,1)$, blue $(0,0,1)$, and magenta $(1,0,1)$, where the (r,g,b) triples represent the fractional intensities in the red, green, and blue display components; the minimum ratio is mapped to blue and linearly extended to the maximum ratio at red. Unfortunately, the perceptual distance between yellow and green is extremely small on most electronic display devices, which renders ratios in that range difficult to perceive. A slight modification of the HSV system, using

$$(r,g,b) = \begin{cases} \left(1, 1 - \frac{2(R_{max}-R)}{R_{max}-R_{min}}, 0\right) & \text{if} \quad R > \frac{R_{max}+R_{min}}{2} \\ \left(\frac{2(R-R_{min})}{R_{max}-R_{min}}, \frac{1}{2} + \frac{R-R_{min}}{R_{max}-R_{min}}, 1 - \frac{2(R-R_{min})}{R_{max}-R_{min}}\right) & \text{otherwise} \end{cases}$$

gives a pleasant, if ad-hoc, rainbow of colors without extreme intensity changes. However, this method also does not preserve intensity values; the maximum ratio value displays as red, which is much dimmer than the middle ratio value (yellow).

To attain perceptual uniformity of color with constant brightness, the CIE L*a*b color coordinate system [CIE 1986] or the Munsell color tables [Munsell 1915 etc.] are often used. We have implemented both, but even when using maximally saturated colors at a given lightness value, the color schemes generated are muted pastels due to the limitations of standard RGB monitors. Although color changes in these schemes are approximately perceptually uniform, the changes are also difficult to perceive at all, which rather defeats the point of visualization. As such, more work needs to be done to develop an adequate compromise between perceptual uniformity and perceptual clarity.

In cases where per-pixel noise is large, displaying ratio values on a per-pixel basis becomes problematic. One approach is to use spatial averaging to reduce the noise, but this blurs the image. A possible solution is to take intensity values from an unblurred image but ratio values computed from a blurred image; this gives the impression of a more uniform ratio across the sample. We typically avoid this, since the CCD images we produce tend to be relatively low-noise.

In summary, color coding allows one to visualize ratiometric image data, but current coding schemes either suffer from severe perceptual nonuniformity or are difficult to view. As such, while movies of ratiometric images can be colorful and enjoyable to watch, as a data analysis tool they should primarily be used to give an indication of where to apply more quantitative techniques. This is not to say that visualization is unimportant; without a reasonable visualization technique, it is difficult to notice potentially interesting spatial nonuniformity. Unfortunately, it has been our experience that the default color schemes on commercial software tend to be too perceptually nonuniform to be of much use.

4.5 Automatic Detection and Quantification of Calcium Transients

The result of the computations in section 4.4.3 is a trace of ratio vs. time in a region of interest. Visual inspection can be used to identify ratio change events but this is time-consuming and prone to artifacts caused by human bias. This section describes algorithms for automatically detecting and parameterizing ratio change events, and for automatically compensating for photobleaching.

4.5.1 Automatic photobleaching estimation

As described in section 4.2.2, fluorophores that are excited for an extended period of time can undergo photobleaching. In a sample undergoing no FRET efficiency changes, photobleaching follows approximately an exponential decay. This suggests using an exponential fit to estimate photobleaching in samples where there is activity. However, we only want to fit the baseline ratio where there is no activity.

In order to accomplish this selective fitting, one can impose an asymmetric cost function to the fit. Typically one would attempting to minimize RMS distance between

the measured data points and the estimate from the fit, e.g.

$$E(A,B,k) = \sum \left(A + Be^{-kx_i} - y_i \right)^2$$

where y_i is the data point measured at x_i and A, B, k are the variable parameters of the fit. Instead, we might choose

$$E(A,B,k) = \sum \begin{cases} 100 \cdot \left(A + Be^{-kx_i} - y_i \right)^2 & \text{if} \quad y_i < A + Be^{-kx_i} \\ \left| A + Be^{-kx_i} - y_i \right| & \text{otherwise} \end{cases} \tag{4.27}$$

to penalize places where the fit is too high much more heavily than places where it is too low. This produces an exponential that is "shrink-wrapped" to the bottom of the trace, which is exactly what we want. Unfortunately, for a large data set, minimizing (4.27) can be computationally expensive.

A more computationally efficient alternative involves picking representative points (x_j, y_j) from the full data set $\{(x_i, y_i)\}$ and applying (4.27) to these representative points only. We use the following algorithm to select representative points, keeping in mind that we really want representative baseline points.

1. Subdivide the full data set into a number of equal pieces (e.g. 20, if there is not significant photobleaching in the first 1/20th of the trace).

2. For each piece, pick the data point with the lowest ratio.

3. Throw out any data points later in the trace that are higher than data points earlier in the trace (these presumably are during activity).

This algorithm produces up to 20 baseline-candidate points which empirically produce good results when a cost function such as (4.27) is used. (In general, the number 100 can be lowered here, as we have already preselected points near the baseline and thus do not need to so heavily discount places where the fit is far below the data; we have found that 5 gives decent results.)

Although this automated method usually produces good results, it cannot be used blind, as it is possible to distort the exponential fit in cases where activity levels build

from the beginning of the trace to the end, or vice versa. It is also not suitable for cases where photobleaching is very small and no correction is necessary. However, in cases where compensation is desirable and activity is sparse or evenly distributed over the recording, the algorithm can provide the values needed to perform the correction in (4.12). Of course, over multiple recordings from the same sample, the bleaching from trace to trace needs to also be kept track of, for instance by comparing the ratios of later traces to the initial ratio of the first trace.

4.5.2 Event detection

Single data sets can contain dozens of separate calcium transients. Depending on the experimental conditions, these can be either spontaneous or evoked by a stimulus. To reduce the labor required to parameterize the events, it is highly desirable to have automated methods for detecting ratio change events, especially in the case of spontaneous activity. Our methods rely on identifying slopes in the ratio characteristic of calcium transients.

Event detection is somewhat complicated by the fact that traces are inherently noisy. As discussed in section 4.4.3, we expect at best 2^6 bits of noise for 2^{12} bits of signal per pixel; from (4.18) we thus expect to have a signal-to-noise ratio of 2^5 per pixel for a zero-to-infinity ratio change. We would like to be able to observe ratio changes of under one percent, or 2^5 bits per pixel, yielding an optimal signal-to-noise ratio of 2^{-1}. Our regions of interest typically consist of dozens of pixels, but even so, for a single measurement the noise is comparable to the smallest signals we wish to detect.

Typical methods for dealing with noise involve low-pass filtering to reveal signals that change on a timescale slower than the frame rate of image capture. We use convolution with a Gaussian blur of the form $e^{-(x/\sigma)^2}$ as our low-pass filter. While any low-pass filtering technique should be suitable, we chose a blur since it is easy to implement, is free of ringing (which can complicate slope-detection), and is guaranteed to be local in effect (i.e. has a finite impulse response), allowing large data sets to be

blurred piecewise. The Fourier Convolution Theorem states that $F[f \star g] = F[f] \cdot G[g]$ where $F[\cdot]$ is the Fourier transform and f and g are (nearly) arbitrary functions. We thus compute our blur as follows. If $y(t)$ represents our data and b_σ the blur of width σ, the blurred data $y_b(t)$ is given by

$$y_b = F^{-1}[F[y] \cdot F[b_\sigma]]$$

To implement this formula on the computer, we use fast Fourier transforms (FFTs) on our discrete data. Note that FFT algorithms assume a constant sampling rate for y, which is approximately the case for our image data; on other types of data, one could use linear interpolation to produce a data set with a constant sample rate.

Calcium transients are distinguishable from noise to the human eye because they have an upward trend over several successive frames. We therefore use as a criterion for transients that at least N of M successive frames display an increase corresponding to a slope of at least s. By adjusting the parameters N, M, and s, as well as σ, it is possible to get highly reliable detection of calcium transients, comparable to what one can achieve by eye. This method typically detects only the steepest part of a transient reliably; to extend to the full transient, one can use a similar but more relaxed criterion to extend the limits of the detected transient. It is also possible to delimit plateaus by searching for a fall in ratio meeting the same type of criterion following a detected rise; the plateau then occupies the space between the rise and the fall.

4.5.3 Event parameterization

Once a ratio change event corresponding to a calcium transient has been identified, we would like to parameterize it. Ratio change events typically consist of a rapid rise followed by a slow return to baseline; sometimes there is a plateau phase between the rise and fall. The three primary parameters we use to describe an event are the duration, total increase in ratio, and rate of increase in ratio (hereafter, duration, rise, and slope); in cases where there is a plateau, the duration and height of the plateau is also of interest.

The blur used to aid detection, as described in section 4.5.2, will tend to lead to an overestimate of the true duration of an event. We therefore do additional processing to accurately compute the duration of the event and find more accurate bounds for later processing. We then compute the duration as the number of frames between the maximum and minimum values observed during the detected event, with the maximum and minimum computed using data convolved with a narrow blur and with values inside noise limits considered identical. Specifically, if the noise in the ratio is $\overline{n}_R$, the start of the true event is considered to be the last data point R_i such that $R_i - \min(R_k) < \overline{n}_R$ where k ranges over the detected region. The end of the true event is considered to be the first R_j such that $\max(R_k) - R_j < \overline{n}_R$. Duration is then $j - i$ times the frame rate. This shorter interval can then be used to compute the rise and the slope, as described below.

Computing the rise and the slope is confounded by several factors: blurring and noise both effect estimates of the rise, and the rising phase is rarely perfectly linear, making an estimation of slope somewhat ambiguous in addition to the effects of blurring and noise. Sharp transitions at the beginning and end of ratio change events will tend to be smoothed by blurring, reducing the apparent magnitude of the event as viewed on the blurred trace. The exact amount depends on the size of the blur and the sharpness of the transition. As such, to compute the total ratio change over the rising phase, we use the measurement blur described above rather than the stronger blur used in section 4.5.2. The rise is then simply the maximum ratio found in the rising phase minus the minimum ratio found there. However, during plateaus of essentially constant ratio, we expect noise to randomly generate measurements above the true ratio. The amount can be estimated with the cumulative distribution function of the Gaussian distribution; for our purposes it suffices to note that taking the maximum value will almost always be an overestimate. To compensate, we measure the peak of a plateau using the detection-blurred version of the data. While this does not eliminate the upward bias, it can substantially reduce it.

Slopes will also tend to be underestimated in the blurred data, so we use the raw

data to estimate the slope. We use a least squares estimate to fit a straight line to the points considered to be in part of the rising phase; this does not always yield a slope equal to the rise divided by the duration, since the latter is more heavily affected by a few points at either end of the rising phase. If the error in the fit is caused only by noise in the data, but the trace is otherwise linear, we expect that $\sum (y_i - \widehat{y}_i)^2 \approx (k-2)\,\overline{n}_R^2$ where y_i is the data, $\widehat{y}_i$ is the estimate of the data given by the linear fit, and k is the number of points used [Zar 1999, p. 335]. (This is just degrees of freedom multiplied by the tracewide noise.) As such,

$$\frac{\sum (y_i - \widehat{y}_i)^2}{(k-2)\,\overline{n}_R^2}$$

is an estimate of the linearity of the rising phase; values near 1 indicate a linear rising phase, while values substantially above 1 suggest that a linear fit may not be adequate for describing the data. Currently, our parameterization routines report this value as an advisory only; it is not used to try to improve the fit.

4.6 Discussion

4.6.1 Application of correction factors to ratiometric calcium recordings

We have predicted that a variety of factors that will alter the relationship between calcium concentration, which we wish to measure, and donor and acceptor fluorescent intensities, which is what we actually measure. Given the difficulty of correcting for even a majority of these factors, it is tempting to simply accept the errors and design experiments where both controls and experiments are subject to the same errors. As such, it is useful to know what must be kept constant in the experimental setup when a given correction is not applied.

Photobleaching correction, unsurprisingly, allows signals after photobleaching to be compared to those before, allowing for longer recordings with comparable values. In the absence of this correction, recordings must either be kept short enough so that photobleaching is minimal, or must be designed to have the same amount of photo-

bleaching under different conditions. In a system with a good signal-to-noise ratio, the former is often not unduly restrictive.

Different cameras, filter sets, microscopes, and so on, are liable to have different values of ζ and crosstalk terms. If $\Delta R/R$ is used as the ratio measurement, ζ does not come into play, but it is unsafe to assume that ratio change values are portable unless crosstalk correction is applied or the optical components have similar properties.

Measurement of the concentration of the indicator, coupled with determination of minimum and maximum ratios, in principle allows determination of the actual calcium flux (and with a bit more work, the free calcium concentration). However, these are particularly difficult measurements to make, so we are often limited to comparisons between conditions where we expect the dynamic range and concentration to be the same on average–for instance, limiting comparisons to different conditions applied to the same cell in the same animal. Despite the difficulty in measuring concentrations, it is our experience that especially dim cells tend to show larger and steeper ratio changes than bright cells to the same stimulation protocol, consistent with the inverse relationship between ratio change and indicator concentration in (4.24), and underscoring the need to be aware of unexpected differences in indicator concentration between experimental groups.

Encouragingly, once crosstalk and photobleaching corrections have been implemented in one's analysis tools, applying them becomes automatic. Thus, after the implementation barrier has been overcome, our results can be used to help produce data that enables more accurate comparisons between different researchers.

4.6.2 Ratiometric image data analysis

We have outlined a set of algorithms that produce event parameters given a series of donor/acceptor ratio image pairs. These algorithms can be implemented to require very little input from the user, which removes data analysis as a time-consuming post-experimental chore. Of particular note are the sub-pixel alignment and automatic tracking and measurement of regions of interest. Without these features, we found

analysis of in vivo ratiometric recordings of *C. elegans* tissues to be error-prone and slow to the point where it was a significant impediment to experimental progress. Theoretically, there is no reason why the analysis could not be performed live as the images were being acquired; on modern computers, all analysis steps run in a small fraction of the time taken by the image acquisition. Although the technical challenge of creating such a system prevented us from implementing one, such a tool would be highly valuable. In particular, a real-time analysis system could allow the experimental conditions to be triggered based on observed responses, such as delivering a sensory stimulus thought to provide inhibitory input to an interneuron while the interneuron was spontaneously active.

Chapter 5

Conclusion

It is the author's hope that the work herein will help to provide a basis for the functional characterization of the entire *C. elegans* nervous system. As a preliminary step towards this goal, we have developed computational techniques and recording and stimulation protocols that allow the quantitative monitoring of activity in two muscle systems, the pharyngeal muscles and the vulval muscles, and in two neuronal systems, the touch neurons and ASH. The success of calcium imaging in these systems suggests that the approach may be broadly applicable within the nervous system; even if this is not the case, the current system enables a more precise characterization of the molecular players in two distinct sensory systems. Further, many of the analytical techniques we use here are applicable to any fluorescent indicator in any suitable organism.

Several major challenges remain. Cameleon imaging has not yet been demonstrated in non-sensory cells, and there is no guarantee that calcium transients will be of the same magnitude in all neurons. Signals may be difficult to distinguish when their timing is not determined by a known stimulus. Also, while calcium imaging may be of general use in investigating excitatory input, the activity of inhibitory synapses is unlikely to be directly visible. Finally, the observation of activity is not necessarily sufficient for the construction of a model of the nervous system based on the electrical properties of the constituent cells. Nonetheless, in conjunction with electrical recordings, single-cell laser ablation, and other optical indicators, we hope that cameleon imaging will advance our understanding of behavioral circuits within the worm.

Bibliography

[Avery 1993] Avery, L. (1993). The genetics of feeding in *Caenorhabditis elegans*. Genetics *133*, 897-917.

[Avery and Horvitz 1989] Avery, L., and Horvitz, H.R. (1989). Pharyngeal pumping continues after laser killing of the pharyngeal nervous system of *C. elegans*. Neuron *3*, 473-485.

[Avery and Horvitz 1990] Avery, L., and Horvitz, H.R. (1990). Effects of starvation and neuroactive drugs on feeding in Caenorhabditis elegans. J. Exp. Zool. *253*, 263-270.

[Avery et al. 1995] Avery, L., Raizen, D., and Lockery, S. (1995). Electrophysiological methods. In *Caenorhabditis elegans*: modern biological analysis of an organism (Methods in Cell Bio. vol. 48), H.F. Epstein and D.C. Shakes eds. (San Diego, C.A.: Academic Press).

[Avery and Thomas 1997] Avery, L., and Thomas, J.H. (1997). Feeding and defecation. In *C. elegans* II, D.L. Riddle, T. Blumenthal, B.J. Meyer, and J.R. Priess, eds. (Cold Spring Harbor, NY: Cold Spring Harbor Laboratory Press).

[Baird et al. 1999] Baird, G.S., Zacharaias, D.A., and Tsien, R.Y. (1999). Circular permutation and receptor insertion within green fluorescent proteins. PNAS *96*, 11241-11246.

[Bangalore et al. 1996] Bangalore, R., Mehrke, G., Gingrich, K., Hofmann, F., and Kass, R.S. (1996). Influence of L-type Ca channel α_2/δ-subunit on ionic and gating current in transiently transfected HEK 293 cells. Am. J. Physiol. 270, H1521-H1528.

[Bargmann 1998] Bargmann, C. (1998). Neurobiology of the *Caenorhabditis elegans* Genome. Science *282*, 2028-2033.

[Bargmann and Avery 1995] Bargmann, C.I., and Avery, L. (1995). Laser killing of cells in *Caenorhabditis elegans*. In *Caenorhabditis elegans*: modern biological analysis of an organism (Methods

in Cell Bio. vol. 48), H.F. Epstein and D.C. Shakes eds. (San Diego, C.A.: Academic Press).

[Bargmann and Mori 1997] Bargmann, C., and Mori, I. (1997). Chemotaxis and Thermotaxis. In *C. elegans* II, D.L. Riddle, T. Blumenthal, B.J. Meyer, and J.R. Priess, eds. (Cold Spring Harbor, NY: Cold Spring Harbor Laboratory Press).

[Bargmann et al. 1990] Bargmann, C.I., Thomas, J.H., Horvitz H.R. (1990). Chemosensory cell function in the behavior and development of *Caenorhabditis elegans*. Cold Spring Harb. Symp Quant. Biol. *55*, 529-538.

[Brenner 1974] Brenner, S. (1974). The genetics of *Caenorhabditis elegans*. Genetics *77*, 71-94.

[Brenner 1988] Brenner, S. (1988). Foreward. In The Nematode *Caenorhabditis elegans*, W.B. Wood ed. (Cold Spring Harbor, New York: Cold Spring Harbor Laboratory Press.)

[Chalfie and Au 1989] Chalfie, M., and Au, M. (1989). Genetic Control of Differentiation of the Caenorhabditis-Elegans Touch Receptor Neurons. Science *243*, 1027-1033.

[Chalfie and Sulston 1981] Chalfie, M., and Sulston, J. (1981). Developmental genetics of the mechanosensory neurons of Caenorhabditis elegans. Dev. Biol. *82*, 358-370.

[Chalfie and White 1988] Chalfie, M., and White, J. (1988). The Nervous System. In The Nematode *Caenorhabditis elegans*, W.B. Wood ed. (Cold Spring Harbor, New York: Cold Spring Harbor Laboratory Press.)

[Christensen et al 2002] Christensen M, Estevez A, Yin X, Fox R, Morrison R, McDonnell M, Gleason C, Miller DM 3rd, and Strange K. A primary culture system for functional analysis of C. elegans neurons and muscle cells. Neuron *33*, 503-514.

[Christenson 2000] Christenson, M. (2000). The applications of scientific-grade CCD cameras to biological imaging. In Imaging Neurons, A Laboratory Manual, Yuste, R., Lanni, F., and Konnerth, A., eds. (Cold Spring Harbor, NY: Cold Spring Harbor Laboratory Press).

[CIE 1986] CIE (1986). Colorimetry, 2nd ed.; Publication CIE 15-2. (Vienna: Central Bureau of the Commission Internationale de LE'clairage)

[Dal Santo et al. 1999] Dal Santo, P., Logan, M.A., Chisholm, A.D., and Jorgensen, E.M. (1999). The inositol trisphosphate receptor regulates a 50-second behavioral rhythm in *C. elegans*. Cell *98*, 757-767.

[Davis and Stretton 1989] Davis, R.E., and Stretton, A.O. (1989). Passive membrane properties of motorneurons and their role in long-distance signalling in the nematode *Ascaris*. J. Neurosci. *9*, 403-414.

[De Waard and Campbell 1995] De Waard, M., and Campbell, K.P. (1995). Subunit regulation of the neuronal α_{1A} Ca^{2+} channel expressed in *Xenopus* oocytes. J. Physiol. *485*, 619-634.

[Driscoll and Chalfie 1991] Driscoll, M., and Chalfie, M. (1991). The *mec-4* gene is a member of a family of *Caenorhabditis elegans* genes that can mutate to induce neuronal degeneration. Nature *349*, 588-593.

[Driscoll and Kaplan 1997] Driscoll, M., and Kaplan, J. (1997). Mechanotransduction. In *C. elegans* II, D.L. Riddle, T. Blumenthal, B.J. Meyer, and J.R. Priess, eds. (Cold Spring Harbor, NY: Cold Spring Harbor Laboratory Press).

[Fan et al. 1999] Fan, G.Y., Fujisaki, H., Miyawaki, A., Tsay, R.-K., Tsien, R.Y., and Ellisman, M.H. (1999). Video-rate scanning two-photon excitation fluorescence microscopy and ratio imaging with cameleons. Biophys. J. *76*, 2412-2420.

[Forster 1948] Förster, T. 1948. Intermolecular energy migration and fluorescence. Ann. Phys. (Leipzig). *2*, 55-75.

[Goodman et al. 1998] Goodman, M.B., Hall, D.H., Avery, L., and Lockery, S.R. (1998). Active currents regulate sensitivity and dynamic range in *C. elegans* neurons. Neuron *20*, 763-772.

[Gordon et al. 1998] Gordon, G.W., Berry, G., Liang, X.H., Levine, B., and Herman, B. (1998). Quantitative fluorescence resonance energy transfer measurements using fluorescence microsocopy. Biophys. J. *74*, 2702-2713.

[Hart et al. 1999] Hart, A.C., Kass, J., Shapiro, J.E., and Kaplan, J.M. (1999). Distinct signaling pathways mediate touch and osmosensory responses in a polymodal sensory neuron. J. Neurosci. *19*, 1952-1958.

[Hart et al. 1995] Hart, A.C., Sims, S., and Kaplan, J.M. (1995). Synaptic code for sensory modalities revealed by *C. elegans* GLR-1 glutamate receptor. Nature *378*, 82-85.

[Hilliard et al. 2002a] Hilliard, M.A., Bargmann, C.I., and Bazzicalupo, P. (2002). *C. elegans* responds to chemical repellents by integrated sensory inputs from the head and the tail. Current Biology *12*, 730-734.

[Hilliard et al. 2002b] Hilliard, M.A., Plasterk, R.H.A., and Bazzicalupo, P. (2002). Worms taste bitter: ASH sensory neurons and *qui-1* mediate quinine avoidance in *C. elegans*. Submitted, EMBO. J..

[Jorgensen and Rankin 1997] Jorgensen, E.M., and Rankin, C. (1997). Neural Plasticity. In *C. elegans* II, D.L. Riddle, T. Blumenthal, B.J. Meyer, and J.R. Priess, eds. (Cold Spring Harbor, NY: Cold Spring Harbor Laboratory Press).

[Kaplan and Horvitz 1993] Kaplan, J.M., and Horvitz, H.R. (1993). A dual mechanosensory and chemosensory neuron in *Caenorhabditis elegans*. PNAS *90*, 2227-2231.

[Kerr et al. 2000] Kerr, R., Lev-Ram, V., Baird, G., Vincent, P., Tsien, R.Y., and Schafer, W.R. (2000). Optical imaging of calcium transients in neurons and pharyngeal muscle of *C. elegans*. Neuron *26*, 583-594.

[Koltzenberg et al. 1997] Koltzenberg, M., Stucky, C.L., and Lewin, G.R. (1997). Receptive properties of mouse sensory neurons innervating hairy skin. J. Neurophysiol. *78*, 1841-50.

[Lakowicz 1983] Lakowicz, J.R. (1983). Energy transfer. In Principles of Fluorescence Spectroscopy (New York, New York: Plenum Press).

[Lee et al. 1997] Lee, R.Y.N., Lobel, L., Hengartner, M., Horvitz, H.R., and Avery, L. (1997). Mutations in the $\alpha 1$ subunit of an L-type voltage-activated Ca^{2+} channel cause myotonia in *Caenorhabditis elegans*. EMBO *16*, 6066-6076.

[Lobel and Horvitz 1997] Lobel, L, and Horvitz, H.R. unpublished; reported (1997) in *C. elegans* II, D.L. Riddle, T. Blumenthal, B.J. Meyer, and J.R. Priess, eds. (Cold Spring Harbor, NY: Cold Spring Harbor Laboratory Press), p. 1033.

[Maduro and Pilgrim 1995] Maduro, M., and Pilgrim, D., (1995). Identification and cloning of *unc-119*, a gene expressed in the *Caenorhabditis elegans* nervous system. Genetics *141*, 977-988.

[Maricq et al. 1995] Maricq, A.V., Pekcol, E., Driscoll, M., and Bargmann, C.I. (1995). Mechanosensory signaling in *C. elegans* mediated by the GLR-1 glutamate receptor. Nature *378*, 78-81.

[Mello and Fire 1995] Mello, C. and Fire, A., (1995). DNA transformation. In *Caenorhabditis elegans*: modern biological analysis of an organism (Methods in Cell Bio. vol. 48), H.F. Epstein and D.C. Shakes eds. (San Diego, C.A.: Academic Press).

[Mendel et al. 1995] Mendel, J.E., Korswagen, H.C., Liu, K.S., Hajdu-Cronin, Y.M., Simon, M.I., Plasterk, R.H.A., and Sternberg, P.W. (1995). Science *267*, 1652-1655.

[Miyawaki et al. 1997] Miyawaki, A., Llopis, J., Heim, R., McCaffery, J.M., Adams, J.A., Ikura, M., and Tsien, R.Y. (1997). Fluorescent indicators for Ca^{2+} based on green fluorescent proteins and calmodulin. Nature *388*, 882-887.

[Miyawaki et al. 1999] Miyawaki A., Griesbeck, O., Heim, R., and Tsien, R.Y. (1999). Dynamic and quantitative Ca^{2+} measurements using improved cameleons. PNAS *96*, 2135-2140.

[Munger and Ide 1988] Munger, B.L., and Ide, C. (1988). The Structure and Function of Cutaneous Sensory Receptors. Arch. Histol. Cytol., *51*, 1-34.

[Munsell 1915 etc.] Munsell, A.H., the Munsell Color Corporation, and GretagMacbeth (1915 and on). Munsell Book of Color (New Windsor, NY: GretagMacbeth LLC).

[Nagai et al. 2002] Nagai, T., Ibata, K., Park, E.S., Kubota, M., Mikoshiba, K., and Miyawaki, A. (2002). A variant of yellow fluorescent protein with fast and efficient maturation for cell-biological applications. Nature Biotech. *20*, 87-90.

[Nagai et al. 2001] Nagai, T., Sawano, A., Park, E.S., Miyawaki, A. (2001). Circularly permuted green fluorescent proteins engineered to sense Ca2+. PNAS *98*, 3197-3202.

[Neher 1995] Neher, E. (1995). The use of fura-2 for estimating Ca buffers and Ca fluxes. Neuropharm. *34*, 1423-1442.

[Okkema et al. 1993] Okkema, P.G., Harrison, S.W., Plunger, V., Aryana, A., and Fire, A. (1993). Sequence requirements for myosin gene expression and regulation in *Caenorhabditis elegans*. Genetics *135*, 385-404.

[Persechini et al. 1997] Persechini, A., Lynch, J.A., and Romoser, V.A. (1997). Novel fluorescent indicator proteins for monitoring free intracellular Ca-2+. Cell Calcium *20*, 209-216.

[Press and Teukolsky 1995] Press, W.H., Teukolsky, S.A., Vettering, W.T., Flannery, B.P. (1995). Numerical Recipes in C, 2nd edition (New York, NY: Cambridge University Press).

[Price et al. 2000] Price, M.P., Lewin, G.B., McIlwrath, S.L., Cheng, C., Xie, J., Heppenstall, P.A., Stucky, C.L., Mannsfeldt, A.G., Brennan, T.J., Drummond, H.A., Qiao, J., Benson, C.J., Tarr, D.E., Hrstka, R.F., Yang, B., Williamson, R.A., and Welsh, M.J. (2000). The mammalian sodium channel BNC1 is required for normal touch sensation. Nature *407*, 1007-1011.

[Raizen et al. 1995] Raizen, D.M., Lee, R.Y.N., and Avery, L. (1995). Interacting genes required for pharyngeal excititation by motor neuron MC in *Caenorhabditis elegans*. Genetics *141*, 1365-1382.

[Rankin and Broster 1992] Rankin, C.H., and Broster, B.S. (1992). Factors affecting habituation and recovery from habituation in the nematode *Caenorhabditis elegans*. Behav. Neurosci. *106*, 239-249.

[Riddle et al. 1997] Riddle, D.L., Blumenthal, T., Meyer, B.J., and Price, J.R. (1997). Introduction to *C. elegans*. In *C. elegans* II, D.L. Riddle, T. Blumenthal, B.J. Meyer, and J.R. Priess, eds. (Cold Spring Harbor, NY: Cold Spring Harbor Laboratory Press).

[Romoser et al. 1997] Romoser, V.A., Hinkel, P.M., and Persechini, A. (1997). Detection in living cells of Ca-2+-dependent changes in the fluorescence emission of an indicator composed of two green fluorescent protein variants linked by a calmodulin-binding sequence: A new class of fluorescent indicators. JBC *272*, 13270-13274.

[Sakai et al. 2001] Sakai, R., Repunte-Canonigo, V., Raj, C.D., and Knopfel, T. (2001). Design and characterization of a DNA-encoded, voltage-sensitive fluorescent protein. Eur. J. Neurosci. *13*, 2314-2318.

[Sambongi et al. 1999] Sambongi Y., Nagae, T., Liu, Y., Yoshimizu, T., Takeda, K., Wada, Y., and Futai, M. (1999). Sensing of cadmium and coppyer ions by externally exposed ADL, ASE, and ASH neurons elicits avoidance response in *Caenorhabditis elegans*. Neuroreport *10*, 753-757.

[Sandison et al. 1995] Sandison, D.R., Williams, R.M., Wells, K.S., Strickler, J., and Webb, W.W. (1995). Quantitative Fluorescence Confocal Laser Scanning Microscopy (CLSM). In Handbook of Biological Confocal Microscopy (2nd ed.), J.B. Pawley ed. (New York, New York: Plenum Press.)

[Segalat et al. 1995] Segalat, L., Elkes, D.A., and Kaplan, J.M. (1995). Modulation of serotonin-controlled behaviors by G_o in *Caenorhabditis elegans*. Science *267*, 1648-1651.

[Siegel and Isacoff 1997] Siegel, M.S., and Isacoff, E.Y. (1997). A genetically encoded optical probe of membrane voltage. Neuron *19*, 735-741.

[Singer et al. 1991] Singer, D., Biel, M., Lotan, I., Flockerzi, V., Hofmann, F., and Dascal, N. (1991). The roles of the subunits in the function of the calcium channel. Science *253*, 1553-1557.

[Sun et al. 1999] Sun, B., Peizhang, X., and Salvaterra, P.M. (1999). Dynamic visualization of nervous system in live *Drosophila*. PNAS *96*, 10438-10443.

[Sequencing Consortium 1998] The *C. elegans* Sequencing Consortium (1998). Genome sequence of the nematode *C. elegans*: a platform for investigating biology. Science *282*, 2012-2018.

[Trent et al. 1983] Trent, C., Tsung, N., and Horvitz, H.R. (1983). Egg-laying defective mutants of the nematode *Caenorhabditis elegans*. Genetics 104, 619-647.

[Troemel et al. 1995] Troemel, E.R., Chou, J.H., Dwyer, N.D., Colbert, H.A. and Bargmann, C.I. (1995). Divergent seven transmembrane receptors are candidate chemosensory receptors in *C. elegans*. Cell *83*, 207-218.

[Tsien and Backsai 1995] Tsien, R.Y., and Backsai, B.J. (1995). Video rate confocal microscopy. In Handbook of Biological Confocal Microscopy (2nd ed.), J.B. Pawley ed. (New York, New York: Plenum Press.)

[Tsien and Harootunian 1990] Tsien, R.Y., and Harootunian, A.T. (1990). Practical design criteria for a dynamic ratio imaging system. Cell Calcium *11*, 93-109.

[Tsien and Waggoner 1995] Tsien, R.Y., and Waggoner, A. (1995). Fluorophores for Confocal Microscopy. In Handbook of Biological

Confocal Microscopy (2nd ed.), J.B. Pawley ed. (New York, New York: Plenum Press.)

[Waggoner et al. 1998] Waggoner, L.E., Zhou, G.T., Schafer, R.W., and Schafer, W.R. (1998). Control of alternative behavioral states by serotonin in *Caenorhabditis elegans*. Neuron *21*, 203-214.

[Walker et al. 2000] Walker, R.G., Willingham, A.T., and Zuker, C.S. (2000). A *Drosophila* mechanosensory transduction channel. Science *287*, 2229-2234.

[Way and Chalfie 1989] Way, J.C., and Chalfie, M. (1989). The *mec-3* gene of *Caenorhabditis elegans* requires its own product for maintined expression and is expressed in three neuronal cell types. Genes Dev. *3*, 1823-1833.

[Welsh and Xie 2001] Welsh, M.J., Price, M.P., and Xie, J. (2001). Biochemical basis of touch preception: mechanosensory function of Degenerin/epithelial Na^+ channels. J. Biol. Chem. *277*, 2369-2372.

[White 1988] White, J. (1988). The Anatomy. In The Nematode *Caenorhabditis elegans*, W.B. Wood ed. (Cold Spring Harbor, New York: Cold Spring Harbor Laboratory Press.)

[White et al. 1986] White, J.G., Southgate, E., Thomson, J.N., and Brenner, S. (1986). The structure of the nervous system of the nematode *Caenorhabditis elegans*. Philos. Trans. R. Soc. Lond. B Biol. Sci. *314*, 1-340.

[Wicks and Rankin 1997] Wicks, S.R., and Rankin, C.H. (1997). Effects of tap withdrawal response habituation on other withdraw behaviors: the localization of habituation in the nematode *Caenorhabditis elegans*. Behav. Neurosci. *111*, 342-353.

[Wood 1988] Wood, W.B. (1988). Introduction to *C. elegans* biology. In The Nematode *Caenorhabditis elegans*, W.B. Wood ed. (Cold Spring Harbor, New York: Cold Spring Harbor Laboratory Press.)

[Xia and Liu 2001] Xia, Z., Liu, Y. (2001). Reliable and Global Measurement of Fluorescence Resonance Energy Transfer Using Fluorescence Microscopes. Biophys. J. *81*, 2395-2402.

[Zar 1999] Zar, J.H. (1999). Biostatistical Analysis, 4th edition (Upper Saddle River, New Jersey: Prentice-Hall)

[Zhou et al. 1998] Zhou, G.T., Schafer, R.W., and Schafer, W.R. (1998). A three-state biological point process model and its parameter estimation. IEEE Trans. Signal Process. *46*, 2698-2707.